Nanomechanical Forming Studies of Thin Polymer Films

Barry O'Connell, B.Sc.

A thesis submitted for the degree of Doctor of Philosophy to The University of Dublin, Trinity College.

August 17, 2008

Declaration

I, Barry O'Connell, declare the following;

- that this thesis is my entirely own work unless cited and acknowledged within the text.
- that this thesis has not been submitted as an exercise for a degree at TCD or any other University.
- that the Library of TCD may lend or copy this thesis upon request.

Summary

Nanoimprint is a technique that involves mechanical patterning using a rigid patterned stamp on a deformable thin film to produce nanostructures. It is also a technique that is the focus of much research because of the benefits it brings over other nanofabrication methods. It is a planar process potentially capable of producing high resolution features at a high throughput and low cost since it's inception in 1995 reproducing features smaller than 25nm [1] and soon afterwards, features below 10nm in 1997 [2].

This project attempted to address some of the issues such as using the approach of instrumented indentation on single feature stamps. With this approach it was possible precisely isolate, control and measure the stresses and strains of the material during and after the imprint event [3] [4] [5].

Using the high sensitivity of the nanoindenter, measurements were carried out to determine the mechanical state of features created by wide area hot embossing of polystyrene [5]. It was found that no measurable difference could be determined between pristine untouched film and that which had undergone flow.

An investigation into the phenomenon of residual layers of unextruded material was carried out [6]. The thickness of the unextruded layer was found to be dependent only on the stamp geometry and independent of applied load, stamping time and initial film thickness. Continuing to increase the applied load was seen to have little effect on the film and served to only deform the stamp and substrate.

As applying enormous loads was shown to cause only non-uniformity in the residual material, an attempt to introduce plasticity by maximising shear and minimising hydrostatic pressure was attempted [7]. It was possible to develop a novel processing technique for thin solid polymer films. This technique [8], known as Small Amplitude Oscillation Shear Forming (SAOSF) activates material transport in an efficient manner by introducing a small oscillatory shear strain which drives plasticity under the stamp and also ratchets material out from under the stamp.

Abstract

The ability to add form and structure to matter for it to function with a given purpose is one taken for granted, but the ability to do so effectively on the nanoscale is still an ongoing concern. The goal of nanostructure fabrication is maximise function in a finite space and as such, it has received much attention and given rise to many techniques, the majority of which utilise a planar geometry for fabrication. Traditional techniques are becoming less feasible with each generation of technology, prompting the development of alternatives.

Mechanical patterning of thin films is one such alternative, identified as a potential for efficient nano-structure fabrication, regarding technologies such as integrated circuits, microelectromechanical systems (MEMS) and photonic devices. Presented here, is an investigation into aspects of forming in planar geometries, specifically, thin glassy polymer films on the sub-micron and nanoscale. The limits to imprint are examined with respect to stamp geometry and materials and the effect on residual height.

A novel technique is presented and discussed which allows forming in a wide range of materials without initiating extraordinary conditions. This is accomplished by direct introduction of deviatoric stresses whilst minimising parasitic hydrostatic stresses. This new technique is known as Small Amplitude Oscillatory Shear Forming (SAOSF).

Acknowledgements

Thanks to both Prof. John Pethica and Dr. Graham Cross for sage guidance, supervision and squeezing every last drop of effort out of me.

Thanks to The Comrades, Simon, Andy, Alan and Siobhan.

Michael Riley, machinist extraordinaire. Harry. Jacqui & Tracy. The characters through the years, for many reasons, Suzi, Catherine, Higgsey, Rowan, Gillian, Niamh, Jason, Camilla, Anika and Davey. Thanks, to neglected friends.

Extra Special Thanks to Paula for help, patience and motivation over the years, (now *I* get to play computer games again).

And to Gerry & Seamus, for financial and moral support and the sacrifices made so I could go this far.

Created in LaTeXusing TeXShop and BibDesk on various Macs with the assistance of Inkscape and Open Office, so thanks are also due to the myriad efforts that resulted in various chunks of Open Source Software

Contents

List of Figures

List of Tables

List of Symbols

a	Radius of Indenter Contact, Radius of Hydrostatic Core
A	Area
A_P	Harmonic Contact Area
A_T	Reduced Variable Shift Factor
A'	Pre-exponential Factor
$\vec{B}$	Magnetic Field Strength
c	Radius of Plastic Zone
c_0	Concentration of Solution
C	Constraint Factor
C'	EmpiricalConstant for WLF Equation
C_n	Conatact Area Coefficient for Indenter Tip
d	Distance
D	Indenter Shaft Damping
E	Young's Modulus
E_{eff}	Effective Modulus
E_a	Activation energy
E_r	Reduced Modulus
F	Force
G	Shear Modulus, Gibbs Energy
h	Planck Constant, Displacement of Indenter Tip Into Surface, Height
h_0	Amplitude of Harmonic Displacement
h_c	Indentation Depth
h_e	Elastic Recovery of indent
h_p	Depth of Plastic Penetration
h_r	Post-indent Plastic Depth
H	Hardness, Enthalpy
HCS	Harmonic Contact Stiffness
HF	Harmonic Frame Stiffness
HFC	Harmonic Frame Correction
k_B	Boltzman Constant
K_f	Indenter Frame Stiffness
K_p	Indenter Shaft Stiffness
K	Bulk Modulus
l	Length

m	Mass
M	Molecular Mass
M_W	Molecular Weight
n	Number of Species
p	Hydrostatic Pressure
p_m	Mean Contact Pressure
P	Load on Sample, Compressive Stress
r	Indenter Radius
R	Gas Constant
S	Stiffness
S_h	Harmonic Stiffness
t	Film Thickness
T	Temperature
T_g	Glass Transition Temperature
U	Bond Potential Energy
v	Activation Volume
Y	Yield Stress
α	Coefficient of Internal Friction
α_G	Volumetric Coefficient of Expansion in Glass Phase
α_R	Volumetric Coefficient of Expansion in Rubber Phase
β	Tip Geometry Factor, Volume Factor
ϵ	Strain
ϵ_n	Nominal Stress
ϵ_t	Transverse Stress
η	Viscosity
κ	Free volume
μ	Coefficient of Friction
ν	Poisson Ratio, Rate of Molecular Movements
ω	Probability of Energy Barrier Transition, Frequency
ϕ	Phase
σ	Stress
σ_0	Uniaxial Yield Stress
σ_r	Radial Stress
σ_n	Nominal Stress
σ_Z	Normal Stress
τ	Shear Stress

Chapter 1

Introduction

1.1 Introduction

This project is about deforming material, using the time honoured method of applying force [9, 10, 11]. By ensuring sufficient shearing forces are present to initiate permanent deformation, an amorphous shape can be formed into a more ordered state, fulfilling a defined function. How the material behaves when subjected to forces depends on the material itself and it's shape. The humble nail[1] serves as an illustration.

It would be unacceptable for a nail to undergo large scale plastic deformation when being hammered into a wall, so the nail must be made of a material that can withstand the forces placed on it, such as steel. However, the nail must first be made into a useful shape or geometry to perform it's job correctly. Fortunately, even for such a material as steel, choices exist on how such deformations can occur. Using a large hammer made of harder material than the nail, enormous forces can be placed on a piece of steel to form it into the desired shape. Another option is to provide energy in another form, such as heat, in order to soften the steel and lower the required forces, hence lowering the requirements on the tools needed to make the nail. By melting the steel and pouring it into molds, gravity is often sufficient to provide the required

[1]Nail: An age old, ubiquitous fastener of great architectural and religious significance.

forces.

Economics is also a factor, usually resulting in a compromise between physical ease and cost. Taking the example above, producing molten steel is a difficult and costly process unsuitable for the required quantities and associated price plasticity of demand. Up until the 18^{th} century, hot forming was a common process of nail manufacture, often performed by a blacksmith. This method was costly of both time and energy involving careful heating, then forming, then careful cooling. This method was superceded by a cold forming method, the wire method.

The wire method provides the preform of the nail as a coil of wire, the wire is unraveled and cut to the desired length. Each of the lengths is then formed with suitable tools. The success of the wire method relies on the choice of materials and therefore a knowledge of how these materials behave. This process, lacking in complications, is easily automated and enormous quantities may be manufactured due to ease of handling raw materials and the simplicities inherent with working at room temperature.

Many analogies may be drawn between this lengthy description of nail manufacture and the goals of NanoImprint Lithography. However, a significant differences exist, primarily the ever decreasing feature sizes required in modern manufacturing fields and the associated problems and challenges [12].

1.1.1 Imprint vs. Traditional Lithography Methods

The most prominent problem facing semiconductor fabrication is that of capital expenditure on fabrication facilities. Facilities required (known as "Fabs") cost billions to setup and run. Emerging trends such as "fabless" semiconductor companies are becoming common place as are the shared facilities known as "foundries" where several companies share the cost of building and running a fab. Taking just one example, modern photomasks are incredibly complex, with transistor counts in the millions and up to 10 layers of interconnects [13], the technical difficulties are significant (and

therefore expensive) in creating and checking each of the masks required.

A driving force in many fields today is to increase device functionality in ever smaller volumes. This is most evident in the semiconductor industry, but it also applies in many other fields. Bottom up manufacture has great scope for large volume manufacture, however, certain disadvantages are present that don't exist with top down methods, such as homogeneity of the product. Other top down methods such as optical lithography are becoming prohibitively expensive. Other techniques such as e-beam lithography achieve low throughput and are therefore too costly for mass production.

Nanoscale forming is a viable top down production method, where accuracy and reproducibility counts and contains the potential to produce volumes on par with modern semiconductor methods. It has been proven to be capable of exceedingly high-resolution work and repeatability [14]. Currently nanoscale forming is a field with many unanswered questions and unresolved problems. For example, the surface area to volume ratio is considerable on the sub-micron scale where surface forces begin to dominate on these scales.

1.1.2 Nanofabrication: A question of scale

Nanofabrication describes a range of fabrication techniques that have arisen out of the demand for ever increasing functionality in ever decreasing form factors. The drive to maximise functionality in a minimal space is exemplified by the semiconductor industry. For years, it has been following a track of improving the functionality and speed of products in a highly competitive market. Crudely put, what this means is attempting to get as many transistors into a single device as possible. Design considerations such as signal propagation times, evolved heat, added complexity, and speed of state transitions means that transistors and their electrical interconnects have been steadily shrinking in size over the years.

To take two extreme points, consider the first commercially available monolithic mi-

croprocessor, the Intel 4004. This was released for sale in 1971 and was manufactured using a 10μm process [2], utilising 2250 transistors and clocked to 740kHz [15]. Compare this to the IBM POWER6, released in 2007, containing 790 million transistors manufactured using a 65nm process and capable of being clocked beyond 4.7GHz [13]. This is an improvement of several orders of magnitude in all areas in under 40 years.

Pundits are often heard telling of a time when traditional optical lithography methods will cease being effective or economically viable, with governments and the semiconductor industry following similar line of thought [16]. For this reason, alternatives to optical methods are being sought. NIL is one of these alternatives. Imprint Lithography involves the transfer of a topographic pattern from a hard master stamp into a softer substrate. NIL has been gathering momentum since it's inception in the form of hot forging in 1995 by Chou et al. These authors demonstrate an array of 25nm diameter dots with a 120nm pitch in PMMA (Polymetylmethacralate) on silicon [1]. NIL was proposed as a viable alternative to the more traditional optical lithography techniques [17] and was followed by examples exhibiting 10nm features [2]. The viability of this technique has been validated, with effective wafer wide imprints being realised on up to 100mm wafers [18] [19]. As such, in the ITRS (International Technology Roadmap for Semiconductors) semiconductor development roadmap [20], NIL is scheduled to enter the preproduction phase as a viable lithography process by 2012.

Nanoscale engineering

Nanoscale engineering reveals some novel properties of materials that are not normally observed on the microscale and above. As feature sizes decrease, the physical properties of the material can differ from those observed in bulk. These properties make new devices and processes possible, such as, photonic crystals, catalysts with increased surface area, nanoporous membranes, direct patterning of active materials and more [21]. Generally, these nanoscale properties are associated with features on the sub−50nm scale, although the exact length scale depends on the process itself

[2]This means that the smallest feature size of the on-chip components is about 10μm, transistors and other structures are naturally larger, being comprised of multiple components.

and the morphology of the material. Nanocrystals, nanowires, sols and colloids are some of the forms which can be fabricated through various methods. Modification of these forms can lead to variations in melting point, phonon behaviour, electronic band structure and optical emission and absorption [22]. Even though nanostructured materials can be engineered to produce desired effects, exploiting these properties in a useful manner raises some questions about how to create an integrated system that provides a level of practicality to the end user. Self-assembly could be seen as an extension of nanofabrication of materials, aiming to provide a level of order of the individual components. Many potentially useful mechanisms for self assembly have been investigated [23, 24], but the commercialisation of these processes is still an ongoing challenge. It should be noted that certain forms of self assembly have been well known for many years, from highly single molecular clusters [25] to liquid crystals and extending to biological processes.

The question arises of how such materials are manufactured and assembled, playoffs exist between feature sizes and throughput. Chemical synthesis has been shown to be highly effective at creating a zoo of materials, which is easily performed in 3D in solutions, but as argued by Cross [12], chemical methods cannot yet produce objects of sufficient uniformity, composition and stiffness in the $10 - 100$nm range. Well documented methods of fabrication exist which allow arbitrary features to be constructed, such as beam lithography, (used in the formation of electrodes separated less than 10nm [26]), scanning probe manipulation of single molecules, (to form molecular logic gates [27]).

Even nanoimprint lithography, which can reproduce physical features below 2nm [28] and which can lend itself to high throughput replication may have difficulty competing with the throughput of some chemical processes. However, high resolution coupled with the possibility of using wide area stamps leading to relatively high throughput makes nanoimprint a conceivable candidate for bridging the gap between top-down[3] and bottom-up technologies. For example, functional nanomaterials could be

[3]Top-down fabrication refers to the fabrication of micro or nano components using macro sized tools. Bottom-up refers to components being constructed using building blocks smaller than the final product.

corralled in place in areas modified by imprint methods which can cause variations in topology or surface chemistry [21].

1.1.3 Synopsis of Thesis

Chapter 1

Introduction

Where the project is introduced and the motivations behind forming on the nanoscale are discussed.

Chapter 2

Background

Here, a review of Nanoimprint Lithography (NIL) relevant to this project is undertaken, along with an introduction to some of the concepts involved in mechanical forming. Mechanisms behind elasticity and plasticity of materials are considered and also the theory behind determining physical properties of materials using nanoindentation.

Chapter 3

Instrumentation

This chapter highlights the instrumentation of the project. The specific details of the nanoindenter used in this project, as well as describing modifications made to the nanoindenter setup can be found in this chapter. Descriptions of microscopy methods such as Atomic Force Microscopy (AFM) and Scanning Electron Microscopy (SEM) which were used to characterise features beyond the limit of optics.

The materials used in the project are considered here, stamps, substrates and their preparation for measurement. The design of the oven is examined and then as well as the shear setup.

Chapter 4

Experimental Techniques & Investigations

The methods of constructing the stamps with which the deformations were carried out are described as well as preparation and characterisation of polymer films. Details of the experimental methods and behaviour of the instrumentation are found here.

Chapter 5

Normal Force Forming

An examination into driving plasticity through compression with variations in temperature geometry and force. An investigation into the existence of residual strains in a sample of hot embossed polymer is carried out. Normal force loading is shown to have limited success when driving plastic flow.

Chapter 6

Shear Injection Forming

The experiments carried out in Chapter 5 led to attempts to inject shear directly into the system as a more efficient method of driving plasticity. Chapter 6 demonstrates the the implementation of Small Amplitude Oscillatory Shear Forming (SAOSF). The effectiveness of this method and attempts to characterise the process are made. It is shown that SAOSF is a scale independent, isothermal process that preserves high fidelity features on the nanoscale.

Chapter 7

Conclusion

A summary of the project and a discussion on future work.

Chapter 2

Background

2.1 Background

This project investigates the mixture of permanent (plastic) and temporary (elastic) strains that result in a material when a tool is used to stress that material. The goal was to establish an understanding of the processes involved to control aspects of these deformations and attempt to improve these processes.

Forming of materials is an ancient art and a detailed understanding of the processes has been built up over the years. The relationship of stress and strain in materials has been observed for many years (as described in many publications detailing the work of Hooke, Euler & Young). The advent of atomic theory established an understanding of the mechanisms for these behaviors, explaining why they differ between materials. In this thesis, contact mechanics and the relationship to theories of plasticity in polymers are examined. The main goal was to selectively activate plasticity in a polymer film through application of a physical force.

2.2 Literature Review

2.2.1 Production of Nanostructures by Mechanical Forming

Nanoimprint Lithography (NIL) is a method of mechanically patterning planar substrates to facilitate selective removal or deposition of material. This technique has been shown to be extremely effective when applied to resist patterning with the potential to succeed current optical lithographic processes in many areas. A simplified example of an imprint process is shown in figure 2.1. As outlined in the original NIL proposals and demonstrations [1, 17], a film of deformable material supported by a rigid substrate (A) has a rigid stamp pushed into it. The applied forces deform the material(B). The stamp is then removed, leaving the desired pattern imprinted in the deformable material(C). The reality is not as simple or perfect as this, phenomena such as pile-up, incomplete filling of cavities, deformation of stamp and substrate, residual material etc. complicate the process and are discussed in Chapters 5 and 6.

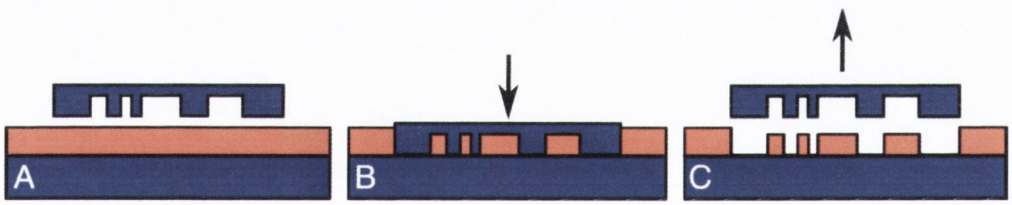

Figure 2.1: Basic Example of Imprint Forming. A film of deformable material supported by a rigid substrate (A) has a rigid stamp pushed into it. The applied forces deform the material(B). The stamp is then removed leaving the desired pattern imprinted in the deformable material(C).

2.2.2 Stamp Construction

As described above, NIL requires a patterned stamp or mold with which to deform material to the desired effect. A large number of materials are available for stamp construction as long as the material it is made from has a sufficient modulus and hardness to withstand the forces applied without undergoing undesired deformation. Materials

used range from rigid diamond [29] to highly flexible PDMS[1] [28] and are dictated by factors such as cost, ease of use, transparency (e.g for step & flash lithography [30]), hardness, thermal coefficient (for hot embossing [31]), etc.

Optical lithography methods can be used to create stamps where small feature sizes are not essential. Optical lithography is well characterised, scales to wide areas and large aspect ratio features can be created easily in a large selection of materials. A photomask is prepared and used to selectively mask off areas of a wafer coated with a polymer based photosensitive resist. The wafer and mask are exposed to light and the photomask exposes areas of the resist. Exposed areas of the resist breakdown or cross-link on exposure and can be removed from the wafer using a solvent. The remaining resist then protects parts of the wafer from an etching process where the desired patten is etched into the wafer. However, optical lithography requires that the photomasks are prepared using beam lithography, which is costly and time consuming [14].

Beam Lithography is another method which demonstrates greater resolution than optical lithography, but is actually used to prepare the photomasks for optical lithography. A beam of electrons or ions is directed onto a material which undergoes a change on interaction with the beam and removed. As mentioned above, beam lithography has a low throughput but can achieve a resolution of smaller than 20nm [24].

More inventive methods have to be considered when striving for extremely high resolutions. For example, the method described by Hua et al. above, successfully achieved molecular resolution. PDMS was poured onto a substrate covered with single wall carbon nanotubes of approximately 2nm diameter, the PDMS was cured and removed from the substrate. Replication of the nanotubes on the surface was demonstrated when the PDMS template was used to mold a layer of polyurethane precursor [28].

Although the stamps are effectively planar, 3-Dimensional features are possible, this "2.5D" approach is of importance as the complexity of modern semiconductor manufacture means that a many layer design is required for interconnects between transistors and the insulators between them. Such a process can involve almost two hundred

[1]Polydimethylsiloxane, a silicon based polymer that with a low molecular weight is a fluid, but is easily crosslinked to an elastic solid.

steps. It has been shown that careful design of an imprint lithography stamp can reduce the number of steps required, one example of which is the dual damascene process[2] process [32].

2.2.3 Variations on NIL techniques

Many variations on the basic NIL theme exist [14], where the desired results, such as the form, function and throughput dictate the design space, as discussed by Cross [12]. The design space considers the constitutive response of the material to be formed, the local and global geometry of the stamp, boundary conditions and the load history.

Variations on the NIL process include Hot Embossing [33], Microcontact Printing (μCP) [34], Laser Assisted Direct Imprint (LADI) [35] and Step and Flash Imprint Lithography (SFIL) [36]. Hot embossing lowers the viscosity of the film through heating, thus reducing the forces required for deformation. μCP prints a mask directly onto the substrate and although this is a print process rather than an imprint process, material transport is still involved. SFIL uses a LASER and etched quartz stamp, where the laser is used to crosslink a layer of liquid polymer precursor into which the quartz stamp is situated. A more direct version of this process uses a LASER to melt the silicon directly and a pattern etched on a quartz stamp molds the molten silicon.

Resists

Some NIL methods focus on modifying the resist properties to solve some of the problems and many different types of imprint resists have become commercially available thus signifying widespread use. By using a liquid resist with a low viscosity, large pressures do not have to be employed, thus avoiding unwanted elastic strains of the system and reducing cycle times. A number of methods avail of the ease of forming

[2]The Dual Damascene process whereby vias (a "via" is a provision for a interconnection between layers) and a wiring level are created simultaneously

of a low viscosity liquid followed by a phase change to preserve the features of the stamp. SFIL uses a resist that solidifies upon exposure to UV light, via the formation of crosslinks within the polymer matrix [30, 36, 37, 38]. SFIL requires a stamp made from a material that that is transparent to UV light, usually quartz. Thermosetting resists are also available, which rely on thermal energy to initiate solidification [33, 39]. The "classic" nanoimprint method [1], "hot embossing", engages a thermoplastic resist, the viscosity can be lowered by heating the resist to above the glass transition temperature [31, 40]. The heating required is typically provided by an oven environment for isothermal environments or a heated stamp for nonisothermal environments. The LADI method foregoes resists entirely, directly imprinting patterns into laser heated molten silicon [35].

Forming using solid resists is a different matter, bringing both advantages and disadvantages to the field. Glassy materials require somewhat higher stresses to cause deformation than in low viscosity resists, but as detailed in Chapter 6, optimisation of stress application can significantly increase efficiency. It also means that a large number of materials can be used and patterned directly that cannot usually be formed or withstand the physical extremes of other processes. The mechanisms for solid forming of glassy polymers are explained in more detail in section 2.5.

Multi-Level Structures

The ability to produce fully 3D structures with NIL could prove to be quite useful allowing for increased circuit complexity. This could be considered a step beyond the 2.5D examples described in section 2.2.2 above, whereby complex forming would be performed on a multilayer basis.

Examples of multilayer forming have been demonstrated [14]. Even the simplest crossbar structures could find uses in devices such as memory structures, multiplexers or FPGAs[3]. Reverse imprint has been demonstrated to be successful in creating such structures. This is a process where resist is spincoated onto a patterned mold

[3]Field Programmable Gate Array

and solidified, the patterned film can then be transferred to a substrate and the mold released. This can be performed onto a featureless substrate or an existing pattern and repeated. Other processes make use of materials so that the glass transition[4] of the material decreases with each layer, preventing previous layers from being deformed.

However, registering multiple layers over each other is a difficult problem especially when stamp features are on the scale of a few nanometers. Despite individual features being beyond the diffraction limit of visible light, methods are available using interference patterns created by Moiré fringes that propose to be able to align features to a level of 20nm [41].

2.2.4 Rheological Considerations

The key to understanding mechanical forming on the nanoscale is understanding the processes that govern the flow and deformation of material, otherwise known as rheology. When considering rheology as it applies to imprint we must examine, geometry, scaling, and constitutive responses of the materials in use.

A comparison with more traditional forms of lithography highlights the different nature challenges faced by NIL. In photolithography, an important factor is that of the mask ratio, also known as resist contrast. Ideally, after the exposure, development and removal of the unexposed resist[5], there is sufficient difference in the thicknesses of the exposed material and the unexposed material that further processing is not hindered. The mask ratio should be large enough that the remaining resist material protects the substrate directly underneath from processing, whether it be doping, etching, deposition etc. However the exposed areas of the substrate must be made susceptible to these processes. An unwanted residual layer of resist may mean an extra processing step. This can be considered costly and a possible point of failure when scaled up to

[4]The glass transition is a phase change associated with glassy materials where the material begins to make the transition from a solid to a liquid.

[5]Not all resists will behave in the manner described above, known as negative resist. The opposite may occur with removal of the exposed resist, known as positive resist.

large manufacturing operations. Uniformity of the residual layer (if any) is desirable to ensure uniformity of action of removal processes. For this reason, the concept of residual height is one of major importance within efforts to replace optical lithography with imprint lithography.

There is however a significant difference between optical lithography and imprint lithography and that is what happens to the material as it flows. This issue does not occur with optical lithography as there is no material transport during the pattern forming process and the resist can be removed with solvent after the exposure. Essentially, with imprint, what happens to the material during pattern forming is a major concern. The formed pattern must replicate that of the stamp, and as discussed below, there are many considerations that must be made to ensure fidelity is maintained.

A recurring aspect of NIL is the driving of deformation through compression, a process known as squeeze flow. NIL stamps can be thought of as a series of asperities which are used to apply stress to a susceptible material resulting in a duplication of the asperity. The process by which this geometry relates stress to strain is known as squeeze flow. A diagram of squeeze flow geometries can be seen in figure 5.9. Squeeze flow creates a combination of shear flow and extensional flow, which are differentiated by changes in the velocity of the material perpendicular and normal to the direction of the applied force [42]. The details of squeeze flow are well documented and studies on it's actual application to NIL have been carried out [40].

Combining squeeze flow with the filling of an adjacent cavity is also an important feature of NIL. Although it is possible to create high aspect ratio spaces adjacent to an asperity to prevent impedance of flowing material, it could be considered a greater advantage to attempt to control the filling of the cavities. The filling of the cavities is shown by experiment and model to fall into one of two modes, a single peak and a double peak. The filling modes are determined by the geometry of the system, namely the ratio of the polymer thickness to the width of the cavity at the start of flow and the evolution of the polymer supply as the imprint proceeds [43, 44].

By examining the rheological considerations, the design space for a particular system may be determined. The properties of a material may impose limits, such as a maximum temperature at which a given material is stable, thus limiting the forming temperature. Time also is a concern, for example, when considering manufacturing processes, reduction of processing time is a pressing goal.

Hot Embossing

Hot embossing resides in the regime of high temperature and short time spans, ensuring operation in a well characterised area of Newtonian flow. Reduction in temperature means higher viscosities and viscoelastic behaviour as well as possible phase changes, in which case solid forming behaviour must be considered. A Newtonian fluid cannot support a shear stress and will flow exhibiting a linear relationship between shear stress and strain rate, a viscoelastic material also cannot support a shear stress but may exhibit either a linear or non-linear relationship between shear stress and strain rate. The elastic component is manifested in behaviours such as shear thinning, creep, and hysteresis [42].

Forming of thermoplastics on the nanoscale was introduced in 1992 as an investigation into a method of high density data storage [45]. Chou et al. then introduced hot embossing as a lithography method [1]. Progress in these fields has made clear the need to understand the rheology of the processes.

Examination of the nature of the flows observed in nanoimprint are vital to obtaining the desired results. To simplify the analysis, hot embossing studies based on a flat single asperity contact (related to the squeeze flow model described above) have been undertaken [46, 47].

In his review of the subject, Cross relates (as determined by Joseph Stefan) that the forming load (L) , to maintain a constant stamp velocity in a fluid of zero-shear viscosity (η) scales with the thickness of the polymer layer (h) and the size of the stamp (R) [12],

$$L \propto \eta \frac{R^4}{h^3} \frac{dh}{dt} \tag{2.1}$$

This effect has been shown for isothermal embossing at a temperature of about 100°C above T_g, where as the film thins, a greater forming temperature is required to lower the viscosity or a longer time is required as at a constant load, the stamp velocity falls over time [46].

Glassy Polymer Forming

This project has focused on the imprint of glassy materials for several reasons. Forming of glassy materials implies that the operation is performed at 'room temperature' when materials are in the glassy phase. Khang et al. proposed the use of room temperature NIL motivated by problems with hot embossing such as the requirement of mold release agents and distortion of the mold and imprinted structures due to thermal cycling [48]. Within the imprint design space, many NIL processes restrict the choice of available materials. Many active materials lose their properties permanently when heated [49] or are unavailable as precursors for SFIL, also proving unsuitable for hot embossing. Crystalline materials are potentially problematic when attempting forming, features such as lattice defects, anisotropy and grain boundaries and which have the potential to cause problems such as the reduction of fidelity [50]. Glassy materials, being free from such defects, are better candidates for forming.

Unlike the techniques described above which describe low viscosity newtonian regimes, a solid maintains a yield stress and deforms only elastically until that yield stress is attained [51] (see section 2.3.2). Elasticity must then be accounted for when dealing with solid forming. Elastic recovery when the forming forces are withdrawn is a well documented phenomenon [47, 5] and this can conceivably reduce fidelity.

Equation 2.1 can also apply to glassy forming, where for a particular stamp size, a minimum thickness of the polymer layer exists. The apparent load on the stamp and polymer layer is limited because increases in load are absorbed as elastic strains by

the rest of the system, thus effectively limiting available stress to drive plasticity [4] (section 5.3.2).

Boundary Conditions

For all flow regimes, the effect of the boundary conditions, namely friction, is an important one. It is widely noted that in compression, a reduction of friction at the interfaces will reduce the forming stress [52, 53].

In deformations concerning normal loading, a phenomenon known as the Friction Hill is often used to explain certain aspects of material behaviour in compression. The friction hill describes the friction of an area as the ratio of the normal stress to the shear stress. The friction hill is discussed in greater detail in section 2.4.2.

Transport over both long and short ranges must be considered for successful reproduction of stamp features, which can be thought of as "material supply". Constrained material, unable to flow, is an issue which can conceivably lead to pattern non-uniformity and an undesirable residual height. Underfilling may occur, where not enough material exists locally to fill a cavity satisfactorily and also the converse, overfilling, whereby cavities fill and the surplus of material is locally constrained leading to an excess of residual material. This effect was demonstrated by Lee et al. [54] where complete filling of cavities prevented the stamp minimising the residual layer. Thus, a need for careful planning of stamp geometry, film thickness material sinks may be required.

Demolding

Adhesion between stamp and substrate is also an issue. Once a pattern has been impressed on a substrate, the stamp must then be removed from the substrate. Nanoimprint stamps typically sport a high density of nanoscale features, thus increasing the surface area. The increased surface area can lead to increased adhesion of the stamp to the imprinted material and resulting tensile forces on unloading may lead to un-

wanted plastic deformation or delamination. However Hirai et al. report that residual stress alone was responsible, citing that the combination of residual stress and thermoelastic stress from hot embossing followed by a rapid quench explained the results [55]. A more gradual cooling rate was found to reduce the thermoelastic stresses and lower the defect rate. Other methods exist to reduce unwanted adhesion. Reduction of the surface energy of the stamp in order to reduce adhesion through use of a chemical layer known as a release layer is a common method [21]. The release layer is a coating on the stamp a monolayer of fluorinated silanes or fluoropolymer [56, 57].

Cross notes that a mechanical treatment of the problem may be useful and postulates that the cause of demolding defects in polymers is due to viscoelastic crack propagation due to demolding occurring at temperatures close to T_g [12]. By embossing below the melting point or glass transition of the material, T_g, the polymer chains do not have enough energy or time to form attachments with the stamp [58]. Sub-T_g forming operations have been shown to exhibit low adhesion [3] and so lack these particular defects.

2.2.5 Overview

There are an enormous number of potential applications for nanoscale engineering. From ever decreasing transistor and interconnect sizes in semiconductors, to 'lab on a chip' systems [59] to cantilever balances which can measure the mass of a single virus [60].

Some of the more "traditional" methods of fabrication such as optical lithography are running out of steam as scales continue to shrink. Other methods such as electron beam lithography have a very low throughput. What drives the choice of fabrication method is economics, low throughput means high costs. Imprint lithography has enormous potential for high throughput over wide scale ranges and planar operation. While the science of embossing has been around for centuries, embossing on the nanoscale has revealed many challenges.

An investigation into nanoimprint and our investigations towards optimising this process based on the discoveries of ourselves and others are presented here. The instrumentation was chosen for this study to afford a live view of the deformation process in order to better understand and investigate NIL.

2.3 Basic Mechanics

To understand the mechanical behaviour of materials some relevant properties must be considered.

Stress, is defined as a force acting on an area. With an applied stress on a material, a change in the dimensions of the object under stress occurs, known as strain. Nominal stress (σ_n) is defined as force (F) per unit area (A). Nominal strain (ϵ_n), is defined as fractional change in length (l) of an elastic specimen under extensional stresses, (δl).

$$\sigma_n = \frac{F}{A} \tag{2.2}$$

$$\epsilon_n = \frac{\delta l}{l} \tag{2.3}$$

Nominal stress and strain and do not take into account plastic deformation and the resulting dimensional changes in the material. The concepts of true stress (σ) and true strain (ϵ) address this by taking these dimensional changes into account.

$$\epsilon = \int_{l_0}^{l_1} \frac{\delta l}{l} \tag{2.4}$$

$$\sigma = \frac{l}{A_t} \tag{2.5}$$

l_0 is the original length of the object and l_1 is the final value. A_t is the instantaneous

cross sectional area of the sample under test.

Stress and strain are related to each other by Young's Modulus, E. As long as the system remains linear, Young's Formulation states that

$$\sigma = E\epsilon \tag{2.6}$$

Values related to Young's modulus exist when dealing with cases of shearing or hydrostatic pressure. G is the shear modulus and for hydrostatic pressure there is a bulk modulus K. The bulk modulus deals with a change in volume, a 3-D quantity as opposed to a 1-D quantity such as length or shear.

2.3.1 Basic Elasticity

All of the above refer to purely elastic strain. Elastic strain is deformation which is instantaneous and reversible, so if a stress, is applied to an object and removed, the corresponding changes in the strain, will not be permanent.

An important quantity is the Poisson Ratio, ν. This relates strain in the direction of stress to strain in the transverse direction ($-\epsilon_t$) as seen in (eqn.2.7). The transverse strain is usually positive in compression, although there are exceptions[6]. The Poisson ratio makes it possible to relate the different moduli G, K and E to each other.

$$\nu = \frac{-\epsilon_t}{\epsilon} \tag{2.7}$$

The classic elasticity model for objects in contact is the Hertz model. The Hertz model describes the elastic deformation of a surface under an applied force from a rigid sphere, a diagram of which is shown in Fig2.2. σ_Z being the normal stress underneath the sphere which varies with the contact area radius of the sphere, a. This is normalised to the mean contact pressure, given as p_m, with r being the radius of the

[6]Some foam materials have a negative Poisson ratio [61]

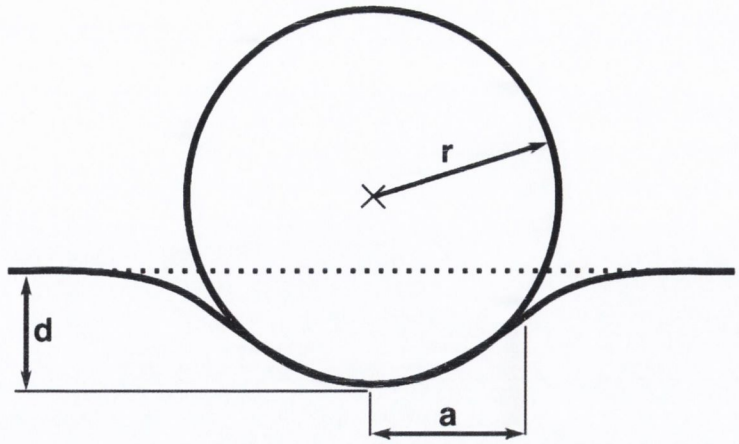

Figure 2.2: Schematic of Hertzian elastic contact. A rigid sphere under an applied force deforms a substrate. r is the radius of the sphere, a is the radius of maximum contact and d is the depth of contact.

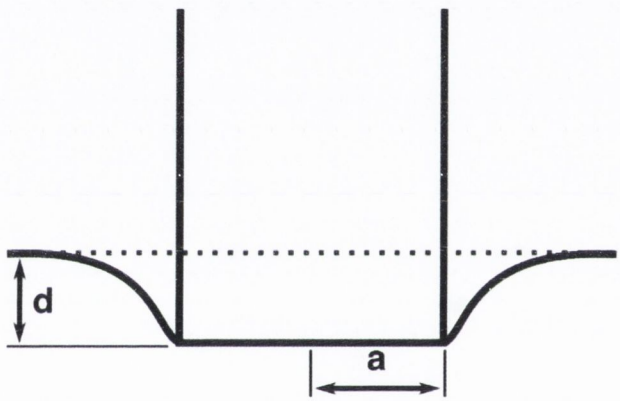

Figure 2.3: Schematic of Flat Punch elastic contact. A rigid cylindrical punch under an applied force deforms a substrate. a is the radius of the punch which is also equal to the radius of maximum contact and d is the depth of contact.

sphere [62].

$$\frac{\sigma_z}{p_m} = -\frac{3}{2}\left(1 - \frac{r^2}{a^2}\right)^{\frac{1}{2}} \tag{2.8}$$

For a cylindrical flat punch (shown in Fig.2.3), the normal pressure distribution may be written as follows, noting that for this geometry, r is equal to a.

$$\frac{\sigma_z}{p_m} = -\frac{1}{2}\left(1 - \frac{r^2}{a^2}\right)^{-\frac{1}{2}} \tag{2.9}$$

These models are important as they provide a method of evaluating the stress fields of contacts. For example, equation 2.9, describes stress being at a minimum at the center of the punch and approaching infinity at the edges.

2.3.2 Basic Plasticity

The onset of plasticity during a deformation is the point at which the system ceases being elastic and a permanent strain remains when external stresses are removed. This is typically identified in instrumented tests as a change in the slope of a stress-strain curve, which can usually be identified as the yield stress of the material [62]. Knowledge of the yield stress is essential, for example, knowledge of the maximum stress that may be applied to a system without unwanted deformation (otherwise known as failure) or optimising machining methods i.e. changing the boundary conditions by adding a lubricant to affect the machining of a material.

In polymers, plasticity may occur from very early on depending on geometry, such as areas of high stress at a corner. Even so, there is usually a point where bulk plasticity or yield "switches on".

The simple elastic models (eqns.2.8 & 2.9) are not sufficient to describe the onset of plasticity. Plasticity cannot occur without the presence of elasticity [63] as no system is purely rigid. A system response to a stress is typically elastic until a quantity known as the yield stress is surpassed whereby plasticity will occur.

Plasticity is driven purely by shear stress [64]. Figure 2.4 shows a kinetic model as described by Frenkel and Frank [51] which is used to describe hydrostatic stress and deviatoric (shear) stress. This model describes a material comprising of a lattice of "atoms" or "molecular components" which are connected to each other by springs. In the figure, *A1* is a lattice of these components at equilibrium with each other with an inter-component spacing, d. In order to change the inter-component spacing, a force must be applied, corresponding in the change of the energy of the bond potential, U. If a hydrostatic force is applied, *A2*, the spacing, d changes. As d decreases, the force

required to do so rises as shown in the graph. Unless failure of the material occurs, removing the force will cause the system to return to the state *A1* as there are no other possible equilibrium positions available.

B1 depicts a lattice similar to *A1*. Instead of a hydrostatic force, a shearing force is applied (*B2*). As expected, the force causes strain. Continued application of force allows the components to exist in a new equilibrium position (*B3*). The deformation resulting in *B3* is permanent and the system will not return to *B1* when the force is removed. Another point to note in the shear system is that if the force is not removed, the system will continue to deform through the successive motion of components into available equilibria positions.

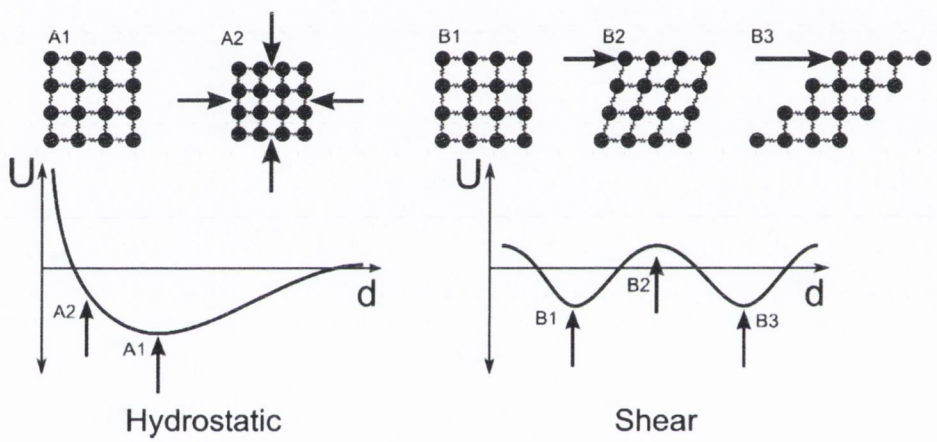

Figure 2.4: Kinetic model of plasticity for Hydrostatic stress *A*) and Shear stress *B*). *A1* is a lattice of these components at equilibrium with each other with an intercomponent spacing, d. Application of hydrostatic force, *A2*, results in a uniform change in d. Application of shear stress to *B1* results in a strain, *B2*. However, the straining allows a new equilibrium to form, *B3*.

The Frenkel-Frank model applies not just to crystalline solids but also to small molecule glasses and polymers. In these cases similar rules apply, whether they by single atoms, small molecules or polymer chain segments.

More practical models for plasticity exist, one of the simplest mathematically being the Tresca criterion (eqn. 2.10). It describes a hexagonal "envelope" or "surface" in principal stress space[7] which defines a critical value for shear stress τ_T, beyond which

[7]Considering a structural element under stress, the shear and normal stresses vary with

yield will occur. This is calculated from the largest principal stress σ_1, and the smallest principal stress, σ_3.

$$\tau_T = \frac{1}{2}|\sigma_1 - \sigma_3|_{max} \tag{2.10}$$

However, it is often difficult to obtain values for σ_1 & σ_3 outside experiment and so the von Mises yield criterion (eqn. 2.11) may be preferable from a practical point of view while producing similar results to the Tresca criterion. In this case the yield surface is cylindrical, circumscribing the 6 points of the Tresca surface. The von Mises criterion τ_{oct}, depends on the principal shear stresses, given by the differences between normal stresses, σ_1, σ_2 and σ_3 and so,

$$\tau_{oct} = \frac{1}{3}\Big((\sigma_1 - \sigma_2)^2 + (\sigma_2 - \sigma_3)^2 + (\sigma_3 - \sigma_1)^2\Big)^{\frac{1}{2}} \tag{2.11}$$

Although these two plasticity methods may produce slightly different results, usage may be determined by ease of use and availability of data as well as the behaviour of the material.

When dealing with glassy polymers, certain aspects of material behaviour must be considered. Experimental data shows that an increase in hydrostatic pressure can lead to a significant increase in the yield stress [51]. Models such as the pressure modified von Mises & Tresca [51] [65] were developed to account for the presence of hydrostatic pressure, p.

$$p = \frac{1}{3}\Big(\sigma_1 + \sigma_2 + \sigma_3\Big) \tag{2.12}$$

The effects of hydrostatic pressure can be accounted for in the following equations, the pressure modified Tresca criterion (eqn. 2.13) and pressure modified von Mises (eqn.

rotation of the element. At particular points the values of the shear stresses are zero and the only existing stresses are those normal to orthogonal planes of the rotated element, these are known as the principal stresses.

2.14).

$$\tau_T^Y = \frac{3}{\sqrt{2}}(\tau_T^0 + \alpha p) \tag{2.13}$$

$$\tau_{oct}^Y = \tau_{oct}^0 + \alpha p \tag{2.14}$$

τ_T^0 and τ_{oct}^0 are the yield stresses for pure shear scenarios, which are added to the factor of the coefficients of hydrostatic pressure and internal friction, α.

Some numerical and experimental studies have shown that the pressure coefficient is generally an independent parameter. These studies also suggest that the usage of a particular model is dependent on whether or not the material under investigation forms shear bands. The von Mises criterion is shown to be the most suitable for materials that undergo homogeneous deformation and the Tresca would be more suitable for materials that exhibit shear banding[8] [66] [67]. A more detailed discussion of the mechanisms of plasticity in polymers is dealt with in section 2.5.

2.4 Forming Analysis

Having considered the basic behaviour of materials under stress, the next step is that of investigating more complex behaviour. Production of non-uniform patterns via NIL means that complex stress fields are produced which must be understood to optimise the process. Some methods of visualising the stresses and strains are discussed here.

2.4.1 Cavity Model

To take elasticity into account, the cavity model postulated by Johnson [9] allows for differing states of stress for a material under compression. Initially during a com-

[8]Shear banding is a phenomenon whereby areas of undeformed material are criss-crossed by bands of material that have undergone high shear.

pressive deformation such as an indentation, the displacement of the indenter into the solid is translated into elastic strains. If the applied pressure is increased, then eventually the yield point will be exceeded and a plastic zone will occur. Continued increases in applied stress will result in an increase of the plastic zone as more and more of the material exceeds the yield stress, Y. This plastic zone will be contained by the expanding elastic zone until the plastic zone reaches the surface and breaks free. This is known as the uncontained plastic mode and is defined by the threshold $p_m = CY$. The constant C is the constraint factor and is also seen in the definition of hardness, $H = CY$. The constraint factor is dependent on the properties of the indenter and surrounding material, specifically the E/Y ratio of the material [68].

Based on experimental and numerical data [9] the cavity model assumes of a hemispherical core of hydrostatic component, radius, a. The hydrostatic core is an area constrained by the rigid tip and the surrounding plastic zone. As it is constrained on all sides, the material in the core can only behave elastically. For blunt conical indenters, this core radius is equal to the contact radius. This is surrounded by a plastic zone of radius c which is in turn surrounded by a long range elastic zone. A diagram illustrating this is shown in figure 2.5.

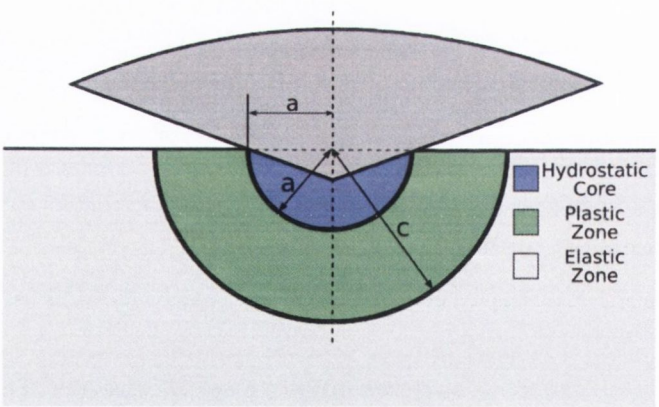

Figure 2.5: Schematic of expanding cavity model for a blunt conical indenter. The dimensions of the the hydrostatic core radius a is equal to the contact radius of the indenter. This is surrounded by a plastic zone of radius c which is in turn surrounded by a long range elastic zone.

The cavity model allows for some predictions to be made about the states of stress under an indenter. We can obtain the stresses σ_r, σ_θ at a particular point r in the

plastic zone ($a \leqslant r \leqslant c$) allowing the core pressure to be obtained at the core boundary where $r = a$. The elastic plastic boundary can be located by assuming self similarity of the indenter tip ($dc/da = c/a$) and conservation of the core volume, whereby for an increment of the indenter depth, the volume of material crossing from the core to the plastic zone is equal to the volume of material displaced by the indenter tip.

For an increase in indentation depth, the zone boundaries must move and it can be demonstrated that the resulting displacements in a and c arise and are given by,

$$\frac{du(a)}{dc} = Y/E\{3(1-\nu)(c^2/a^2) - 2(1-2\nu)(a/c)\} \tag{2.15}$$

and conservation of the volume of the core as the indenter moves into the material requires,

$$2\pi a^2 du(a) = \pi a^2 dh = \pi a^2 \tan\beta da \tag{2.16}$$

giving the following equation, from which the extent of the elastic plastic boundary can be determined,

$$\frac{E\tan\beta}{Y} = 6(1-\nu)(c/a)^3 - 4(1-2\nu) \tag{2.17}$$

where β is the angle made between the tip and the surface, ν is the Poisson Ratio, and E is the modulus of the material.

A simpler version of eqn.2.17 is the following, given by Lee et. al [69], where P is the load on the sample and σ_{ys} is the uniaxial yield strength.

$$c = \left(\frac{3P}{2\pi\sigma_{ys}}\right) \tag{2.18}$$

Now that both c and a can be evaluated, the pressure in the core can be obtained by,

$$\frac{\bar{p}}{Y} = \frac{2}{3}\left\{1 + \ln\left(\frac{1}{3}\frac{E\tan\beta}{Y}\right)\right\} \tag{2.19}$$

The usefulness of a self similar system is evident again as it allows for the mean pressure to be calculated for a particular strain as well as surface and subsurface

stresses.

The cavity model has proven to be a satisfactory model for conical and spherical indenters, providing results in general agreement with experimental results. Experiments using PMMA have revealed evidence for the existence of the plastic zone and hydrostatic core [70]. Indentations of PMMA with conical indenters of various angles visually shows the presence of two zones, an "anomalous zone" and a "dead zone", analogous to the plastic zone and hydrostatic core respectively. The anomalous zone exhibits a change of refractive index and the dead zone appears opaque. A notable point is that the elastic relaxation of the dead zone when the indenter is removed is similar to the non-uniformity of the residual layer observed in section 5.3.

2.4.2 Boundary Conditions

The state of boundary conditions can result in a marked change of the behaviour of a material being tooled [9]. Friction and yield stress would be examples of significant boundary conditions experienced in contact mechanics. For example, changes in boundary conditions can be such that the coefficient of friction of can be determined by the nature of deformation of a ring in compression [52].

Boundary conditions can produce undesirable effects, such as friction leading to an increase in yield pressure [64] and are commonly modified to avoid such. Traditional lubrication serves to reduce friction and ultrasonic forming utilises friction to heat the areas in contact, producing a lubricating layer [71]. However, friction can be utilised in other ways. Finite Element Modeling of variations of boundary conditions shows that a condition of full-stick aids in the transmission of strains through a point of contact [7]. This is of great benefit in the process of Small Amplitude Oscillatory Shear Forming (SAOSF), described in greater detail in chapter 6.

Friction Hill

One effect of boundary conditions in compression forming is the phenomenon of the "friction hill". During contact of surfaces, a combination of shearing and normal stresses arise. Shear stresses lead to friction at the interfaces and as the pressure increases, the friction opposes the outward motion of the deforming material [72, 64]. The friction (μ) can be related to the shear stress (τ) and the normal compressive stress (P),

$$\mu = \frac{\tau}{P} \tag{2.20}$$

The yield criterion for this model can be written in terms of principal stresses as,

$$\sigma_0 = \sigma_r + \sigma_Z \tag{2.21}$$

where σ_r and σ_Z are the radial stress and the normal stress respectively and σ_0 is the uniaxial yield stress. The maximum pressure is exists at the zero radius where the friction is also maximum, as demonstrated in the example of compression of a cylindrical billet shown in figure 2.6 and described by the following equation,

$$P = \sigma_0 e^{\frac{2\mu}{h}(a-r)} \tag{2.22}$$

which gives the pressure (P) at a radial point (r) inside the contact radius (a) of a billet of thickness (h).

In this geometry, the presence of the friction hill is revealed by the bowing of the sides and the presence of what is known as the dead zone. The dead zone is analogous to the hydrostatic core in the Johnson Cavity Model [73] (section 2.4.1), the difference being the constraint of the material arises from the friction at the boundaries, not merely the surrounding material. The bowing of the sides is caused by the friction preventing motion at the interfaces while motion occurs as expected away from the interfaces. The

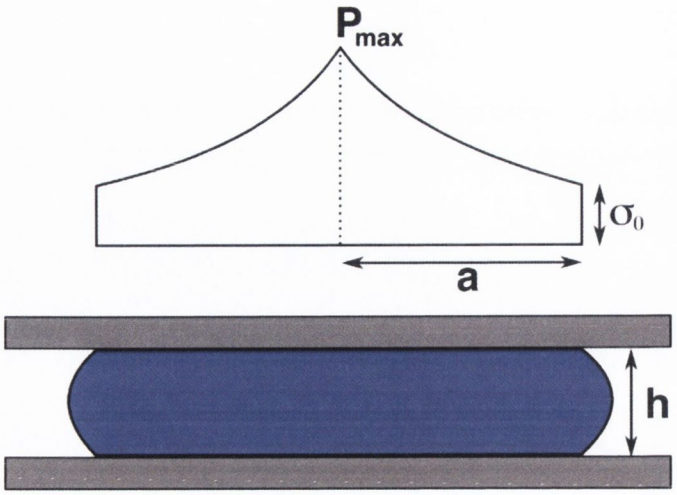

Figure 2.6: Schematic of friction hill for a billet under compression with full stick conditions.

occurrence of the dead zone is caused by the friction opposing the shearing stresses thus preventing plasticity. Although conditions such as full stick and full slip can exist, there is often a gradient which can alter the shape of the friction hill.

The effect of the friction hill and the associated dead zone cause inhomogeneities in the deformed material as noted above. These effects can be negated by reducing friction at the interfaces thus reducing the extent of the friction hill, hence the use of teflon shims, lubrication and high frequency vibrations when forming [74, 75]. The friction hill also causes the deformation pressure to climb as the a/h ratio increases. This means that as the object under deformation becomes thinner or as the area of contact becomes larger, it becomes more difficult to drive plasticity using compressive loads.

2.5 Properties of Glassy Polymers

This section discusses the behaviour of glassy polymers in greater detail due to their prominence in this project. Glasses are amorphous solids, typified by the lack of a melting point. Instead there exists a glass transition temperature (written as T_g), the temperature at which the segue between the liquid and glassy solid state occurs. To understand the behaviour of glasses, some concepts must be considered, such as the

reason for the glass transition itself and free volume.

2.5.1 Glass Behaviour

Glassy polymers generally display viscoelastic behaviour which can be split into 5 regimes with increasing temperature [58].

Glassy.

Below the glass transition temperature (T_g), molecular motions are restricted to vibrational and rotational movements. The material appears brittle and most glassy polymers have a modulus of 3GPa in this phase. Creep may exist, but is essentially negligable.

Glass Transition.

This is characterised by a drop of the modulus of 2 to 3 orders of magnitude as long range co-ordinated molecular motion is allowed. The number of backbone atoms involved in a movement increases from 1 to 4 ($sub - T_g$) to 10 to 50 . Certain conformational properties such as tacticity may affect the behaviour.

Rubber plateau.

Long range plasticity typifies the rubber plateau. Again tacticity may play an effect, but the dominating factor is crosslinking. The existence of crosslinks results in an extended zone of elasticity, while the absence of cross-links permits creep.

Rubber Flow.

Rubber flow behaviour is time and chain length dependent. On short time scales, the polymer chains cannot move vary far permanently and the material appears elastic.

Over longer times, the material will creep or flow. Rubber flow does not occur for crosslinked polymers as the crosslinks prevent large scale chain motion.

Liqud Flow.

There is now enough energy in the system for the chains to flow as individual molecules and this results in liquid like behaviour.

2.5.2 Detailed Eyring Description

The Eyring equation describes transport on a molecular scale. To understand the Eyring equation as it relates to strain in a glass, consider 2 sites, #1 and #2, separated by an energy barrier (ΔG) where G is the Gibbs energy. A chain segment of a polymer molecule may cross back and forth across the barrier if it has enough energy (represented by the product of the gas constant R and the temperature T) to do so. The probabilities of transition, ω_{12}^0 (forward) and ω_{21}^0 (back) are given by,

$$\omega_{12}^0 = A' \exp\left(-\frac{\Delta G_1}{RT}\right) \text{ and } \omega_{21}^0 = A' \exp\left(-\frac{\Delta G_2}{RT}\right) \tag{2.23}$$

where A' is a pre-exponential factor that empirically relates the rate of transitions to the temperature.

Application of stress changes the free energies involved, resulting in an apparent lowering of the barrier heights to δG resulting in changes to the probability of a chain segment crossing the barrier in either direction ω_{12} & ω_{21},

$$\omega_{12} = \omega_{12}^0\left(1 - \frac{\delta G_1}{RT}\right) \text{ and } \omega_{21} = \omega_{21}^0\left(1 - \frac{\delta G_2}{RT}\right) \tag{2.24}$$

These probabilities can be associated with rates based on the number of species occupying each state, n. Every member of the population that crosses the barrier has an associated strain, expressed as $n\bar{\epsilon}$ and when combined with total elastic deformation

ϵ_u, the total strain ϵ is

$$\epsilon = \epsilon_u + n\bar{\epsilon} \tag{2.25}$$

This system can be expressed in a more practical sense as follows, equation 2.26 is a form of the Arrhenius equation [76]. With no external stress, the frequency of molecular movements (ν) across the barrier can be shown to be,

$$\nu = \nu_0 \exp\left(-\frac{\Delta H}{RT}\right) \tag{2.26}$$

with ΔH being the the activation energy (where H is the enthalpy of the system, the energy available to do work), based on the energy available to a particular molecular segment. The rate of molecular movements is described by ν_0, related only to temperature as shown in equation 2.27 where k_B is the Boltzman constant, and h is the Planck constant.

$$\nu_0 = \left(\frac{k_B T}{h}\right) \tag{2.27}$$

Applying a stress, introduces an asymmetry of forces, which leads to an effective change in the barrier height and is shown in figure 2.7. This can then be described by the following equation,

$$\nu_1 = \nu_0 \exp\left(-\frac{\Delta H - \beta\sigma}{RT}\right) \text{ and } \nu_2 = \nu_0 \exp\left(-\frac{\Delta H + \beta\sigma}{RT}\right) \tag{2.28}$$

where ν_1 and ν_2 are the rates of molecular movement in each direction and ΔH is the enthalpy of the system. β has dimensions of volume, and can be considered as the volume of material moved across the energy barrier. β is comparable to the activation volume of the polymer v, as shown in equation 2.29.

The strain rate of the system $\dot{\epsilon}$, is proportional to the frequency and can be written as,

$$\dot{\epsilon} = \dot{\epsilon}_0 \exp -\left(\frac{\Delta H}{RT}\right) \sinh\left(\frac{v\sigma}{RT}\right) \tag{2.29}$$

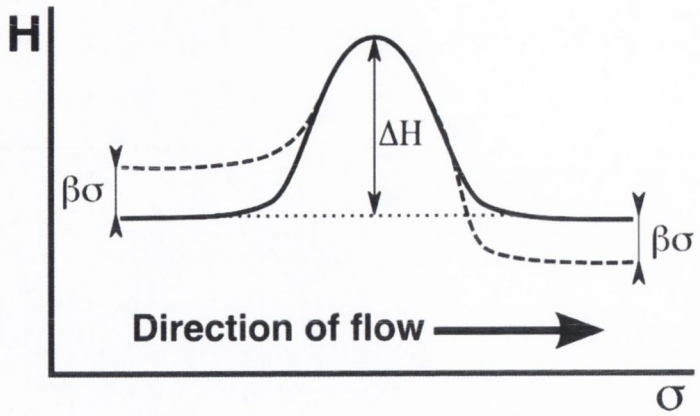

Figure 2.7: The Eyring Model under an applied stress

where $\dot{e}_0$ is a strain factor similar to ν_0 in equation 2.27 and v is the activation volume of the material in question. For large strains, this process becomes analagous to equation 2.33. The activation volume represents the volume of a polymer segment which can move as a whole and produce a permanent deformation [76, 77]. As the activation volume increases, the greater the length of polymer chain which can move in a given energy fluctuation.

2.5.3 Free Volume Theory

The free volume theory provides a mechanism for glass behaviour and relies on the presence of existing voids within the polymer matrix. Glassy polymers being amorphous, are randomly packed and like all other solids contain some degree of free volume. Free volume is essentially unoccupied voids or empty inclusions within the molecular matrix. These voids provide areas into which chain segments can move if they have the energy to do so, the probability of which is described by the Eyring equation, detailed above (section 2.5.2). Assuming the amount of free volume in a polymer remains constant, above T_g the free volume of a polymer (v_f), may be expressed as,

$$v_f = \kappa_0 + (\alpha_R - \alpha_G)T \tag{2.30}$$

α_R is the volumetric coefficient of expansion in the rubber phase, and α_G that of the glass phase, T is the temperature of the sample and κ_0 is the supposed free volume at 0K.

Free volume can cause some undesirable effects, causing variations in density and structural properties. In order to reduce the free volume, a technique called annealing is often used. Annealing is a common process used with glasses where the material is cooled slowly to room temperture from a temperature close to or above T_g. Annealing provides enough thermal energy so that the molecules can move and settle into the positions with the lowest available energy. Annealing avoids the "freezing" in of free volume, which results from the thermal expansion of the molecular chains at higher temperatures. It should be noted that some studies show that for annealed films, the presence of an interface creates a modulation of the glass transition temperature [12].

An excess of free volume can also be caused through the use of solvents when dealing with polymer solutions, whereby the solvent molecules evaporate leaving inclusions. Processes may also influence the free volume, such as spincasting where the material is subject to centrifugal force and the forces inherent with the spincasting geometry can cause gradients of [78].

It has been noted that hydrostatic forces are not generally the cause of plastic deformations (which are usually volume preserving). However hydrostatic forces may remove free volume in a material producing plastic deformation (see section 5.3.1) [58, 51]. Nevertheless, it has been verified experimentally that hydrostatic forces raise the yield stress in materials [51]. Referring back to the Frank-Frenkel model in section 2.3.2, this can be explained by the hydrostatic pressure raising the energy barrier height between equilibrium positions, thus requiring more energy to traverse the barrier.

2.5.4 WLF theory

WLF (Williams, Landau & Ferry) theory defines the relationship between the viscosity of a fluid polymer and the amount of free volume. This is notable as it postulates that flow will not occur without sufficient free volume. WLF theory relates the probability of a chain segment moving into a vacancy, to time and temperature. Essentially this states that a change in the time scale will have the same effect as a change in temperature. Given enough time, a chain segment will move into a vacancy, increasing the temperature merely provides enough energy to increase the likelihood of such an event. Equation 2.31 is the basic WLF equation.

$$\ln A_T = -\frac{(B/\kappa_{T_0})(T - T_0)}{(\kappa_{T_0}/\alpha_f) + (T - T_0)} \tag{2.31}$$

A_T is the reduced variables shift factor, which relates time dependent quantities to the change in time scale, ($\ln A_T = \Delta \ln t$). B is a constant, κ_{T_0} is the fractional free volume at a transition temperature T_0 and α_f the expansion coefficient of the free volume.

Using experimental data for the relevant materials at particular temperatures, the constants for equation 2.31 can be expressed as shown in equation 2.32 (in this case, for linear polymers $C_1' = 17.44$ and $C_2' = 51.6$). Equation 2.32 is an example of a practical version of the WLF equation which is expressed as the log of the ratio of the viscosity, η, at temperature T and the viscosity at the glass transition η_{T_g}.

$$\log\left(\frac{\eta}{\eta_{T_g}}\right) = \frac{-C_1'(T - T_g)}{C_2' + (T - T_g)} \tag{2.32}$$

In amorphous polymers, plastic flow can be considered viscous with the yield stress being strain rate dependent. If the temperature is increased, the yield stress drops and becomes equal to zero at the glass transition temperature (T_g). At this stage, chain mobility is such that the material behaves as a liquid with viscosity depending on chain length.

Many things can affect the yield point besides temperature, molecular weight (M_W), tacticity, residual stress and additives. Increasing the chain length means the number of entanglements associated with an individual chain are increased and the motion of the chain through the matrix is impeded [58]. Side chains and side groups and their associated frequency and arrangements on the primary chain can also impede motion. Small molecules such as plasticisers can act in a similar manner to free space.

Equation 2.33 is the Eyring description of the plastic strain rate ($\dot{\epsilon}$) as it relates to the conditions the polymer is under. Most attempts to optimise forming by improving the plastic strain on this level involve increasing the temperature of the system T, or by lowering the activation energy E_a by shortening chain length.

$$\dot{\epsilon} = \dot{\epsilon}_0 \exp - \left(\frac{E_a - \sigma v}{k_B T} \right) \tag{2.33}$$

As discussed in Chapters 5 and 6, increasing the stress σ, in order to attain plastic yield only works to a certain extent. High stresses result in undesirable elastic deformation of the stamp and limited gains of yielded material. The aim of this project was to examine and optimise the forming process, as altering E_a is not always viable and increasing T prohibits the use of active materials, many of which are thermally sensitive.

2.6 Indentation theory

Indentation is a mechanical method of determining the properties of a material where a tool of known properties and geometry is brought into contact with a material of unknown properties and by applying sufficient force the material under test is deformed. Under an applied load the indenter tip moves into the specimen, deforming it. By examining the geometry of the remaining deformation after the tip is removed, properties such as hardness and modulus can be determined. Nanoindentation reduces the scale of the experiment so that measurements are in the nanometre & nanonewton

regime. [68].

Indentation data can be obtained in two ways, a standard form (described in the paragraph above) and a more advanced dynamic method, hereafter referred to as "DC" and "AC"[9] mode respectively.

Although this project used standard nanoindentation methods to characterise many of the samples used, the primary purpose of the tool was not to perform indentation in the traditional sense. The ability of the nanoindenter to make highly accurate and repeatable force applications and displacement measurements allowed single feature imprints to be made and characterised. Examination of the behaviour of single features revealed insights to the processes of deformation and allowed optimisations based on the findings.

2.6.1 Standard Intentation Testing (DC)

As already described, indentation techniques involve pushing a machined tip into a material thus causing deformation of the material under test. The size and shape of the resulting indentation after removal of the tip is related to the properties of the material under test. However on nanoindentation scales the indent would be very small and difficult to characterise optically. Knowledge of the tip geometry allows this problem to be overcome, as does examination of the resulting indents with Atomic Force Microscopy (described in section 4.6). Two tips were used in this project, a cube corner and a Berkovich tip[10]. The cube corner is a 4 sided pyramid with a semi-angle of 35.26°. The Berkovich tip is a three sided pyramid with an semi-angle of 65.3°. A useful property of pyramidal tips is self similarity, where the ratio of the width of the tip to the depth is a constant. For a Berkovich tip, the representative strain has a value of 8% and during an indentation, the strain (and hardness measurement) is independent of the load [68].

[9] Although not strictly correct, the AC/DC terminology provides a shorthand to distinguish between the two methods

[10] A myriad of other tips exist, e.g. Knoop, Vickers, conical & spherical.

Obtaining an accurate value for the contact area of the tip depends on the depth of the tip into the sample and tip shape. Although the tip conforms to a well defined specification, imperfections may exist which introduce errors to the measurement. Direct measurement of the exact tip shape is difficult (if not impossible) but a reasonable approximation can be obtained by the Oliver-Pharr method [79]. By indenting the tip into a homogeneous sample of known properties, the tip shape can be inferred. Typically, fused silica is used for the calibration of the tip because it tends not to to produce "pile-up" of material surrounding the tip, which would create an artificial increase in tip contact area. The data obtained from the calibration is a series of coefficients (C_n) which can be fitted to produce a function relating the contact area (A) to the indentation depth (h_c) (eqn.2.34).

$$A = \sum_{n=0}^{8} C_n (h_c)^{2-n} \tag{2.34}$$

For an ideal Berkovich tip, the area function can be written as follows where h_p is the depth of plastic penetration,

$$A = 24.5 h_p^2 \tag{2.35}$$

One of the simplest values that can be obtained through nanoindentation is hardness, (H), the ability of a material to resist plastic deformation. This can be determined by the load on sample (P), divided by the area of the indenter tip in contact with the sample.

$$H = \frac{P}{A} \tag{2.36}$$

To obtain measurements such as modulus (E), a load displacement curve is produced using the indenter. Figure 2.8 gives an example of such a curve showing a typical elastic-plastic loading curve (as well as an example of a purely elastic loading curve) and the unloading slope, the initial part of which is purely elastic. The y axis is the applied load P, the x axis is the displacement into the surface h, h_r indicates the plastic

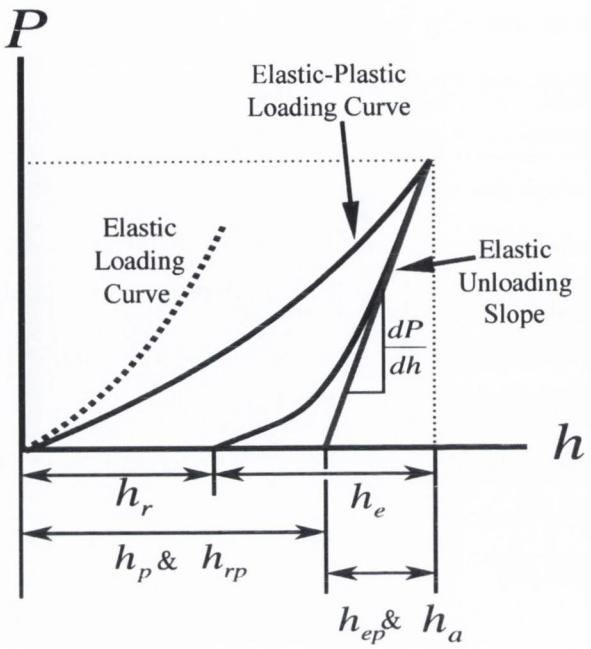

Figure 2.8: Typical Load-Displacement nanoindentation curve to a Berkovich tip. P is the applied load, h is the displacement into the surface, h_r indicates the plastic depth after the indent, and h_e is the elastic recovery.

depth after the indent, and h_e is the elastic recovery.

The measured modulus, may be measured by obtaining a value for the stiffness of the system (S) from the initial part of the unloading slope,

$$S = \frac{\delta P}{\delta h} \tag{2.37}$$

From there, the geometry is taken into account allowing a value for the effective modulus (E_{eff}) (the combined modulus of the tip and sample) to be determined.

$$S = \beta \frac{2}{\sqrt{\pi}} E_{eff} \sqrt{A} \tag{2.38}$$

β is a tip geometry correction[11]. The modulus of the sample may be obtained from the

[11]It should be noted that $\beta = 0$ for a cylindrical flat punch, which was a very common stamp geometry in this project and thus renders some of these calculations invalid.

effective modulus of the system,

$$\frac{1}{E_{eff}} = \frac{1-\nu^2}{E} + \frac{1-\nu_i^2}{E_i} \tag{2.39}$$

where E and ν respectively are the modulus and Poisson ratio of the specimen and E_i and ν_i refer to the already known modulus and Poisson ratio of the indenter tip, which is typically made from diamond. Whilst it is useful to know ν for the sample under test, it is not absolutely necessary as the calculation turns out to be rather insensitive to variations in ν and an approximation will suffice in most cases.

2.6.2 Dynamic Indentation Testing (AC)

It is possible to dynamically measure the properties of the sample, augmenting the "DC" method. By superimposing a force controlled small amplitude low frequency oscillation onto the normal indenter DC behaviour for loading and unloading, it is possible to measure the contact stiffness throughout the entire test. This is advantageous over determining E from the unload slope and can measure events such as the evolution of strain hardening during the load segment. This method also allows the initial contact of the indenter with the test surface to be determined with some accuracy [68].

The superimposed oscillation is typically on the order of $1-3$nm at $\sim$45Hz. The hardware to support this method is provided by the Continuous Stiffness Measurement (CSM) module. The CSM is essentially a lockin amplifier and is used to determine the phase difference between the excitation signal and actual displacement, thus measuring the storage and loss components of the material under test. As described below, from the measured phase difference, the Harmonic Contact Stiffness (HCS) is obtained. The HCS is analogous to the stiffness, S acquired from the unload curve (see eqn. 2.37), only it is measured dynamically throughout the whole test.

The indenter and sample can be described as a spring and dashpot network. For an applied AC force p, of frequency ω and amplitude p_0, a displacement h, arises with a

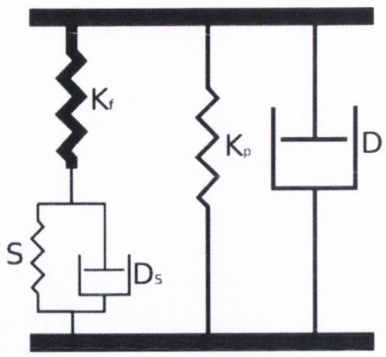

Figure 2.9: Spring and dashpot representation of indenter components. S and D_S represent the stiffness and damping respectively associated with the sample with K_f being the stiffness of the indenter frame. K_p and D are the stiffness and damping of the indentation shaft.

phase difference ϕ and amplitude h_0 [68].

$$p = p_0 e^{i\omega t} \text{ and } h = h_0 e^{i(\omega t \phi)} \tag{2.40}$$

Analysis of the model described in figure 2.9 returns the relationship between p_0 and h_0, with m being the mass of the system.

$$\left|\frac{p_0}{h_0}\right| = \sqrt{\left(\left(\frac{1}{S_h} + \frac{1}{K_f}\right)^{-1} + K_p - m\omega^2\right) + \omega^2 D^2} \tag{2.41}$$

Equation 2.41 can be rewritten in terms of the phase difference with the help of the relationships described in equation 2.40.

$$\tan\phi = \frac{\omega D}{\left(\frac{1}{S_h} + \frac{1}{K_f}\right)^{-1} + K_p - m\omega^2} \tag{2.42}$$

This allows the only unknown, S_h, to be calculated and this is the Harmonic Stiffness, the stiffness of the whole system. S_h does not take into account the fact that the frame is not perfectly rigid and will comply with an applied load, thus affecting measurements. However, the indenter itself is a very stiff spring of known stiffness in series with a less stiff spring (the sample), shown in figure 2.9. The corrected value is

the HCS, and is calculated as shown in equation 2.43. This essentially allows for the compliance of the frame as the load upon the sample is increased.

$$HCS = \frac{1}{\frac{1}{S_h} - \frac{1}{HF+HFC}} \tag{2.43}$$

The Harmonic Stiffness, the stiffness of the frame and sample combined is calculated on the fly by the hardware by the method detailed above. HF is the Harmonic Frame Stiffness, this is a constant and this has a value of $8,200,000 N/m$. The HFC is the Harmonic Frame Correction and has a value of 0 by default, but can be defined by the user to correct for errors introduced by other elements in the system if their stiffness is known. The Frame Stiffness is further discussed in the instrumentation section 3.1.

Figure 2.10 displays the increasing influence of stage compliance on the measurement (in this particular case, a cube corner being indented into a fused silica standard). As the load is increased, the indenter frame complies and this appears as a reduction of sample stiffness. This is visible as the lower curve diverges from the corrected curve as the load increases.

The modulus E, can be calculated in the following manner. Firstly, the reduced modulus E_r (the modulus of the entire system, indenter and sample) is determined from the HCS, the contact area A_p and β is a factor related to stamp geometry.

$$E_r = HCS\frac{\sqrt{\pi}}{2\beta\sqrt{A_p}} \tag{2.44}$$

As the modulus of the indenter tip is known, then the modulus of the sample can then be calculated. Hardness is defined as

$$H = \frac{P}{A_p} \tag{2.45}$$

the load (P) divided by the harmonic contact area (A_P). Although the equation is

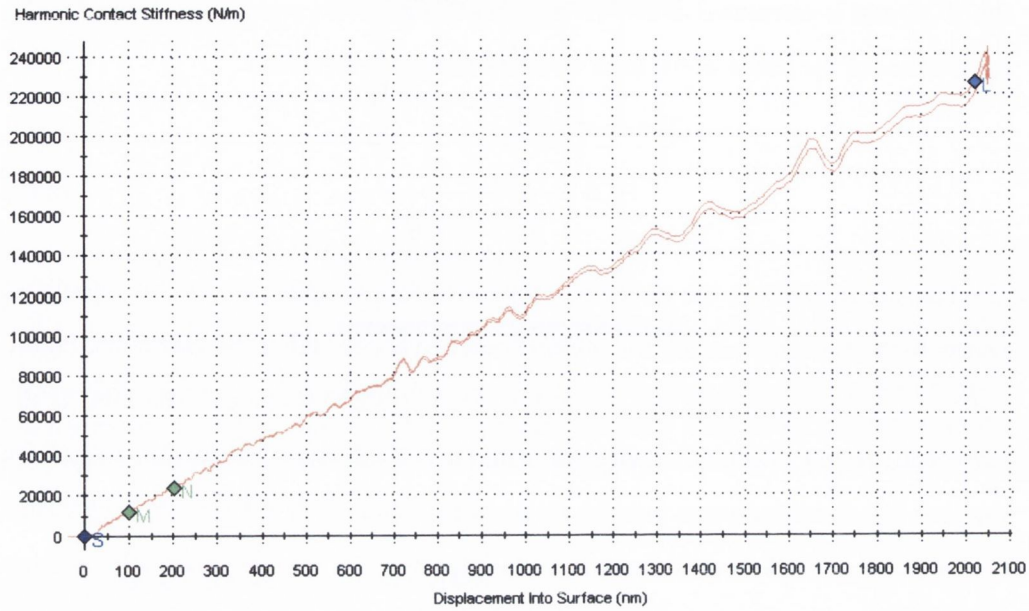

Figure 2.10: Divergence of Harmonic Stiffness (combined stiffness of frame and sample) and Harmonic Contact Stiffness (which includes corrections for frame compliance with increasing load.

similar for AC and DC methods, A_P is calculated using the harmonic contact stiffness (equation 2.46) as opposed to the indenter shape function in equation 2.35.

$$A_P = \frac{h - \epsilon P}{S_h} \tag{2.46}$$

All of these methods rely on the tip geometry being known, hence the prominence of the tip geometry factor and contact area. During this project, the use of unorthodox stamps of differing geometries and delicate materials has prevented quantitative measurements being made directly using this method. However, with all relevant variables remaining constant during a test, conclusions have been reached using qualitative comparisons. The load, displacement and HCS measurements remain the cornerstone of all conclusions reached during this project.

Another advantage of using the AC method is the improvement of surface detection. As this method is so sensitive, a very slight change in the phase angle indicative of damping allows even imminent contact with the surface to be detected, although care

had to be exercised with soft surfaces such as polymer close to or above T_g. This is especially useful for use with delicate samples and tips.

Chapter 3

Instrumentation

This section describes the instrumentation used in this project. The central instrument for the project was the MTS Nano Instruments nanoindenter which performed the imprinting and the materials characterisation through indentation. Other main instruments included an Atomic Force Microscope (AFM) and Electron Microscope (EM) with Focused Ion Beam (FIB) capability.

3.1 Nanoindentation

To examine the flow processes involved in the experiments being conducted, it was of high importance that the applied forces and resulting displacements be measured with great accuracy and repeatability. The MTS Nanoindenter[1] was chosen not only because it could provide such qualities but because it afforded a high level of control and flexibility, as well as an unmatched dynamic range of displacement and applied load measurement. Testworks, the control software, provided an environment where every aspect of an indentation sequence could be managed using a script called a "Method". Another important feature was the ability to fabricate and attach arbitrary tips, allowing different flow geometries to be characterised. In general, the nanoindenter is capable of providing an arbitrary load history during a test and an arbitary

[1]MTS, Oak Ridge, USA

displacement history.

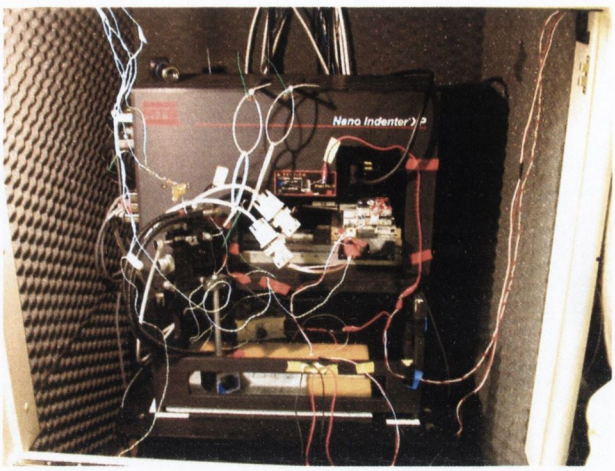

(a) Photograph of Indenter, featuring slight modifications.

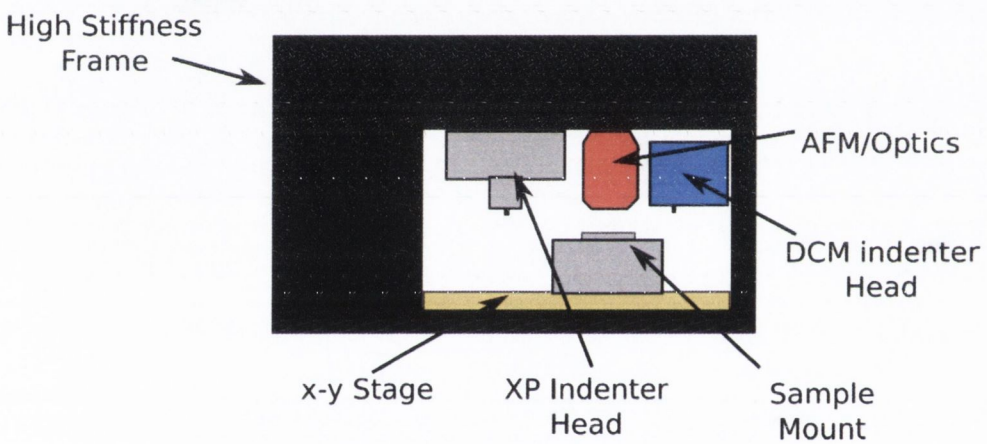

(b) Indenter Block Diagram.

Figure 3.1: Photograph (a) and Block Diagram (b) of the indenter setup.

The nanoindenter setup consists of 2 separate indenters, an AFM with integrated optics and an x-y stage mounted in a high stiffness frame arranged as shown in figure 3.1(b). The two indenters are the XP unit and the DCM (Dynamic Contact Module) unit. Both units are capable of taking dynamic stiffness measurements, (section 2.6.2), as well as the more standard measurements, (section 2.6.1). In order to offer lower noise floors and increase load and displacement resolution, the DCM is a smaller, reduced mass version of the XP, however the underlying design principles are the same. The usage of either the DCM or the XP depended on the nature of the experiment. The XP was the predominant instrument due to it being more robust and possessing

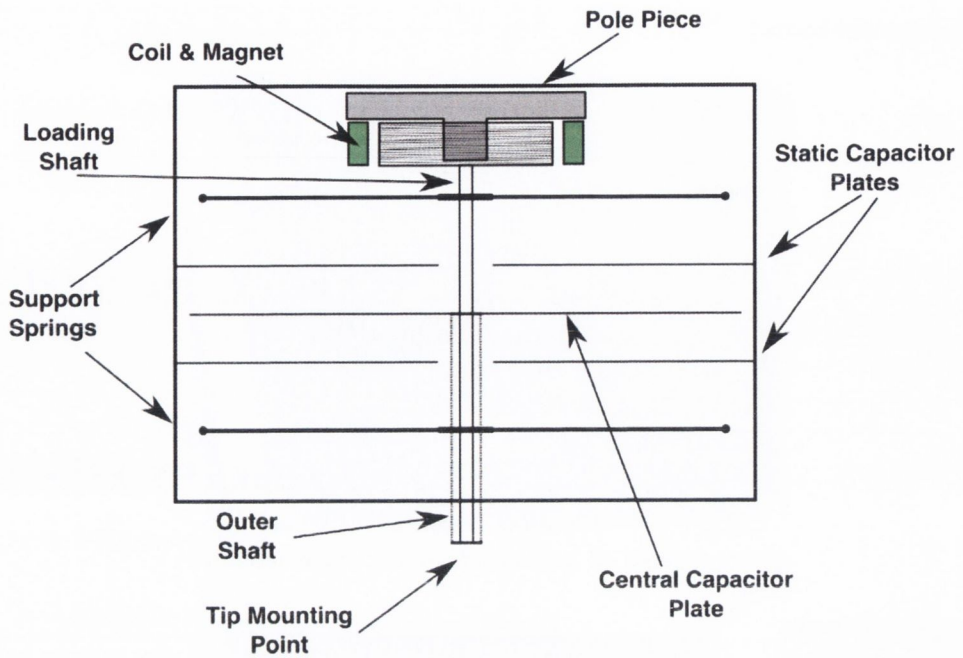

Figure 3.2: Nanoindenter Schematic: The main components of the indenter are shown in this diagram. The coil and magnet, providing the force, connected to the loading shaft upon which the tip is mounted. The support springs which keep the shaft steady laterally. The capacitor plates, linked to the outer shaft for the displacement measurement.

a greater dynamic range and easier tip change method than the DCM.

The nanoindenter is designed to apply a defined force to a sample via a tip of known geometry and measure the resulting displacement as the sample deforms under the resulting stress. From the known force, displacement and tip geometry the sample properties may be derived, more details may be found in section 2.6. The general indenter design consists of a load cell to provide the stress and a displacement measurement method. Figure 3.2 is a simplified cross section of the indenter head, detailing the main components.

The voice coil actuator provides the force required. This type of actuator has been proven to demonstrate quiet operation. It is a moving coil arrangement. This can apply a force of up to 750mN with a resolution of $\approx$ 50nN with the XP and a maximum of 10mN with a resolution of $\approx$ 1nN with the DCM. The force vector $\vec{F}$ is defined by $\vec{F} = \int I(\vec{dl}\,\vec{B})$, where I is the current through the coil, $\vec{B}$ is the magnetic flux

density and $\vec{dl}$ is the length through a straight section of conductor, hence the integration of a number of conductor segments to approximate the curve of the speaker coil. An applied current results in a force which causes a displacement of the indenter shaft. However this relation alone is not satisfactory for measurement purposes and the force must be calibrated against mass standards. The voice coil actuator is capable of very high accelerations and the response of the system to a disturbance is primarily limited by the control loop. If a force of over 750mN is required, then a cantilever is brought into contact with the end of the shaft, capable of raising the maximum force to 10N. The force exerted by the cantilever is modulated by a stepper motor and is measured and controlled via a strain gauge attached to the high load cantilever which measures the applied force.

The indenter shaft is held in place by leaf springs. The springs have a very low stiffness in the displacement direction ($100 - 80\text{Nm}^{-1}$), but a relatively high lateral stiffness($\sim 7000\text{Nm}^{-1}$). The springs are not linear over the entire displacement range, so the stiffness at any particular displacement is given by a look-up table generated by calibration at time of manufacture. Using interferometric methods to measure displacement and calibrated weights to measure force, a load versus displacement curve for the indenter in free space is generated. This curve allows the calibration of the support springs.

The displacement measurement of the shaft is undertaken by a 3 plate capacitor setup. One plate is attached to the mobile shaft and the two other plates are stationary. In order to avoid unwanted measurement of displacements due to strain of the loading shaft, the central plate of the capacitor is attached to a collar surrounding the shaft. This lessens the susceptibility to elastic strains in the shaft resulting from loading which could subsequently contaminate measurements.

An AC voltage is applied to each of the static plates, 180° out of phase and the voltage difference is used to determine the absolute displacement. This method of measurement can result in displacement resolutions of < 0.01nm for the XP unit whilst the DCM can achieve a resoltion of 0.2pm. The indenter is calibrated at time of manufac-

ture.

The indenter head is held within a frame of high stiffness in order to effect operation as little as possible (see 2.6.2). There is a limit to the range of stiffnesses the indenter can measure. The lower limit depends on the displacement sensitivity, so to be measurable, the contact must be stiff enough to produce a deflection in the load/dsplacement slope or cause a dampening of the harmonic oscillation. The upper limit of stiffness measurements is defined by the frame stiffness (8.2MN/m). The frame compliance can be corrected for, but only to a certain extent and as a result, large contact areas (creating large stiffnesses approaching that of the frame) prohibit accurate measurement.

The sensitivity of the indenter displacement measurement means that it was affected by mechanical vibrations from external sources (traffic, air conditioning plant etc.). In order to attenuate these external mechanical vibrations, the indenter was mounted on a vibration isolation table in an enclosure designed to dampen acoustic interference. In practice, using the indenter's own displacement measurement, background vibration was found to be on the order of $\sim 7 - 10$nm which was reduced through use of the anti-vibration table to < 1nm.

3.2 Atomic Force Microscopy

Atomic Force Microscopy (AFM) is a method of mapping out the topography of a surface using a scanning probe in contact with the surface [80]. It was originally designed as a complimentary method to Scanning Tunnelling Microscopy (STM) by being able to work on non-conducting samples. The probe is a sharp tip on the end of a cantilever typically made from silicon or silicon nitride. As the tip scans, the surface forces interact with the tip and the cantilever deflects. Unlike Binning et al. the cantilever deflection is not measured by an STM probe, instead, the magnitude of the deflection is translated into topographical information via reflection of a laser onto a photodiode as detailed in figure 3.3.

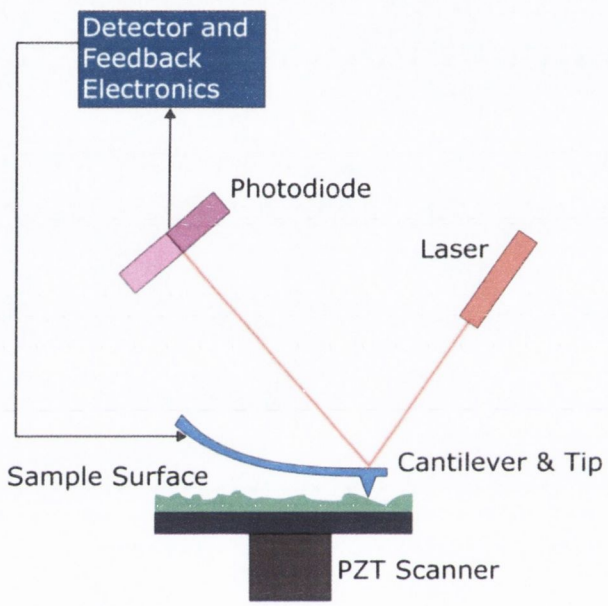

Figure 3.3: AFM Block Diagram detailing the basic components for operation. A laser beam is focused on a cantilever and the reflection made incident on a photodiode. By placing the tip on the end of the cantilever in contact with a surface which is then scanned under the tip using a piezoelectric transducer, the cantilever will deflect depending on it's interactions with the surface. The deflections of the cantilever cause the reflection of the laser beam to move around and these are measured and intermpreted.

By relying on a high displacement sensitivity and a cantilever with a low spring constant, AFM is highly sensitive to changes in surface forces and may be used to detect localised variations in a samples properties. Data from the phase shift (in AC mode) or the lateral movement (in a DC mode) can often reveal features not easily visible in topographical data such as surface energy.

The AFM in use for this project was made by Danish Microengineering (DME)[2]. The scan head was a DualScope^{TM} DS95-200 with a C-21 controller. The scan head bolted into the indenter frame and contained all optics and piezo scanners and so, relied on a static stage. It allowed *in-situ* three-dimensional high resolution scans of samples to be taken of experiments with a very quick turnaround. The lateral resolution is essentially only limited by the shape of the tip and will achieve a resolution of ~ 10nm in all the X&Y axes. The Z axis resolution was typically 0.31nm, limited by the design of the AFM controller.

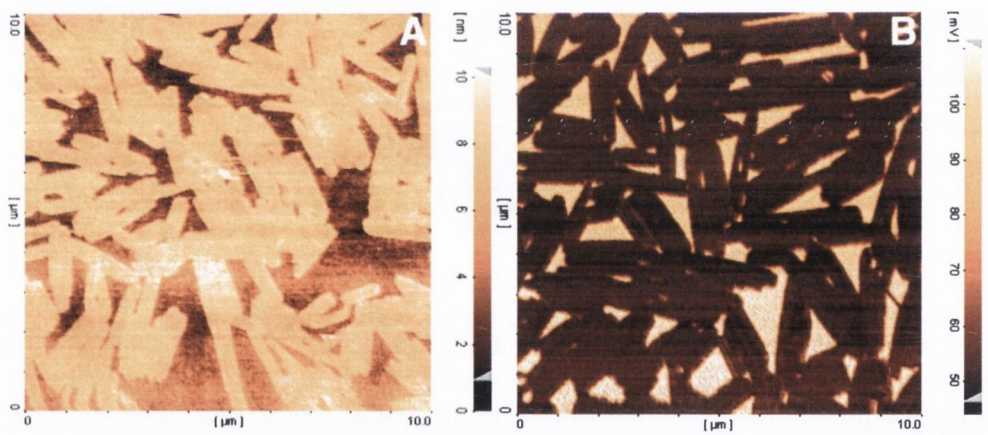

Figure 3.4: Artifacts revealed in a spun thin film of polystyrene. "A" shows a height trace of polystyrene of M_W352k and "B" shows a lateral torsion image of polystyrene M_W 58k.

The AFM in this project was a modular part of the indenter frame, allowing *in-situ*, non-destructive imaging of indentations within minutes of their formation. This was important, especially when creep or relaxation processes were active and the geometry of the indent would change over time.

[2]Danish MicroEngineering, Herlev, Denmark

Whilst the AFM is a very suitable tool in many circumstances, there are certain limitations which must be considered. Tip radius limits the minimum resolution, as described above. This can be overcome by modifying the tip, using such methods as FIB milling to remove material or by extending the tip by adding material. The attachment of carbon nanotubes to AFM tips is now a commonplace practice to try and reduce tip radius and produce a known tip shape and radius, this is discussed in more detail in section 4.6.

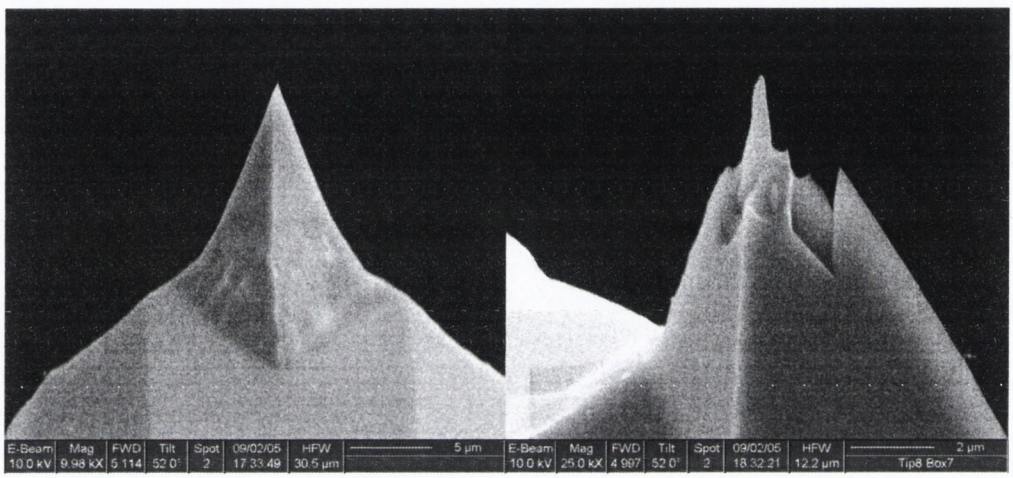

Figure 3.5: Original AFM Tip (left) and FIB sharpened AFM tip (right).

Another problem with AFM is the measurement of high aspect ratio features on a surface. These features will not be measured correctly due to convolution as a result of the sides of the probe coming into contact with the sample as opposed to the tip alone. Much thought has been applied to the performance and problems of AFM tips [81] [82].

However, nanotubes do not normally solve the problem of imaging high aspect ratio structures due to their short length. Longer nanotubes demonstrate flexibility, introducing other problems. Using multi-wall carbon nanotubes to increase tube stiffness and allow for tube lengths up to several microns have been investigated [83]. However tip radii must increase to maintain stiffness. 60nm diameter is required for a 5µm long nanotube [84]. In order to prevent the issue of contact with sidewalls, a tip extension must be of a greater length than the largest vertical feature and as narrow as

possible. It is possible to lengthen an AFM tip by up to 500nm without significantly widening it by growing a metallic appendage on the end [85]. Another technique is sharpening tips using the FIB to sputter away material, (see figure 3.5), but such tips are delicate and proved difficult to use. Unfortunately, as the length of an extension to the tip grows, it brings a greater propensity to flex and introduce errors. Such tips are often delicate and care must be taken when scannig high aspect ratio features as high speed. For these reasons Scanning Electron Microscopy combined with Focused Ion Beam cross-sectioning were used as a complimentary method of imaging along with AFM.

3.3 Focused Ion Beam Milling and Electronic Microscopy

The project utilised a Strata DB235 instrument, a combination of Field Emission Scanning Electron Microscope (FESEM) and Focused Ion Beam (FIB) made by FEI[3]. It is a highly flexible instrument allowing integration of energy dispersive X-ray analysis and automated lithography options.

Scanning Electron Microscopy (SEM) is a very well known technique capable of resolving nanometre level features [86]. The SEM produces a focused beam of electrons from a field emission gun. The electrons are accelerated to between $5 - 30$kV. The beam is rastered across the surface of the sample. The interaction of the beam with the sample produces secondary electrons which are then detected by one of several detectors. The position of the beam correlated with the amount of secondary electrons produced can then be assembled into an image.

The FIB works in a similar manner to the SEM except it uses a beam of gallium ions as opposed to electrons. The gallium source is a small quantity of gallium on a metal tip. The gallium is fluidic and held in a cone shape by the extraction field. The gallium ion beam is focused, accelerated (normally through a potential of 5kV) and rastered in a

[3]FEI, Eindhoven, The Netherlands.

similar manner to the electron beam. Although the ion beam can be used for imaging and may also produce desirable results, the beam tends to sputter away material and is rarely used for imaging. This is not such a setback, it is in fact the most desirable property of the FIB. When the beam is focused, precisely controlled areas can be milled away by blanking the beam at appropriate points during the raster. This allows high precision fabrication of features with the smallest feature size approaching 10nm. The deliberate introduction of precursor gasses into the chamber can produce other effects when subjected to the ion beam, such as deposition of insulating or conducting materials via the GIS (Gas Injection System). The GIS offers enhanced milling with reactive gases to produce enhanced etching rates. For this project, the most common use of the GIS was for the deposition of platinum on the surface of the sample. The platinum precursor was an organo-metallic gas introduced to the chamber.

The combination of SEM and FIB as a single tool is a particularly powerful one. The main uses for the dual beam setup in this project were creation of imprinting stamps and cross sectioning of samples which could not be imaged in the AFM. Precise metrology of samples is difficult, which is why SEM imaging data was taken as complimentary to AFM data.

3.3.1 SEM Techniques

The nature of SEM means that it is beneficial to image a conducting sample. Non-conducting samples such as the polymer films used in this project tend to build up charge locally on the sample and affect the beam. For this reason, samples were usually sputtered with a layer of gold $\sim 5\text{nm}$ (as described in section 3.4.3) and connected to ground. The sample was mounted in the SEM vacuum chamber which was pumped to a pressure of at least 1×10^{-5}mbar before the beams were turned on. The beam was roughly focussed on the sample, and the height of the sample was adjusted to attain the optimal working distance from the electron column. The beam would then be optimised regarding focus and stigmation and the area of interest then examined.

3.3.2 FIB Techniques

The ability of the FIB instrument to deposit and sputter away material was the main purpose of the instrument, and was so used to cross section samples and machine stamps. Cross sectioning was used to examine samples with aspect ratios that could not be examined with the AFM. This involved cutting a trench into the sample at an angle which allowed easy viewing of the cross section with the e-beam. Because of the destructive nature of both beams delicate samples had to be protected. The thin gold coat (see section 3.4.3) for electon-beam imaging is not sufficient for work with the ion-beam and cross sectioning involved depositing a protective layer of platinum on top of the sample to be sectioned.

To use the GIS, the organo-metallic material in the GIS cartridge must be heated, then the needle must be introduced close to the sample. Care must be taken regarding the tilt and position of the sample to prevent contact of the sample with the needle. Once the GIS needle was in place, the optics were adjusted to compensate for the effects of the needle on the field of the objective lens. The platinum precursor gas was then introduced. Interaction of the focused beam and the gas would cause the gas to separate into an organic vapor and platinum, resulting in the deposition of platinum about the focal point of the beam, (usually on the surface). For this process, the e-beam would typically be used. The acceleration voltage was set to 5kV, and the beam focused on the surface. The area to be coated in platinum was selected and the raster would begin.

The ion beam was then used to selectively remove material as detailed in figure 3.6. Firstly, the sample was tilted to 52° to make the sample normal to the ion beam, this prevented distortion due to the sample being out of the focal plane of the ion beam. The cross section cut involved two special milling patterns to create the cross section. A rough cut would then be initiated. The rough cut was a raster pattern which would vary the dwelling time of the ion-beam to produce an angled cut at high speed to allow the electron beam access to the section face. The next step would be the "polishing" cut. This was simply a small cut at a low current to expose the area of interest, as the

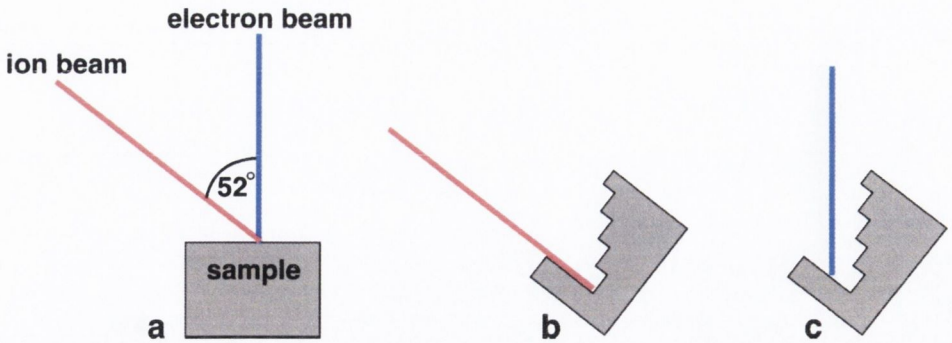

Figure 3.6: Diagram of method used to perform a cross-section cut using the FIB/SEM. The positions of the electron beam and the ion beam are shown (a). With the sample tilted normal to the ion beam, milling can occur (b). The cross section can then be examined using the electron beam (c).

first rough cut used a high beam current and had a tendency to produce artifacts. Part B of figure 4.3 shows an example of one of these cuts.

Stamp preparation followed a similar process to the cross section cut, but did not require the deposition of platinum due to the ability of the doped silicon to conduct charge away from the milling area. Usually a stamp would be cut in 3 or 4 steps. Large areas of silicon had to be cleared to prevent collision with the substrate. Precision was not critical on the large area cuts, so high current beams with wide profiles were used to save time. As the accuracy of the cuts required increased with decreasing feature size, the beam current was decreased to present a smaller beam profile. Again samples were coated in a thin layer of gold by sputtering.

3.4 Materials

3.4.1 Stamps

Besides the standard indentation testing tips used (cube corner & Berkovich, see section 2.6.1), customised stamps were produced in-house to facilitate the investigations of thin-film behaviour, particularly in squeeze flow geometries. These stamps were produced from single crystal p-doped silicon spheres of a diameter of 1mm. The

spheres had a lithographic grade polish with the size of surface surface features ranging from $< 1 - 3$nm.

The spheres were mounted on an indenter tip holder and the FIB was used to sputter away the silicon in a controlled manner to produce the required geometry. More details on the method of stamp construction is given in section 4.1

The use of iridium spheres was investigated due to iridium being less brittle than silicon. Unfortunately, iridium blanks were in short supply, meaning that silicon was most commonly used. Nanoindentation was performed to try and determine the crystaline direction of the spheres however the results were inconclusive. The milling process was generally the same as that for silicon.

Tables 3.1 and 3.2 list the names and sizes of the stamps used in this project. As mentioned above, all the stamps are silicon excepting the eponymous "Iridium" stamp.

Name	**Diameter** (nm)	**Contact Area** (m^2)
Arwyn	7400	4.30E-11
Gandalf	9500	7.09E-11
Gandalf White	3440	9.29E-12
B1	827	5.37E-13
B2	3450	9.35E-12
B3	2000	3.14E-12
B4	3710	1.08E-11
B8	3000	7.07E-12
C3	7500	4.42E-11
H11	800	5.03E-13
H11 v2	300	7.07E-14
H12	1600	2.01E-12

Table 3.1: List of circular flat punch stamps used in this thesis.

Name	**Width** (μm)	**Length** (μm)	**Contact Area** (m^2)
Iridium	1.00	10.00	1.00E-11
X8	0.61	6.19	3.00E-12
X6	0.51	6.05	3.30E-12

Table 3.2: List of plane strain stamps used in this thesis.

3.4.2 Substrate

The substrate chosen was 0.5mm thick, polished silicon wafer with a native oxide. The wafers were diced into 4cm^2 pieces, scribed on the back side and cleaved, to produce 1cm^2 pieces after spin-coating the polymer onto the silicon.

The main polymers used were;

- Polystyrene (PS)
- Polymethyl Methacrylate (PMMA)
- Polyvinyl Acetate (PVAC)

Spin-coating is a well known and reliable method of creating homogenous films on substrates. The solvent used was primarily toluene and varying film thicknesses were achieved by spinning different concentrations.

Film thicknesses were determined through cross sectioning in the FIB, stiffness measurements with a cube corner and AFM scratch profilometry. All of these methods were found to correlate sufficiently. Section 4.2 explores this in more detail.

3.4.3 Sputter Coating

Some of the samples used required conductive coatings for use in the SEM/FIB (3.3). Sputter coating was chosen for this, due to the thermally sensitive nature of the polymers used in the project. The machine used was a Cressington 208$_{HR}$[4]. The sample was placed in a vacuum chamber and air was evacuated. Argon gas was introduced at a low pressure ($0.2 - 0.005$mbar), from which a plasma was created using a radio frequency generator. The plasma ions bombard the target and knock the target atoms into a gas phase which is deposited on the substrate.

Minimal thermal effects were achieved using a very low pressure of $\sim$ 0.01mbar of argon and a relatively low sputter current of 20mA. The coating was carried out with

[4]Cressington Scientific Instruments Ltd., Watford, England

the shutter in front of the target and the target as far away from the sample as possible. This setup minimised heating of the sample through radiation, thermal conduction and direct ballistic interactions of ions and electrons with the sample.

A typical coating thickness would be of the order of 5nm at a deposition rate of 1.0nm/min.

3.4.4 Tilt Stage

Certain stamp geometries require the sample to be tilted in order to achieve the desired contact. Traditional pyramidal tips did not require alignment as these were supplied already aligned to the axis of the indenter and any small misalignment would not result in a significant error. The manufacture of stamps with a constant contact area (e.g. flat punch & plane strain) revealed a need for correct alignment. This was particularly important on very thin films, for example, a tilt misalignment of 30nm of a flat punch end to end on a 100nm film was unacceptable. Such a misalignment naturally caused errors in measurements, and could possibly lead to damage of a stamp during experiments involving shearing. Section 4.1 discusses the alignment procedure in greater detail.

The "classic flat punch signal" defined by an elastic loading, followed by plastic yield which appeared as a plateau on the load displacement curve (see figure 5.11) was used as an alignment indicator. If the plastic plateau was not observed within the first few tens of nanometers, then the stamp was not aligned and corrections had to be made.

To achieve tilt adjustment, we used two Physik Instrumente M-042.D01 single axis tilt stages driven by DC motors (a photo of which is shown in figure 3.7). The stages were configured one on top of the other allowing independent x and y tilting. Each stage was capable of $\pm 9°$ movement per axis and could be moved a number of "steps", each step being equivalent to 314nrad. In practice, the stage was capable of movements as small as $\sim$ 40μrad due to backlash and overshoot errors, this was sufficient for all the

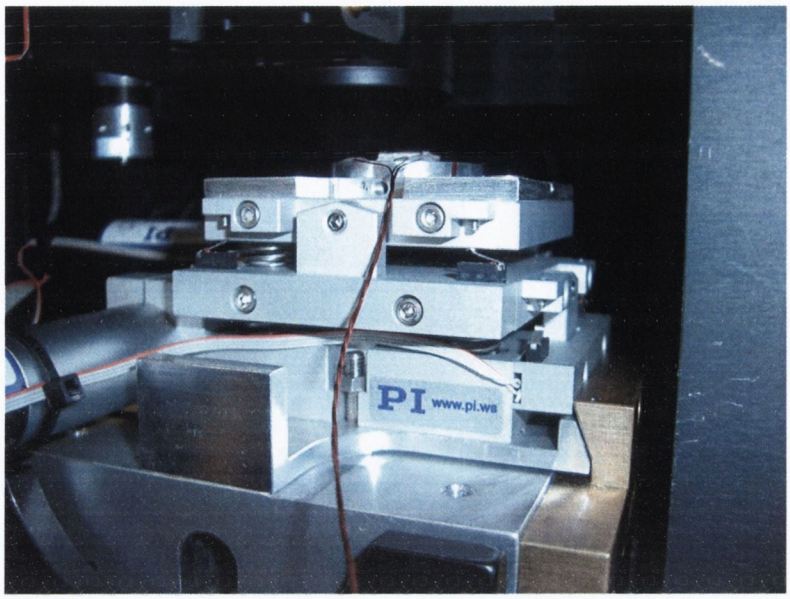

Figure 3.7: Photograph of tilt stage mounted in indenter frame.

experiments.

As the tilt stages were supported by springs, the compliance of these springs under load could subsequently effect measurements. Figure 3.8 shows how measurements can be effected by the tilt stage. The stiffness for the standard stage is shown along with measurements for the tilt stage. The plots denoted by A to E in figure 3.8 are a series of measurements taken up to a radius of ~ 15mm away from the fulcrum of the tilt stage with A being at the fulcrum and E the furthest point. It can be seen that the plots begin to level out towards a constant stiffness, that of the tilt stage. Compliance of the stage under load leads to errors, such as an apparent increase in contact area, resulting in the illusion of an increasingly softening material. Section 2.6.2 provides more detail on the importance of accounting for stiffness during experiments. Figure 3.8(b) is a exploded version of figure 3.8(a) in order to illustrate the divergence of stiffness.

Figure 3.9 shows measurements taken using a calibrated Berkovich tip indented into a fused silica calibration standard at a number of points with increasing distance from the fulcrum. HCS measurements were taken at an applied force of 4N. HCS was used as it provides a good measure of instantaneous properties of the system (see

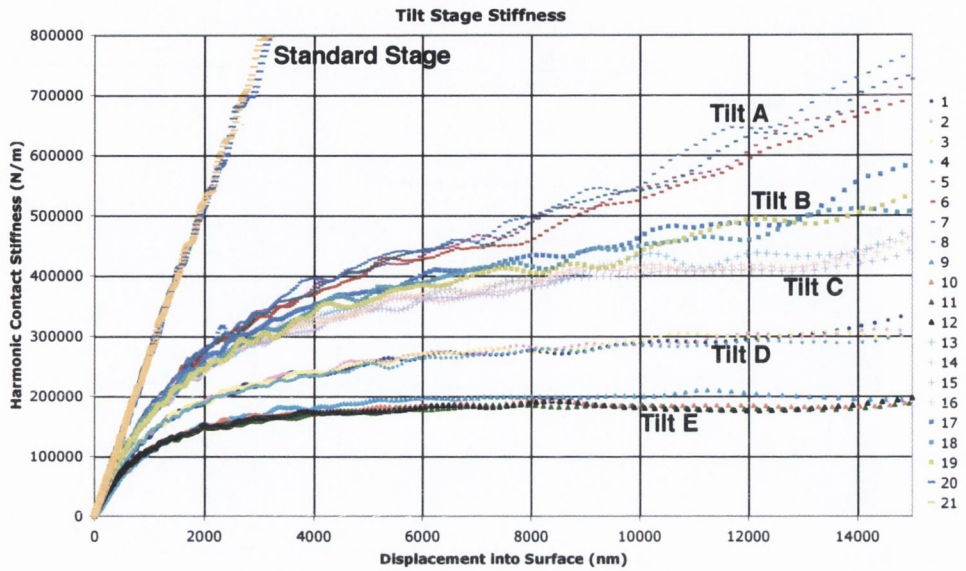

(a) Variation of stage stiffnesses for large loads over various distance from the fulcrum of the tilt stage.

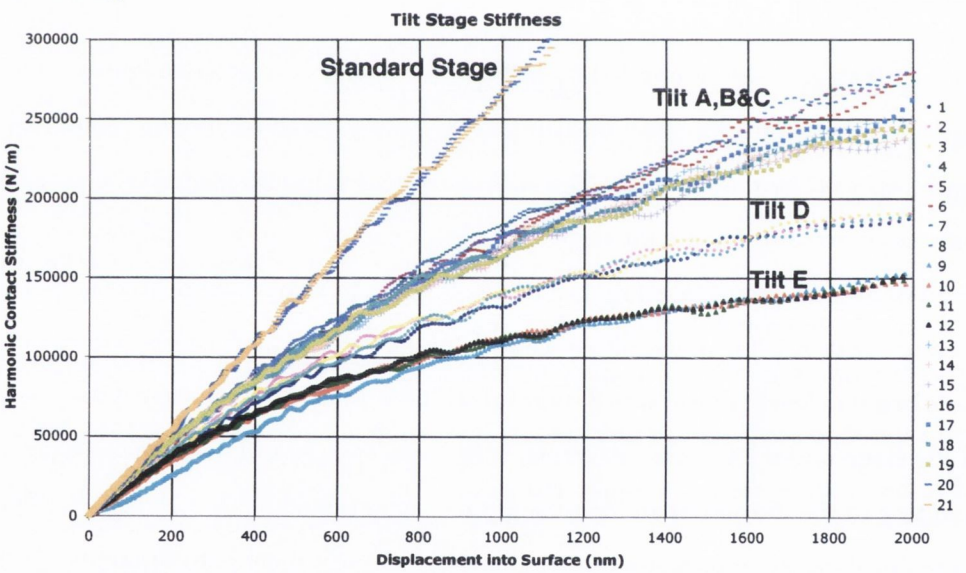

(b) Magnified section of graph (a) above.

Figure 3.8: Dependance of Tilt Stage Stiffness upon stage type and location. (a) Long range behaviour, (b) short range behaviour), A to E in the figures are a series of measurements taken up to a radius of ~ 15mm away from the fulcrum of the tilt stage with A being at the fulcrum and E the furthest point. It can be seen that the plots (excepting A) begin to level out towards a constant stiffness, that of the tilt stage for a particular distance from the fulcrum.

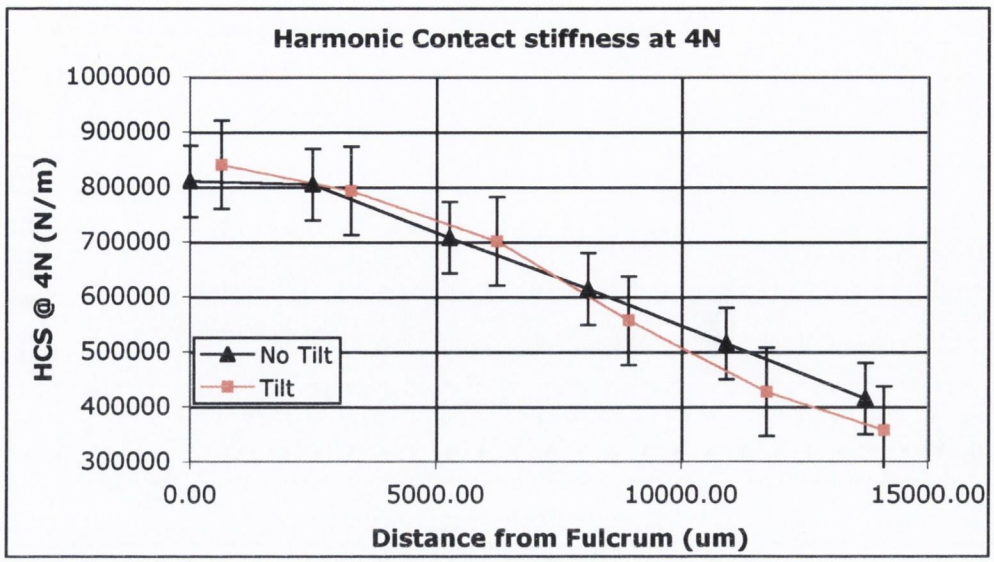

Figure 3.9: Graph of the variation of Harmonic Contact Stiffness relative to the distance from the fulcrum for the tilt stage in a tilted and non-tilted configuration. Taken using a calibrated Berkovich tip indented into a fused silica calibration standard.

2.6.2). Two series of tests were performed, one with the tilt stage level and another with the stage tilted by 47mrad (150000 steps) in both axes. It can be seen that the tilt of the stage did not significantly affect measurements any differently than when non-tilted.

It can be seen from figure 3.9 that the HCS of the stage is approx. 800kN/m falling to 700kN/m at a distance of just over 5mm from the fulcrum. This provides ample area in which to perform experiments without any unwanted effects. This allows the comparison of the stage stiffness to the contact stiffness of the stamps. "Gandalf" was one of the largest silicon flat punches, with a diameter of 9.5μm, this achieved a maximum measured HCS value of 400kN/m. Typical harmonic contact stiffnesses of the stamps used in this project were on the order of 200kN/m or below.

Knowing the stage stiffness allows for corrections to be made to the measurements, although care was taken to perform all tests as close to the fulcrum as possible to minimise errors.

3.5 Oven

It was proposed to investigate the properties of some polymers above and below the glass transition point, section 2.5.1 describes the variation of glassy polymer properties with temperature. Merely heating the sample in order to perform thermal investigations was not always suitable. The unheated stamp would cool the area in contact and introduce errors because of expansion, contraction and the thermal gradient in the material. An oven was designed to provide an isothermal environment.

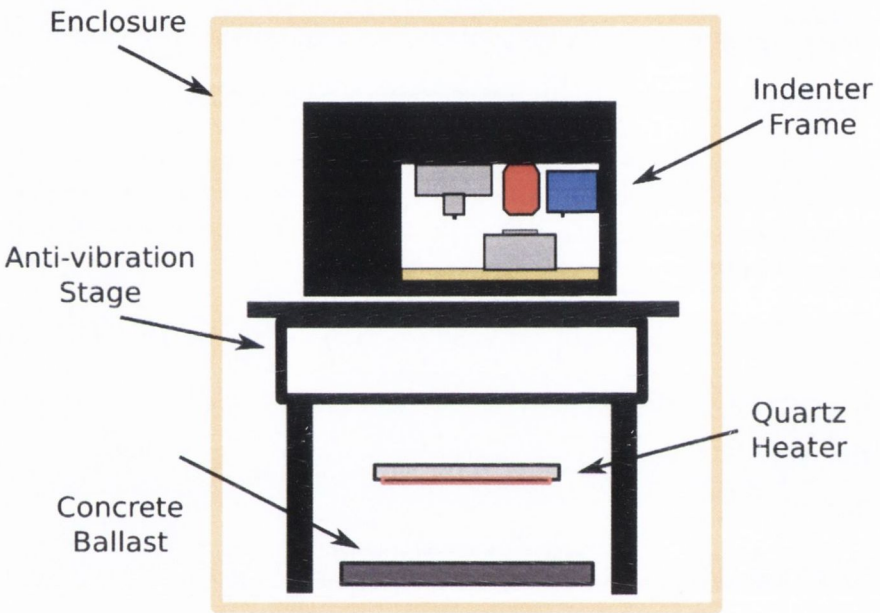

Figure 3.10: Schematic of Indenter oven showing the location of the heater and thermal ballast underneath the frame of the nanoindenter.

The oven design featured 4 x 150W tungsten filament infra-red lamps. These lamps were later replaced with a single 500W quartz element array which improved efficiency and warmup times. The lamps were incident on several concrete slabs which had been painted with matt black radiator paint. A diagram of the setup is shown in figure 3.10. The function of the concrete slabs was to provide a large surface area to heat the air in the enclosure and to act as ballast thus avoiding temperature oscillations. Two fans were placed to provide airflow across the radiator bricks. This speeded up the reaction time and ensured temperature uniformity in the enclosure. A voltage regulation circuit was built to control the power supply to the fans. As the

fans were large, a low rotational speed was possible, reducing acoustic noise in the system. A thermal fuse with a latch was incorporated to cut power permanently to the circuit in case the temperature in the enclosure exceeded 80°C.

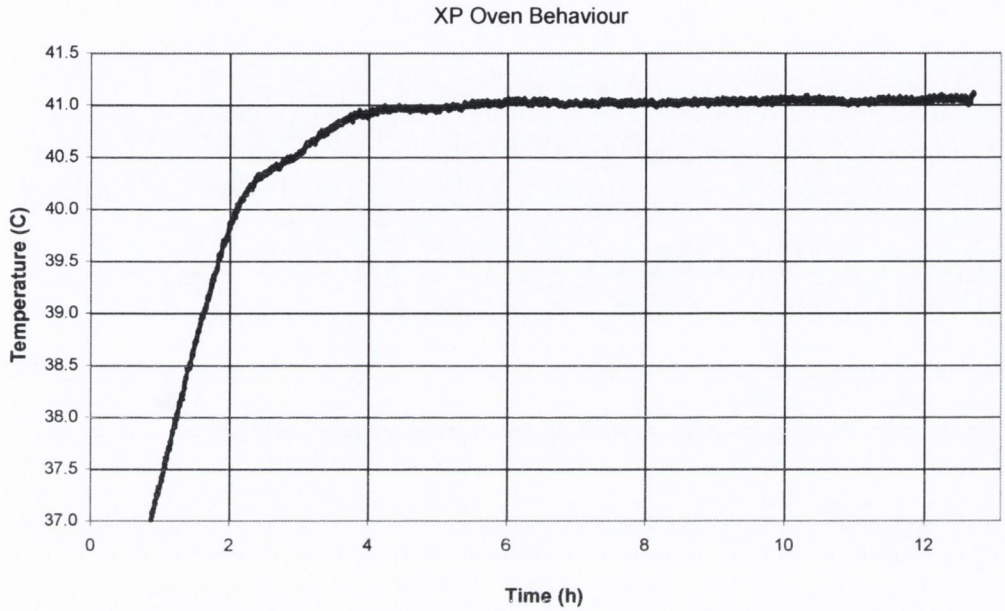

Figure 3.11: Response of oven temperature over time to a fixed setpoint under control of an automated PID controller.

The temperature in the enclosure was controlled by a CAL9000 hardware PID controller which was tuned to maintain a temperature of $30 - 70 \pm 0.1$°C. Figure 3.11 shows the oven behaviour over 12 hours with a setpoint of 41°C The maximum rate of heating was 5°C/h but was determined by the PID controller to be approx. 3.5°C/h to prevent overshooting. Once the setpoint was reached, the system performed satisfactorily to the design specs of ± 0.1°C.

3.6 Shearing System

One of the principle innovations of this thesis was the decision to introduce and investigate lateral loading in contrast to the normal loading provided by the indenter. The rationale was to induce plasticity by supplying shearing forces (section 2.3.2). Piezoelectric transducers were used to supply the lateral force and a vibrometer was

employed to measure the lateral displacements due to the piezo.

3.6.1 Piezoelectric Actuators

The piezoelectric actuators were single crystal shear actuators of 1mm thickness and 1cm each side. Each crystal had a conductive coating top and bottom which was connected to a signal generator via an amplifier. More details on the PZT actuator usage is given in section 4.4.

The capacitance of the PZT crystals was ~ 2nF, this value came in useful when testing for short circuits when constructing the shear devices (section 4.4) as an unexpected value would usually indicate a short circuit.

The application of energy into the PZT crystal produced a heating effect. A study was undertaken to determine if this would effect the samples in any way. A low mass thermocouple was attached to the piezo to measure the temperature and a $\pm$200V sine wave was applied to the piezo at different frequencies. Figure 3.12 shows the effects of this study.

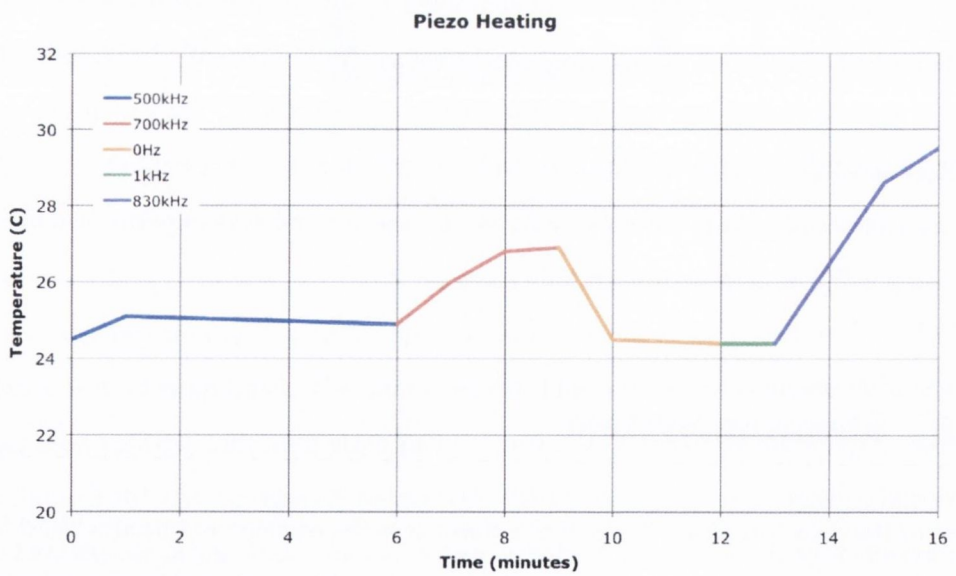

Figure 3.12: Results of temperature measurements when applying an AC voltage of varying frequencies to a PZT element

Initially, an application of 500kHz led to a slight increase above room temperature, increasing the frequency to 700kHz resulted in a rise to 27°C. After this, the amp was turned off and the PZT returned to the ambient. A 1kHz signal produced no measurable temperature difference and the 830kHz signal led to a 5°C change. Considering that most experiments were performed below 1kHz, the heating of the PZT crystal was considered to be of negligible effect.

3.6.2 Amplifier

The amplifier was a Kronn-Hite 7602 wideband amplifier. This provided $17W_{rms}$ of amplification from DC to 500kHz with a variable voltage gain of up to 42dB to a maximum voltage of $\pm 200V$. The input to the amplifier was a signal generator which could be controlled manually or via Labview capable of supplying DC offsets and arbitrary AC functions.

3.6.3 Vibrometer

In order to measure the displacement of the stamp relative to the substrate (see section 6.1), a vibrometer was required. The Polytec DFE-650 is a 2 arm laser doppler vibrometer, a reference arm and a measurement arm. The reference arm was focused on a static object and the measurement arm was focused on the object to be measured. As surfaces were non reflective, retro-reflective tape was adhered to surfaces to improve the signal.

This instrument relies on the apparent shift in wavelength resulting from the Doppler effect. Figure 3.13 shows a schematic of the vibrometer optics. The beam from a He-Ne LASER is split by beam splitter $BS-1$ into a reference beam and a measurement beam. The light from the measurement beam passes through $BS-2$ and is reflected off the surface being measured, M, where it is combined with the reference beam at $BS-3$ before entering the detector. The reference beam passes through a Bragg Cell before being reflected off the reference object before entering the detector. The interference of

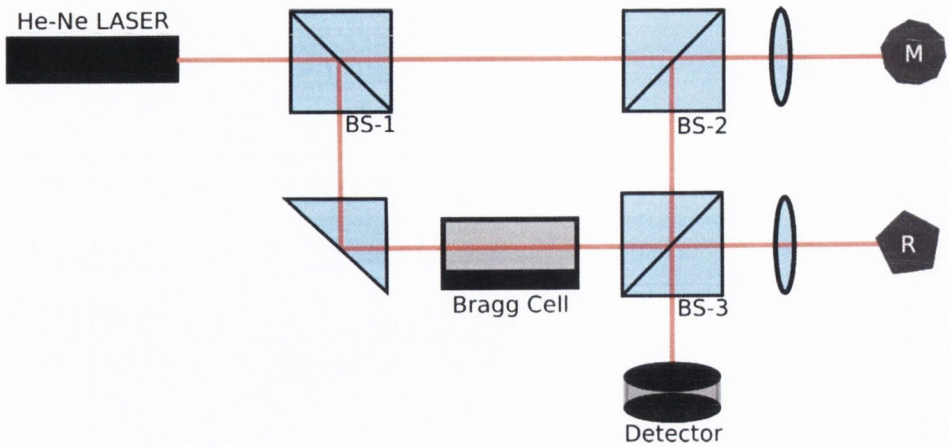

Figure 3.13: Diagram of Vibrometer Optics. A beam from a He-Ne LASER is split by beam splitter $BS-1$ into a reference beam and a measurement beam. The light from the measurement beam passes through $BS-2$ and is reflected off the surface being measured, M, where it is combined with the reference beam at $BS-3$ before entering the detector. The reference beam passes through a Bragg Cell before being reflected off the reference object before entering the detector. The interference of the two beams creates a pattern of fringes, which is measurable by the detector.

the two beams creates a pattern of fringes, which is measurable by the detector. The velocity of the measured object causes a doppler shift in the reflected light and this is proportional to a change in phase which is observed as a fringe movement. A movement from fringe to fringe (or phase rotation of $\pi/2$) corresponds to a displacement of the measured object by $\lambda/2$.

The direction of fringe movement and therefore the direction of the object movement cannot normally be determined with this technique. For this reason, the Bragg Cell is used to modulate the reference beam at 40MHz, creating a virtual velocity in one direction, it is then possible to determine the change in velocity of the object. A Bragg Cell consists of a piezoelectric transducer mechanically coupled to an optical material such as quartz. The transducer vibrates and creates a traveling wave within the quartz which causes a doppler shift as the light is diffracted by the moving wavefront.

The detector provides the velocity information and a quadrature signal is then produced, (consisting of in-phase (I) and quadrature (Q) components). Fringe counting alone yields a maximum resolution of 2nm in this system and so arctangent phase de-

modulation is used to improve this by up to 3 orders of magnitude [87]. A method of arctangent phase demodulation is described by Veldman et al. [88]. This involves manipulating the sampled Q and I signals to produce the phase and amplitude of the displacement. This method requires extensive calculations requiring a powerful microprocessor.

This method can produce an enormous dynamic range for the displacement, essentially limited by the bandwidth of the system. The resolution of the device is stated as being in the picometer range this depended on the quality of the reflected signals and vibration isolation of the setup. In practice, a background noise of $\pm$200pmwas present. Using a sampling rate of 2MHz a maximum velocity measurement of 840mms^{-1} is possible.

The vibrometer was unsuitable for measurement of lower frequency displacements as the highpass software filter had a cutoff centered about ~ 100Hz. Turning off the filter revealed a wandering baseline of magnitude ~ $\pm$500nm due to thermal fluctuations and lateral movements of the vibration isolation stage. This problem may be overcome by application of a suitable offline FIR (Finite Impulse Response) filter.

The actuators of the tilt stage made vibration measurements in-plane impossible and so the vibrometer beams were directed onto the retroreflective tape at an angle of 45° to the piezo displacement direction. To determine the required correction factors, a series of measurements were made from different angles orthogonal and in the direction of the piezo displacement direction. The results of these measurements are shown in figure 4.9 in section 4.4.

3.7 Other Instrumentation

Many of the experiments required external hardware to measure and control experiments which are details as follows;

- Multifunction DAQ/ADC.

- Standalone PID controller.
- Oscilloscope, signal generator, power supply, etc.
- Labview

Key among these items was Labview, which acted as the "glue" holding all the instruments together. Labview is a development environment which uses a visual programming language called "G", produced by National Instruments. Labview facilitates data collection and inter-instrument communication and may also act as a set of virtual instruments. Programs take the form of a block diagram called a Virtual Instrument (VI). Although Labview is extremely flexible, it places an emphasis on instrumentation & control and extremely short development times at the expense of speed and the level of control found in lower level languages. With most minor projects reaching a "beta" stage in under 2 hours, this has proven extremely useful when commissioning new experiments.

Instrument intercommunication was carried out using TTL and GPIB which was chosen for it's robustness, high bandwidth and ease of implementation. The multifunction DAQ/ADC was key in this process, capable of arbitrating signals and voltages. An example of the flexibility of this device was the creation of a voltage sweep which controlled the modulation behaviour of the signal generator (section 6.4). The modulation sweep was triggered by the nanoindenter software producing a TTL signal, which was digitised by the DAQ and signaled Labview to start the sweep.

Chapter 4

Experimental Techniques & Investigations

In this chapter, an overview of the experimental techniques used in the project are discussed which is summarised in [8]. A central part to the project was establishing a reliable system of creating the stamps used to deform polymer films, while the films themselves had to be created and characterised. Also discussed are the methods of performing the indent and the methods of examining the results.

4.1 Stamp Construction

It is vital that the geometry of the stamp is well known as the geometry is key to the measurements made by the indenter and to the shape resultant deformations. Stamps were milled from single crystal silicon spheres using the ion beam, for milling and embossing the spheres had to be firmly affixed to a mount in a manner preventing motion. Stamp construction began with attaching a sphere to a metallic XP tool mount. The mount had a depression into which the ball sat, preventing lateral movement. A thin layer of epoxy was smeared on the mount and the sphere was placed on the mount (figure 4.1).

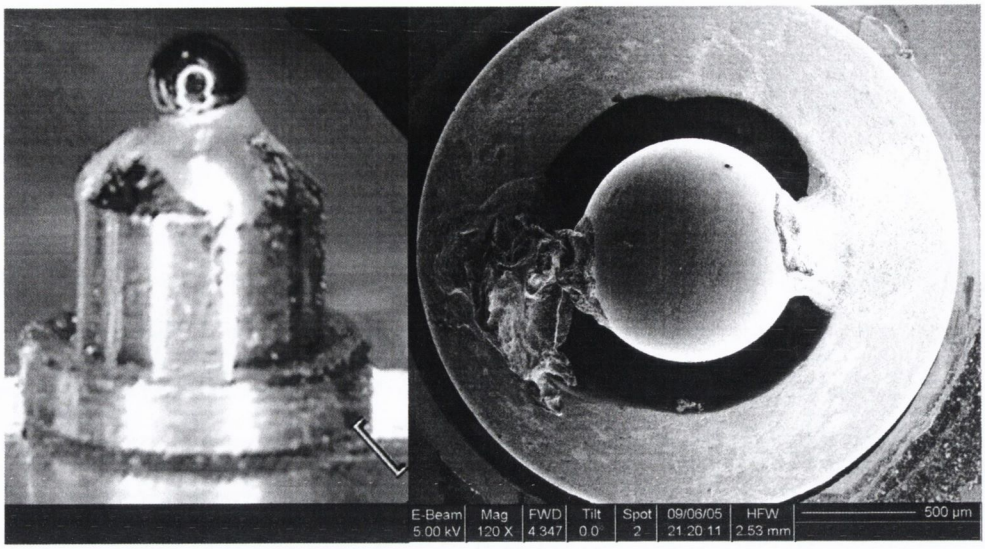

Figure 4.1: Photograph (left) and SEM image (right) of a 1mm silicon sphere on an aluminium mount.

Stamp "Inking"

Once the epoxy had cured and the stamp had passed a visual inspection to ensure the sphere was sitting correctly, the contact point of the sphere had to be determined. This was necessary because manufacturing variations in the mounts would lead to a tilt difference between the mounting for the FIB and the mounting for the embossing and therefore misalignments during embossing. The rationale behind the inking process was to transfer material from the substrate to the sphere at the contact point. The transfered material would be then visible on the stamp in the SEM allowing milling at the contact point.

The sphere was inked using a high load of 1500mN to ensure a large contact area so the transfered material would not interfere with the milling. Inking used a single shear piezo element which was excited at 613kHz. This frequency coincided with a lateral mechanical resonance of the indenter shaft ensuring relatively large amplitude oscillations. If polymer had been successfully transfered to the stamp, a fretting ring would be optically visible on the substrate. The ring of transfered material was then used as a marker for FIB milling, figure 4.2. The relative location of the fretting ring on the substrate was noted as this would prove useful for locating the indents after the

stamp was milled. The transfered material was usually sputtered away as it would be within the radius of the first wide cut and would not interfere with the embossing process. Without the successful transfer of the material, the exact point of contact was subject to a large error and the ball would rendered useless.

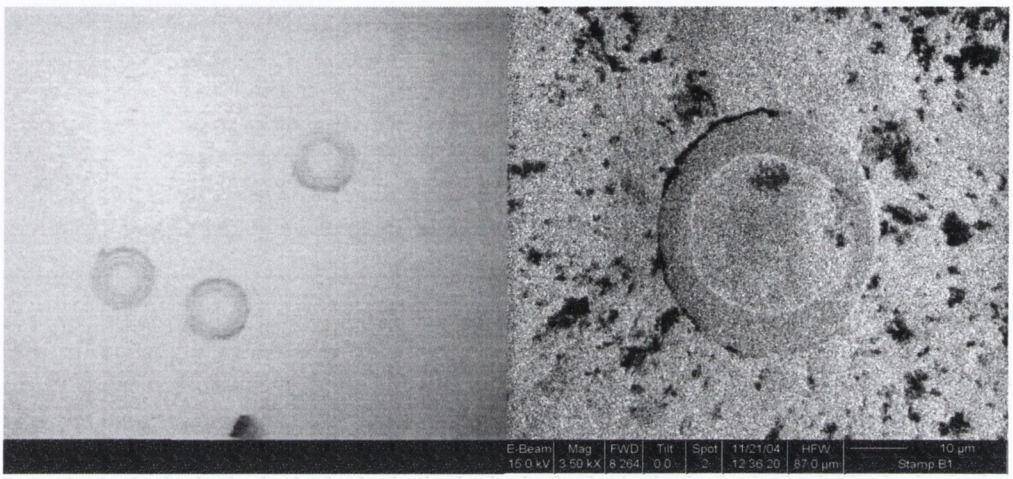

Figure 4.2: Images of fretting rings caused by high load shearing at a resonant frequency of the indenter, (613kHz). Photograph of fretting rings on polymer film (left). SEM image of fretting ring on a silicon sphere (right).

If a sphere was deemed suitable for milling, silver loaded conductive paint was used to ensure electrical continuity between the sphere and the mount to facilitate FIB milling. The mount was placed in a specially designed holder to prevent mechanical drift and the desired pattern would be milled, see section 3.3.

Stamp Tilt Alignment

After the stamp was created in the FIB, it was mounted in the indenter. In order to quantify the tilt errors and perform analysis with the AFM and SEM obtaining the relative locations of the indents was necessary. The stamps were small and the resulting indents not normally visible through the optics of the indenter, so a series of techniques were used to find the indents. A rough estimate of the location had already been obtained through the inking process (section 4.1) and so a tightly spaced series of indents were performed, separated by only a few microns. In most cases the series would be visible, in which case the tilt correction would be performed.

If the indents could not be located several options were available. The image capture system of the indenter was susceptible to thermal noise and had very few facilities for collecting and processing image data and so was of little use for locating some indents. By rerouting the video feed into a separate high specification video capture card and using Labview as a live filter and frame averager, some improvement was achieved. If this was unsuccessful, wide area scans using the AFM were performed. The AFM scans covered a maximum area of $200\mu m^2$ and were low resolution by necessity of time constraints. If the AFM scan failed to reveal the indent locations, then the indent location had to be re-verified. The stamp was indented into a series of hot embossed grating consisting of lines of 400nm pitch. The grating was gold coated and any disturbances in the grating, such as those caused by the stamp, were visible optically. This would then allow the relative position of the indent to be discovered and the final tilt corrections to be executed.

The indents were scanned with the AFM and the profile tools of the AFM software were used to determine the tilt offset of the indent. Typically, 3 iterations of Indent And Scan were required to align the stamp correctly. With this method, tilt errors of less than 5nm on each axis were routinely achieved.

4.2 Polymer Films

The creation of polymer films was a cornerstone in the project. Spin-coating was the method used as it is a reliable method for producing homogenous films of known thickness. The spin coating method used was as follows. A $\%w/w$ (percentage weight/weight) solution of the polymer was created by dissolving a quantity of polymer in a suitable solvent, primarily toluene. To produce 5ml of 2% polystyrene solution the following procedure was used. 5ml of toluene weighs ~ 4.34g, so 2% of 4.34g (0.0868g) of polystyrene was dissolved in the toluene. The quantity of toluene was measured using a volumetric flask and the polymer was measured separately and placed in the flask with the toluene. The flask was then sealed with a stopper and parafilm and

placed in a sonic bath. The sonic bath dissolved the polymer, whereupon the solution was ready for spinning, typically at a speed of 4000rpm for 30s using the polymer concentration as the variable affecting film thickness. Toluene was chosen as the solvent for the the three polymers used as it's solubility parameter was similar to to that of PMMA, PVAc and PS [58] [89] (see table 4.1). Another reason for selecting toluene as the solvent was it's known interaction with silicon. Toluene does not exhibit a strong interaction with the silicon relative to that of the chosen polymers [90]. If this were the case, the toluene would displace the polymer chains away from the substrate resulting in inhomogeneous wetting of the surface.

Solvent	**Solubility Parameter** $\delta(MPa^{0.5})$
Toluene	~ 18.3
Solute	**Solubility Parameter** $\delta(MPa^{0.5})$
PVAc	~ 19.2
PMMA	~ 18.6
PS	~ 20.8

Table 4.1: Solubility parameters for toluene and selected polymers.

The spincoater consisted of a motor attached to a spindle at the end of which was a vacuum chuck. The substrate, in this case a piece of silicon was placed on the vacuum chuck and centred and 3-6 drops of the polymer solution were placed on the silicon with a pipette. The spincoater would rotate the sample at a set angular velocity for a set period of time whilst the vacuum held the silicon in place. The film was removed from the spincoater and heated on a hotplate for about 10min at ~ 100°C to drive off the solvent, before being covered by a petri dish to reduce temperature gradients and heated at up to 20°C above T_g for over an hour. The sample was then allowed to cool slowly to room temperature over the course of 2 to 3 hours before being mounted on a stub for experimentation.

The thickness of the film generally relies on properties such as the molecular weight of the polymer, the concentration of the solution, the spinning velocity and the properties of the solvent [91], this is examined in the following section.

4.2.1 Film Characterisation

Film thickness is a critical measurement for many of the experiments performed. A number of methods are available to characterise the polymer films. Ellipseometry is a common thickness determination method, relying on the change of the polarisation of light upon reflection from a surface with sub-nanometer resolution. Interfereometric methods may also be used, however these cannot achieve the resolution of ellipsometry. Both these methods require that the film being measured is non-absorbing and homogeneous.

Due to the unavailability of ellipsometry and interferometry at the time , other approaches had to be used to determine the thickness of the films. These methods were viewed to complimentary to each other, in order to provide coherent data on film thickness. The methods used are summarised as follows.

- Profilometry of Scratches
- FIB Cross sectioning
- Depth sensing via mechanical testing

The thermal history of a polymer film and the resulting effects on it's mechanical properties are subject to much investigation. The process of spin-coating leaves the thin film of glassy polymer in a non-equilibrium state, effecting the mechanical properties. After spin-coating, the polymer chains are frozen into position under large stresses due to solvent evaporation, surface tension and substrate constraints. Annealing is a common process, often attempted to bring the film into an equilibrium state by providing enough energy through heating to allow the polymer chains to move, before bringing the film back below T_g in a controlled manner, affording the chains time to adjust to the falling temperature. McKenna et al. reviews experiments and theory regarding the behaviour of confined polymer systems (i.e. thin films) and reaches several important conclusions [92]. The physical characteristics of thin polymer films differ from those of the bulk properties. These differences are attributed to the constraints imposed by the substrate and film itself. It has been noted that polystyrene

films (doped or labeled with a fluorescent marker) of thickness below ~ 150nm, exhibit a drop in T_g up to 40°C below that of the bulk value [93]. Further work has shown that the relaxation rate of polymer chains in thin films varies throughout the film and depends on the proximity to interfaces [78] and the roughness of such surfaces [94]. and the results from vitrification [95].

It has been reported that in order to fully equilibrate a film, a temperature of T_g + 50°C was required over a time of 60h. As described above, the annealing attempts for this project were not undertaken to the same degree due to time constraints and the difficulty of safely maintaining a high enough temperature for long periods of time. It should also be noted that quenching of a hot embossed film produced no observable effects of hardness changes [5](section 5.2), however it is also speculated that the hot embossing process cited here could create an annealed sample [12]. All the films in this project were effectively quenched and in an unknown thermal state. Despite such revelations, it should be noted that all films manufactured "in-house" for the project were subjected to similar substrate preparation and thermal treatment and so should be considered in a consistent state for the measurements made.

Profilometry

Profilometry involved making scratches on the surface and obtaining a profile with a profilometer or similar instrument. The AFM was used in this case. Scratches were made in the polymer films with a plastic stylus in order to prevent damage to the underlying silicon. These scratches were then scanned by the AFM and the profiles of these scans were used to determine film thickness. This is demonstrated in part A of figure 4.3. While the AFM appears to have produced reasonable data, calibration in the Z direction was uncertain and difficult to achieve. Another problem was the maximum scan width of the AFM at 200μm. Care had to be taken to make the scratch as narrow as possible. Due to the nature of the AFM profiling software, a reasonable area surrounding both sides of the scratch had to be imaged in order to obtain a practical baseline from which the trench was measured. If the trench was too wide this was

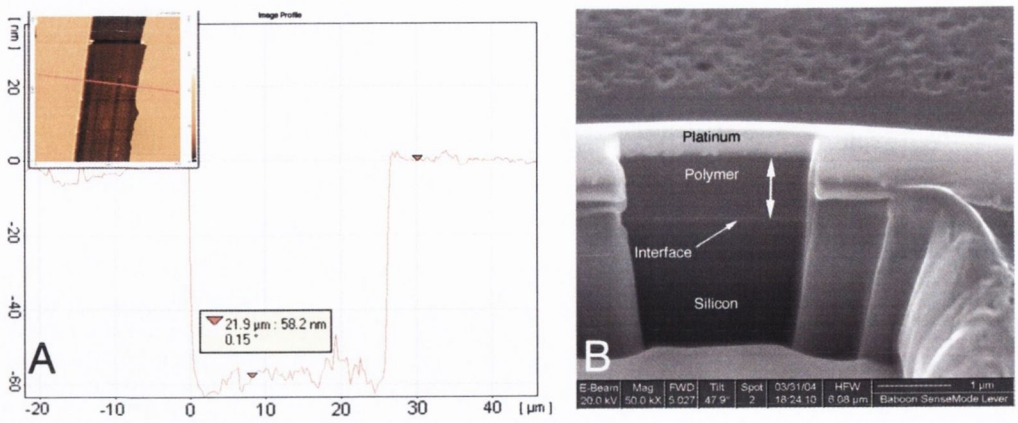

Figure 4.3: Examples of methods used to determine the thickness of polymer films. A : Profile of scratch made by hand in a polystyrene film. Inset, an image of the scratch taken using AFM. B : SEM of FIB cross section of polymer film.

impossible.

FIB & SEM Measurements

Regarding FIB/SEM measurements, high contrast between the non conducting polymer and the conducting gold/platinum layer (deposited to minimise the effects of the beams, see section 3.3) was observed. The polymer-silicon interface was usually visible too meaning it was then possible to determine the thickness of the films. Using this method to obtain values for film thickness was the most time consuming. The process is the same for any cross section preparation, see section 3.3. An example of a cross section is shown in part B of figure 4.3. An interesting point to note is that the stage is tilted 52° to the normal of the e-beam in order to bring the sample normal to the ion-beam to during milling. This means that all dimension measurements made with the e-beam must be divided by cos α to compensate, where α is the angle of tilt of the stage.

Mechanical Testing

A mechanical depth sensing method was used, this had the advantage of being very quick to implement. A cube corner was indented into a polymer film. The data was

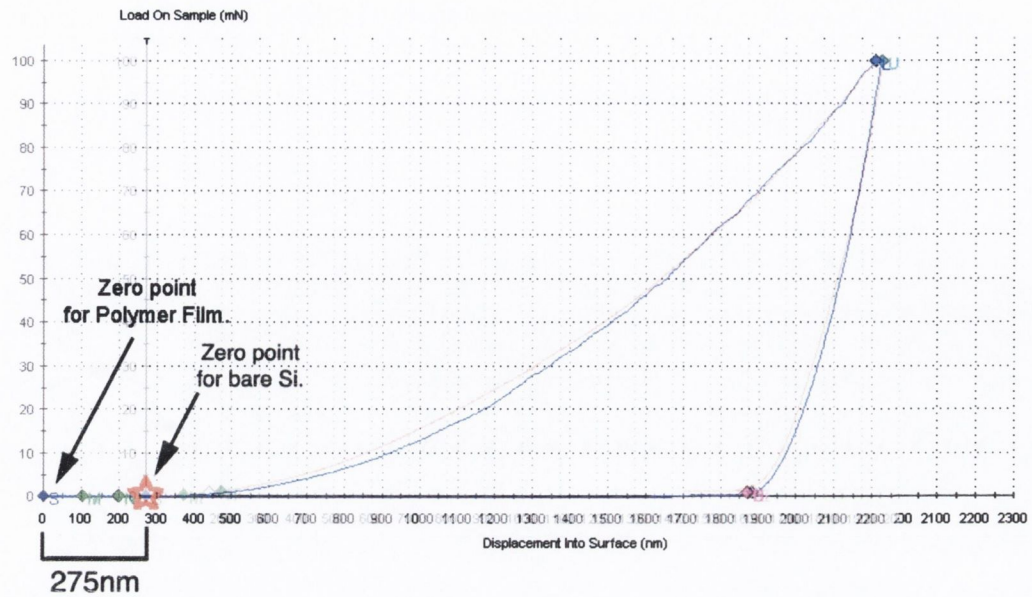

Figure 4.4: Two overlaid nanoindentation plots allowing a comparison of bare silicon and 4% polystyrene film using a cube corner.

verified using the above methods. Figure 4.4 shows the indent curve for a 4%wt. polystyrene film overlaid on the curve for bare silicon.

The indents were designed to be much deeper than the films measured in order for the stiffness of the silicon to dominate the curve in the latter parts. A cube corner tip was chosen over a Berkovich tip because of it's sharper profile, preventing pile-up (indenter tip types are discussed in section 2.6.1). The curves were plotted to the same scale and overlaid onto the bare Si curve. This way, the extra displacement caused by the polymer was measurable by shifting the polymer curve so the hold and unload parts matched. As seen in figure 4.4, there the blue line is the curve to the film and the pink curve is the bare substrate, the depth of the film works out to about 275nm.

Results

All of these methods were complimentary to each other and were used to produce figure 4.5, a graph of concentration versus film thickness for polystyrene of M_W 382, 000. In figure 4.5, the cube corner measurements are represented by the points at 278, 524 and 950nm, the rest of the points were taken using AFM profilometry. The experimen-

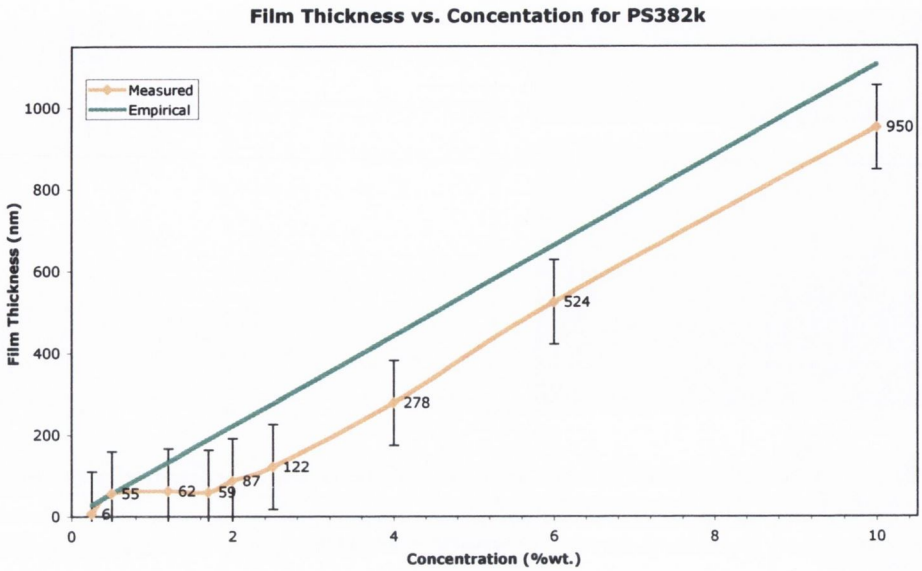

Figure 4.5: Graph showing range of film thickness measurements for Polystyrene 382k using AFM profilometry, and cube corner depth sensing (orange) and semi-empirical model (green).

tal data agrees with the semi-empiral formula for polystyrene in toluene (formula 4.1) [91]. Considering that the film properties are subject to many variables such as polydispersity, solvent evaporation rate (depending on ambient conditions) and substrate condition, the agreement with the actual data is reasonable.

$$t = 93.5\text{nm}\left(\frac{1950\text{rpm}}{\omega}\right)^{0.5}\left(\frac{c_0}{20\text{g/l}}\right)\left(\frac{M}{100\text{kg/mol}}\right) \tag{4.1}$$

Regarding formula 4.1, t is the film thickness, ω is the rotational velocity in rpm, c_0 is the concentration of the polymer solution in g/l and M is the molecular mass of the polymer in kg/mol.

Also of note is that the data is linear until a constant film thickness of $\sim$ 59nm is reached between 1.7%*wt*. and 0.5%*wt*.. Schubert et al [91] identifies 3 regimes regarding the variation of film thickness with solution concentration. Regime I, associated with very low concentration solutions is correlated with no film formation as the polymer chains are washed away during spinning. Regime II is identified by actual film formation, with film thickness proportional to solution concentration. Regime III

is characterised by the film thickness being more strongly affected by higher viscosities than in Regime II, leading to a steeper slope of film thickness against concentration.

It is possible regarding the 0.25% data point where a film thickness of 6nm was measured, that the heavy main polystyrene fraction was washed away during spinning and the leaving behind a low weight fraction which resulted in a film.

4.3 Performing the indent

The nanoindenter was used to apply and measure the force and displacement required for the indents (sections 2.6 & 3.1), the typical method of performing an experiment is outlined here.

The stamp is mounted to the indenter shaft by a small threaded cup. The indentation mechanism is quite delicate and the indenter shaft must be extended and locked in place with 2 pins to prevent lateral movement when changing the tip. Once the tip was secure the pins were removed and the shaft returned to it's parked position. The sample was then mounted on the stage at the correct z position relative to the indenter tip. The XP unit has a maximum z displacement of 2mm, ($\pm$1mm), although best practice is to mount the sample close to the zero position to avoid non-linearities in the measurements due to extension of the spring. Care must be taken to ensure the sample does not strike the indenter during a stage move as it is easily damaged as mentioned above.

A method suitable for the sample was loaded or created, the method comprised of a number of segments in a particular running order, with each segment specifying the operation parameters. An initial approach would be made in order to detect the surface plane and obtain drift measurements. Delicate stamps for example, required a slow approach of < 50nm/s and a highly sensitive surface detection method based on phase rotation caused by damping of the oscillating tip as it nears the surface. Less care was required with more robust stamps and the indenter would approach and

detect the surface at high speed. Once the surface had been detected, the tip would withdraw, make contact with the surface once before obtaining a drift measurement. If the drift rate was satisfactory, then the indenter would withdraw again (to typically ~ 1μm above the detected surface), move the stage to the desired location and approach for the measurement at < 10nm/s.

Once in contact with the surface, a controlled loading segment begin at a defined load or displacement rate to a prescribed depth of load limit. The peak load or position would then be held for some time to allow creep to extinguish and to perform shearing, heating etc. This is followed by a controlled unloading to ~ 10% of the peak value, where a drift measurement was taken and the unloading continued until the tip was clear of the sample.

4.4 Shear Application

The extent of plastic flow in glassy polymers via imprinting processes has been shown to be limited, (sections 5.2.1 & 5.3.2) [6] [7]. Having investigated the limits of normal loading, it was proposed to investigate the effects of shearing strains, the results of which are described in section 6.1. Described here is the method of inducing shear strains within the indenter setup.

A typical shear sample setup is shown in Figs. 4.6 & 4.7 with a stack of 2 piezo transducers. The piezo transducer elements (see section 3.6.1) translate an applied electric field into a displacement. In this case the transducers were orthogonal to each other, allowing independent movement in each of the X & Y axes. The sample was fixed on top of the transducer stack and the measurment was made directly from the edge of the sample, the reference vibrometer measurement was made from a static point close to the sample. The vibrometer relies on a good reflected signal from the surfaces to be measured, however this was not possible due to the materials used and so retroreflective tape was used. Retroreflective tape was attached to the sample to facilitate displacement measurement in either axis. The retroreflective tape was self-adhesive,

with the non-adhesive side uniformly coated with transparent polymer spheres with a high refractive index and diameter $100 - 200\mu m$. The back of each sphere, (the part of each sphere embedded in the opaque material of the tape) acts like a concave mirror reflecting the incident beam back in it's original direction.

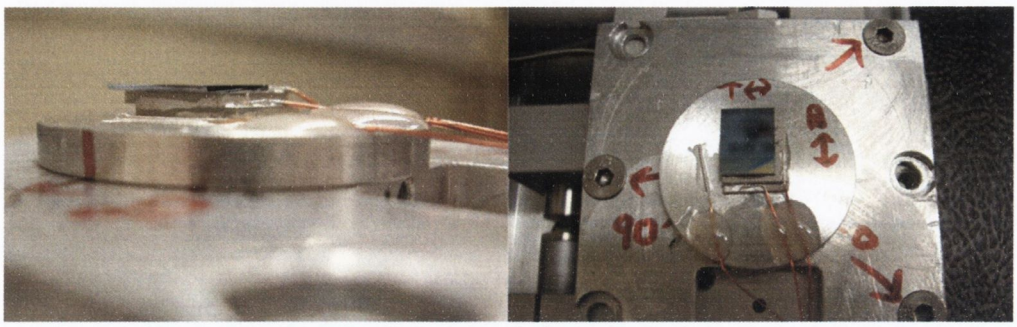

Figure 4.6: Photographs of the double piezo stack mounted on the tilt stage.

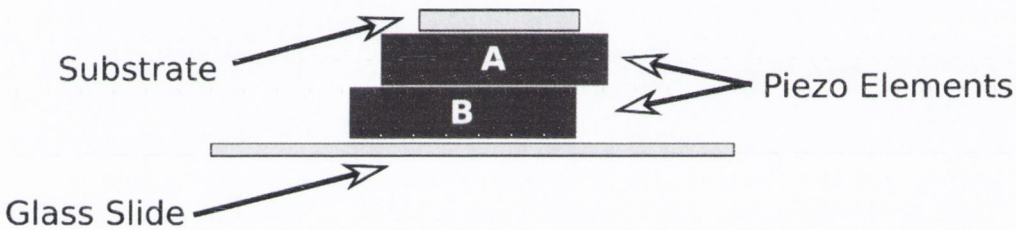

Figure 4.7: Schematic of piezo setup, showing the 2 piezo elements A & B on an insulating glass slide.

A signal generator was used to provide a modulating voltage which was subsequently amplified , typically with a gain of 100, (see section 3.6.2). The shear piezos used presented a displacement of 0.5nm/V, producing a maximum displacement of $200nm_{pp}$ when the maximum voltage of $400V_{pp}$ was applied.

It was found that having the uppermost surface of the top transducer (A in figure 4.7) at a high voltage with respect to the stamp would lead to current flow between the stamp and the sample, destroying the stamp when it came into contact with the silicon substrate. For this reason, the uppermost surface of transducer A was always kept connected to ground with the driving voltages being applied to the other electrodes. The piezo stack was tested by applying 500V to the terminals with an insulation tester, this determined that there was no arcing, current leakage or any other deleterious effects arising from the voltages applied.

The dependence of the incident angles of the vibrometer beams to the sample to be measured was examined. A schematic of the angles used is shown in figure 4.8 and the vibrometer measurements are shown in figure 4.9. Referring to figure 4.8, the black arrow shows the direction of the piezo motion where the mobile piezo is the dark gray box and the static substrate is light grey. The red lines indicate the LASER beams from the vibrometer.

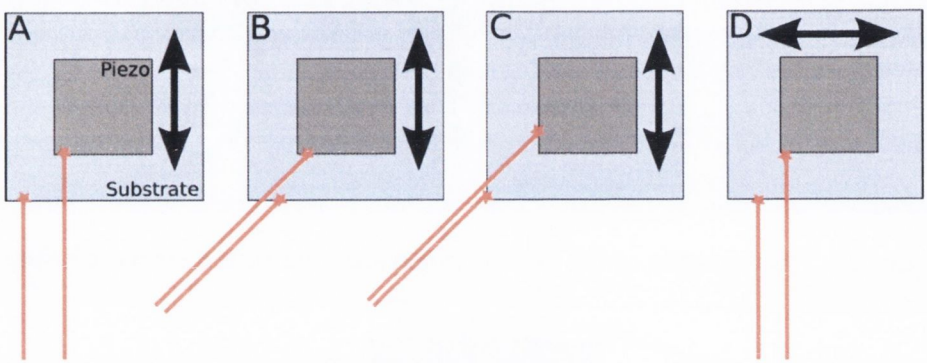

Figure 4.8: Measurement of angular dependance of vibrometer measurement of piezo displacement. A: Beams are parallel to piezo motion, incident on the front of the piezo & substrate. B: Beams are at 45° to piezo motion, incident on the front of the piezo & substrate. C: Beams are at 45° to piezo motion, incident on the side of the piezo & substrate. D: Beams are orthogonal to piezo motion, incident on the front of the piezo & substrate.

figure 4.9 shows the results of the 4 measurement positions shown in figure 4.8, A, B, C and D along with the ideal pzt behaviour. It can be seen that positions A and B provide acceptable results, showing that the angle of incidence of the laser beams do not result in errors greater than 10nm. Plots C and D show that the position of the lasers on the sample with respect to the shear direction can result in significant error as both measurements were made orthogonal to the shear direction.

Figure 4.10 shows an example of a measured shearing event. For this particular experiment, a peak load of 4mN was imposed on an iridium plain strain stamp bringing it to a depth of 439nm in a polystyrene film of 950nm thickness. At the beginning of the test, the stamp was brought into contact with the substrate and ramped to maximum load causing deformation. The maximum load is then held constant until the shearing operations are complete. A wait of 20s is maintained in order to allow creep processes

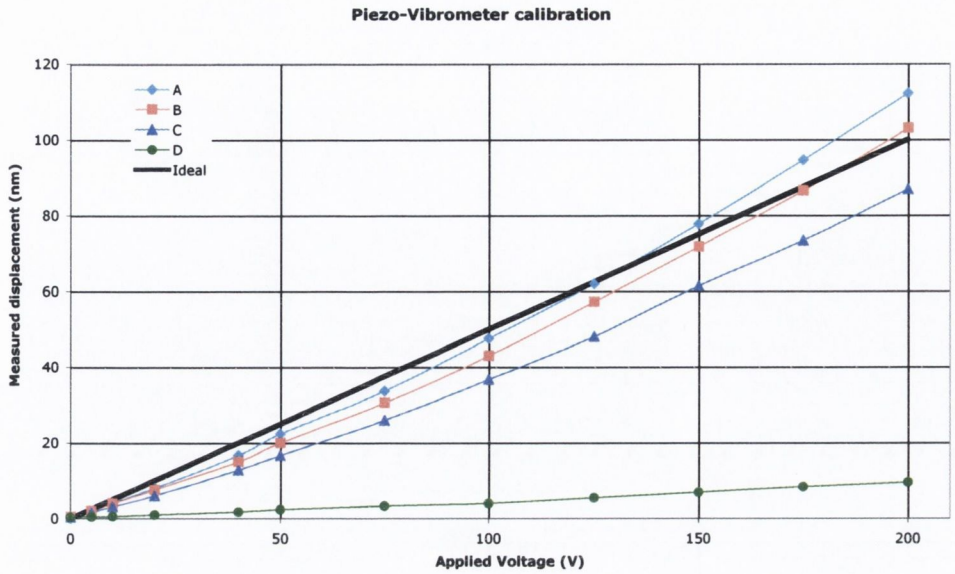

Figure 4.9: Piezo displacement measured by vibrometer for the 4 measurement positions shown in figure 4.8, A, B, C and D along with the ideal pzt behaviour ("Ideal").

to extinguish. Creep manifests itself as continued motion of the stamp into the substrate. The extinguishing of creep is identified by a reduction of the velocity of the stamp. The shearing was applied at 500Hz & $200V_{pp}$ for 50s resulting in a piezo displacement of $100nm_{pp}$. figure 4.10(a) shows the displacement into the sample caused by the shearing action as measured by the nanoindenter. The x axis denotes the "Hold Time" which is the time for which the indenter is maintains a peak load at a steady state. At the 20s point, the signal generator is switched on and the signal amplified and applied to the shear piezo. The vibrometer measures a horizontal motion of the stamp relative to the substrate of ~ $18nm_{pp}$, figure 4.10(b), and a signal from the signal generator before amplification (with a gain of 108) of $1.85V_{pp}$, figure 4.10(c). During the shear tests, the vibrometer measurement was triggered manually or by a TTL signal via the indenter software.

From these measurements, we can immediately conclude that the extra displacement sue to shear in the conditions described above is ~ 110nm. It would appear that the relative motion of ~ $18nm_{pp}$ compared to the piezo motion of $100nm_{pp}$ suggests that some of the strains are being absorbed by the indenter shaft. Further discussion re-

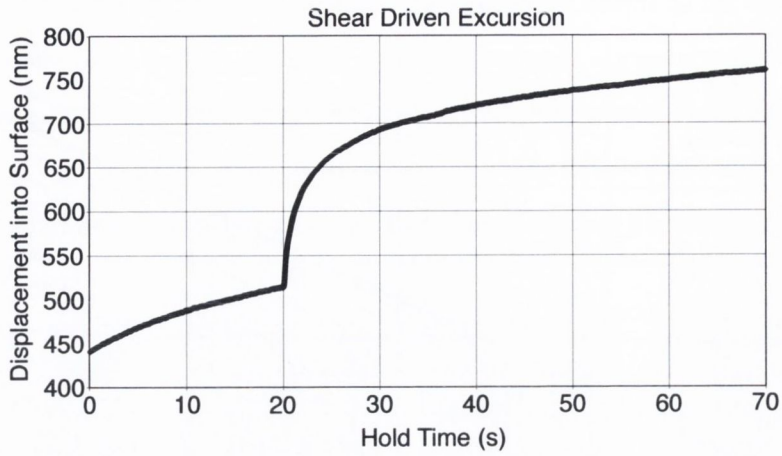

(a) Indenter displacement during plastic event driven by shearing.

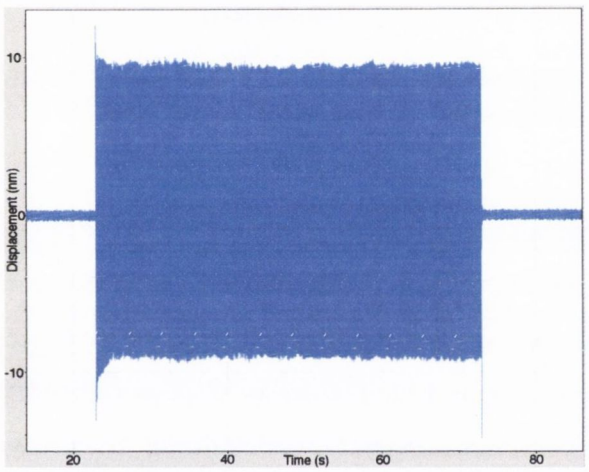

(b) Vibrometer measurement of relative motion between stamp and substrate.

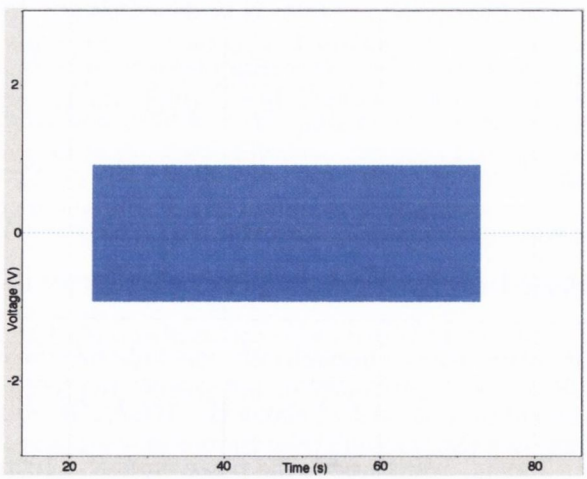

(c) The signal applied to the amplifier by the signal generator, measured by the vibrometer hardware.

Figure 4.10: Examples of metrology for shear driven plasticity.

garding the shearing can be found in section 6.1.

4.5 Sub-surface Stresses & Strains

Some attempts were made to try and picture the nature of sub-surface strains after imprint. The importance of determining the extent and form of the plastic strains becomes clear when considering high resolution structures of up to 8 layers (and beyond) used in modern semiconductor manufacture [96]. If imprint lithography is to be considered as an alternative to more traditional lithography methods, preservation of sub-surface structures is essential in multi-layer processes. The existence of residual strains would also cause problems when dealing with etching and multi-step processes, for example, inhomogenities in density would create problems during etching regarding the etch contrast.

Firstly, a multilayer geometry was proposed. This involved creating a number of polymer layers separated by thin gold films deposited by sputtering (section 3.4.3). The nature of the plastic deformation of the structure would then be visible in the SEM through the use of the gold as a easily visible tracer material after cross sectioning (section 4.6). Secondly, attempts to detect any residual stresses in these films were made using the ability of the AFM to detect changes in surface energy using friction force (lateral torsion) imaging or phase imaging.

Cube corner indents were performed were performed on two kinds of PVAc film, single and dual layer. The single layer was a film of 170nm thickness, an indent was performed until contact was made with the substrate. The 2 layer sample was a film of thickness $\sim 5.3\mu m$ ($2 \times 2.6\mu m$). To create the cross section, the film was coated with gold, grounded and transfered to the FIB/SEM. A sample was prepared in the manner of TEM sample preparation, although TEM was not performed. To prepare such a section, cross sectioning and polishing processes were performed on two sides of the area of interest, see Section 3.3. Cuts were then made along the sides and bottom of the sample to free it from it's surroundings, whereupon a needle attached to a Kleindiek

micro-manipulator was employed to pluck the sample from the trench and transfer it to a silicon substrate. To attach the cross-section to the needle, a charge difference between the sample and the micro-manipulator was required which was usually provided by the e-beam charging up the electrically isolated cross section. Great care was required to transfer the sample in this manner. If successful, the sample was adhered to the surface with platinum from the GIS. The adhesion proved to be inadequate as the samples were often removed from the surface by the AFM during the initial approach, preventing further investigation. The experiment was abandoned after several attempts due to the high failure rate and time consuming nature.

4.5.1 Indentations into multilayered films.

A number of experiments were performed on multilayer PMMA polymer films. A polymer film was constructed as normal and baked for several hours to remove any remaining solvent and annealed, then coated with gold using a sputtering method. A second film was spun on and then heated to drive off the solvent and attempt annealing. The gold acted as a boundary, preventing the solvent from subsequent coatings affecting the underlying layers. The gold layer was typically ~ 40nm thick, which was as thin as possible whilst still acting as a solvent barrier.

Unfortunately, the difficulty of successfully manufacturing multiple layers limited the extent of the investigation. The sputter coater had to be extremely clean, otherwise gold particles detaching from the chamber walls would settle on the substrate during the sputter process and result in the imperfect coverage of gold. These imperfections, known as pinholes would allow solvent from the second coating to leak into the initial film, resulting in deformities. Ambient airborne particles were observed caused pinholes (vias between layers), impossible to avoid as cleanroom facilities weren't available at the time. Solvent leaking through the edges of the substrate was also an occasional problem, although the central portions of the film would generally be unaffected.

Figure 4.11 shows an AFM scan of a cross section prepared by the FIB. A cube corner

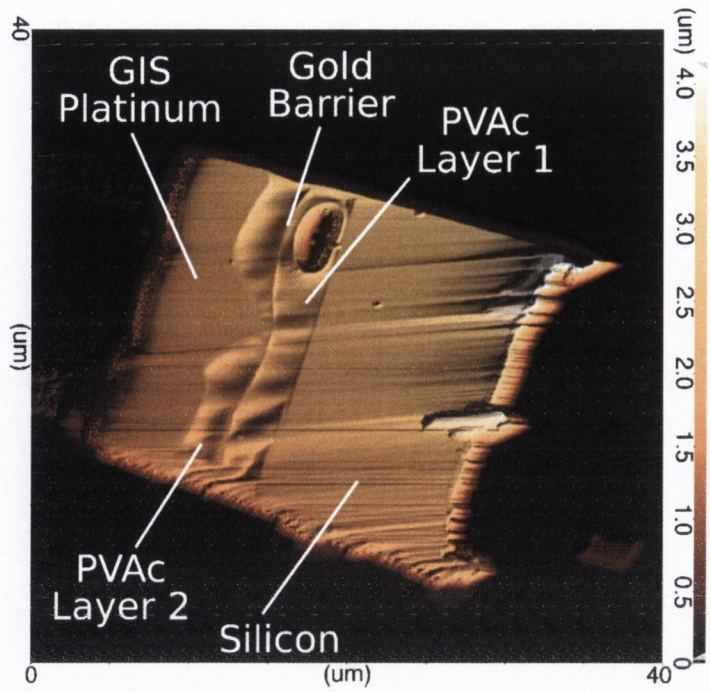

Figure 4.11: AFM image of a FIB prepared cross section of a cube corner indent of multilayer PVAc.

was used to indent to a depth of 2.6μm, the thickness of one layer. The interstitial gold layer can be identified and noted that it's deviation from being parallel indicates an area where material has undergone plastic deformation. This deviation is roughly the extent of the radius of the pileup. We can infer from these results and existing literature that the plastic field caused by the wedge indentation extends beyond the contact radius of the indenter. Models for rigid plastic material in agreement with experiment, show that plasticity exists in an area encompassed by the free surfaces adjacent to the indenter tip extending the part of the tip in contact with the material. These areas, constrained by the surrounding material can only flow into the free area adjacent to the tip, resulting in pile-up [9, 10, 68].

4.5.2 AFM of a thin cross section of a cube corner indent

An attempt to determine if the AFM was capable of detecting surface effects due to the possible presence of residual stresses was performed. The successful use of AFM

for such measurements under certain has been documented [97].

Figures 4.12 and 4.11 show the results of these investigations. While immediately inconclusive using phase mapping in AC mode and torsion mapping in DC mode, a number of possible outcomes may be inferred from this experiment. One conclusion could be that the residual stresses are not present or do not manifest themselves in differences in surface energy. It may also be possible that the AFM was not sensitive enough to detect the differences in surface energy, although an example of it's sensitivity is shown in figure 3.4 where an apparent phase separation of different molecular weights is detected. Another possibility may be that the cross sectioning process in the FIB/SEM could be effecting the sample.

4.6 Post-deformation characterisation

The most common techniques used to characterise the imprinted substrates were Atomic Force Microscopy (AFM) and Scanning Electron MIcroscopy (SEM). Whilst SEM is a mature technique and AFM is a relatively new and radiply developing technique, they are both not without their own unique benefits and problems. As a result they were complimentary to each other in this project.

AFM

For shallow deformations and non critical examinations, the AFM was the most common characterisation tool in due to it's short turnaround time. To perform an AFM scan, the sample stage had simply to be moved from indenter tip to scan-head and the AFM tip engaged, more about the functioning of the AFM is detailed in section 3.2. AFM techniques did not suit samples featuring complex geometries or large aspect ratios. Such samples had to be taken into the FIB for cross-sectioning and examination with the SEM.

Setting aside external influences such as vibration, AFM artifacts can be caused by

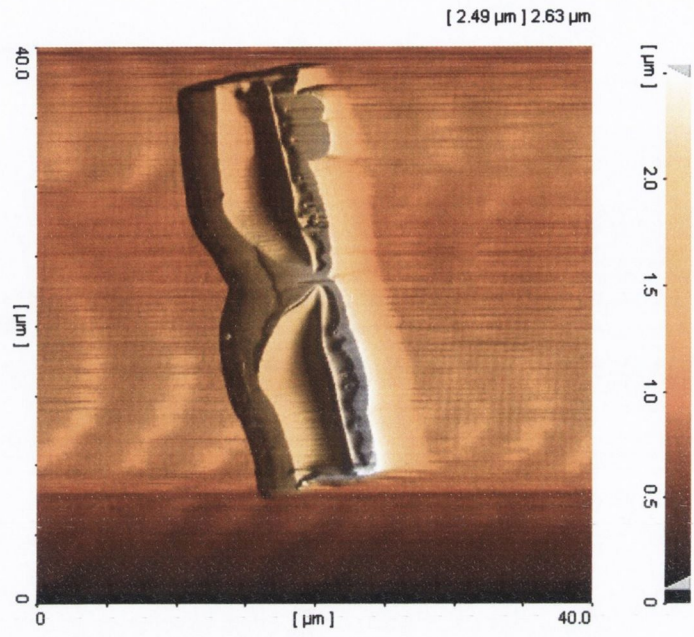

(a) Topographical Trace

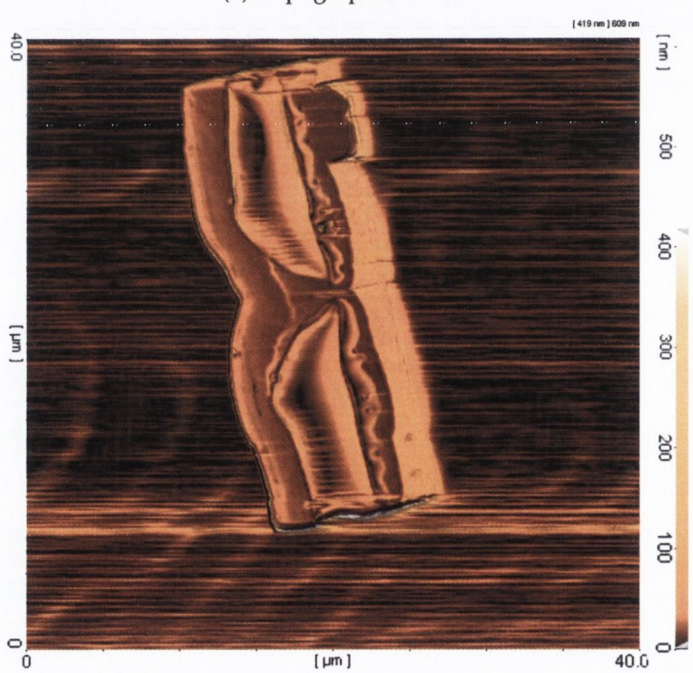

(b) Phase TRACE

Figure 4.12: AFM images of a FIB prepared cross section of a cube corner indent in PVAc.

the imaging tip or the scanner. Scanner artifacts concern the hardware and software controlling and measuring the tip. The AFM consists of several control loops which monitor and vary the voltage of the piezo transducers in order to move the tip in each of the 3 axes. The control loops employ feedback of measured signals to achieve predetermined set-points, this is a simple matter regarding scanning in the x and y directions where a simple steady-state rate is required. The ideal situation during a scan is for the tip to be maintained at a certain distance from, or force on, the surface. This means that the AFM adjusts the z axis to maintain this criterion as the surface changes. For the z axis, more sophisticated control is required as some samples can be complicated topologically. As the "target" is constantly changing for the z axis, this can cause problems. The control loop has a defined frequency response and errors may be introduced if the loop cannot adjust to the new set-point quickly enough. Tuning the control loop incorrectly can lead to either a non-responsive system or uncontrolled cantilever oscillations. Both of these scenarios may be liable to damage the tip or the sample as there is no control over the force exerted onto the surface. A less extreme example of a mistuned loop would be ringing or overshooting when imaging features containing high frequency components, such as sharp edges. Setting the scan parameters correctly will remove many of these problems. Solutions lead from allowing the AFM and controller to warm up prior to operation, to changing the scan speed to bring rapidly varying surface features within the bandwidth of the control loop.

The piezoelectric transducers are susceptible to problems. Temperature sensitivity can lead to drift which distorts images. A phenomenon known as bowing or tilt can occur due to non-linearities in the piezo behaviour. It is common for manufacturers to anticipate these problems and provide fixes with both software and hardware. Again, allowing the system to warm up prior to use is recommended. The AFM used in this project used an integrated interferometer to facilitate z linearisation. Various precision machined silicon (and silicon nitride) gratings are available to check and adjust piezo displacement calibration in the x y & z axes. Processing of the scan data is common, with such tools as filters to remove high (or low) frequency artifacts and the ability to planarise a bowed scan. These techniques may be applied during the scan or after.

One must be careful when using such tools to differentiate between AFM artifacts and actual sample data.

Tip artifacts are ubiquitous, the very fact that a mechanical contact (in standard topographical imaging) is required imposes restrictions on the measurement being made. The tip has a finite radius and this introduces limits to the smallest measurable feature in that objects smaller than the tip radius may be resolved albeit incorrectly. The cone angle of the tip is a limiting factor when imaging high aspect ratio topographies. The cone angle will prevent sidewalls being measured and with narrow troughs may not be probed to their full depth. Deconvolution methods (usually employing numerical post-processing) can be used to correct tip based artifacts, but for this the physical dimensions of the tip must be known. In order to obtain the tip's dimensions, the tip may be "self-imaged". A tip will self-image if it images features smaller than itself, such features are found on specifically prepared porous aluminum. SEM may also be employed to obtain details such as the cantilever dimensions and tip cone angle etc. Modification of the tip is a common practice, appending the tip with grown metallic needles or carbon nanotubes, or removing material using FIB in order to reduce the tip cone angle. Adding a nanotube to the tip makes the tip radius known and can result in sub-moleular resolution [98] [84] . The use of long nanotubes 500nm+ to reduce the effects of cone angle have been attempted, however the question of how the flexure under force and the motion of the nanotube affects the measurements remain.

Electron/Ion Beam Microscopy

As pointed out in the above section, AFM despite it's flexibility and speed of use is not without it's problems. For more accurate feature measurements and geometry observations the Scanning Electron Mircoscope (SEM) was used, (SEM is detailed in section 3.3). The main disadvantage to SEM was that the sample had to be removed from the indenter stage, meaning that a time consuming alignment procedure had to be performed when remounting the sample. Obtaining data for a sample usually meant creating a cross section cut with the Focused Ion Beam (FIB) and using the SEM

to image the cross section (also described in section 3.3). Cross-sectioning involved cutting an angled trench, followed by a cleaning cut with the ion beam. The cleaning cut used the lowest current beam with the lowest profile and would effectively polish the surface for examination. On other occasions, two cross section cuts were used to prepare a thin section which would be plucked out and placed on a grid, typically for use in Transmission Electron Microscopy (TEM). In this case, the thin section was placed on a substrate for mechanical testing (see section 4.5).

4.7 Heating & Cooling

Working on such small scales of displacement, temperature changes were manifested as drift in displacement due to expansion and contraction of the indenter frame and components. The indenter was enclosed in an insulated box, which kept temperature fluctuations to a minimum, and drift rates between indenter tip and sample at room temperature were typically on the order of 0.05nm/s.

One of the first experiments of the project was to use sample side heating to vary the temperature of the sample. It was soon discovered that the thermal expansion and contraction associated with the sample side heating and cooling led to very high drift rates and uncertainty in the vertical sample position. Both of these phenomena crated errors in the data, high drift rates were prone to contaminating the load-displacement data and a wandering sample position could lead to a crashed tip or the indenter software becoming confused. These problems led to the creation of an oven environment to provide isothermal heating (see section 3.5). Because of the large heat capacity and volume of the indenter enclosure and it's contents, the heating rate was relatively slow. Inclusion of a large thermal ballast prevented sudden temperature fluctuations and as a result, drift rates were of a reasonable level.The oven had limitations of temperature range and reaction time, so the thermoelectric devices were used to supplement the oven if needed. These can heat or cool the sample depending on the direction of current flow through the device. The coolers were run in closed loop or open loop control

depending on the setup required. These devices were used to heat the sample in place of the oven when an isothermal environment is not required or possible. In the oven environment, the peltier device could be used to cool the sample to prevent adhesion or slow temperature driven creep.

Temperature measurements were made using a series of low mass K type thermocouples. The thermocouples were small enough that they could be attached to (or close by) a sample without effecting the experiment. The thermocouples were connected to a multi-channel DAQ device and labview was used to monitor and log the temperature.

When using sample side heating, it was noticed that the indenter tip was acting as a heat sink, resulting in localised cooling on the sample. Sample side thermometry and variations in the power dissipation of the peltier devices revealed that the tip only had to be proximal to and not necessarily in contact with the surface to affect it. The tip acting as a heat sink introduces a few problems, unknown temperature gradients are set up through the sample creating unknown conditions regarding the position of the system on the T_g curve and the sudden quenching of the material close to the tip leaves the material in an unknown state (section 4.5). All of this complicates the analysis of the data.

A solution was to construct tip side heating, SMT resistors were attached to a diamond berkovich tip using a thermally conductive epoxy. When an electrical current was passed through the resistors they would dissipate energy, thus heating the tip. By attaching ultra-fine thermocouples to the tip, temperature measurement was possible. The energy flow from the limited thermal reservoir of the tip into the large reservoir of the sample and stage could be estimated, so the energy dissipation into the polymer film could be determined.

Chapter 5

Normal Force Forming

This chapter details the experiments undertaken while investigating the plastic forming of thin film glassy polymers. The amorphous properties of glassy polymers lend themselves to forming operations because of their material properties such as isotropy and low hardness.

In order to try and build a picture of the forming behaviour of these films, initially, the thermal behaviour was investigated. An investigation into the variation of the yield stress on a film of polymer based photoresist was undertaken, as well as mechanical characterisation of hot embossed films using polymers of differing molecular weights were supplied for testing. The goal for examining these samples was to determine if the process at elevated temperatures created inhomogeneities, residual strains or any other differences during the embossing process.

The results of the initial thermal investigations led the main thrust of the project towards room temperature forming of glassy polymers. This led to most subsequent experiments being undertaken below the glass transition, T_g. Above T_g, the probability of adhesion increases, meaning that unwanted strains are created when separating the stamp and substrate. In the worse case scenario, adhesion may cause material to be transfered from the substrate to the stamp, causing defects in the sample and requiring the stamp to be cleaned or discarded. Also, if the material that is to be formed is to

be active (e.g. polymer LED material), forming above T_g reduces the choices available as many active materials degrade upon heating. Strains resulting from cooling and temperature gradients during and after processing must also be considered.

The squeeze flow geometries chosen were deformation of a coupon and cylindrical flat punch. The flat punch was chosen for most experiments as the constant contact area simplified analysis. Using a single flat punch on a series of films of varying thickness, it was verified that a residual layer of material exists underneath the stamp with the ratio of the original film thickness to the residual layer thickness otherwise known as the mask ratio.

5.1 Thermal Experiments

A common process in the field of Imprint lithography is that of elevating temperature to achieve the desired results. Most commercial imprint tools are capable of providing elevated temperatures to facilitate material transport (see section 2.5.2). While this project was mostly concerned with sub-T_g deformation of polymers, investigations into the thermal behaviour of such polymers were carried out.

5.1.1 Temperature Dependance of Yield Stress

A study into the effects of temperature on the yield point of a glassy material was carried out. The resist was a proprietary polymer based material, (MRI 6002.3)[1]. The resist was provided pre-spun onto scored wafers. The resist was designed for especially for nanoimprint technology, and curable by UV exposure or baking with a pre-cure T_g of $\sim$ 40°C [39] . Due to the photosensitive nature of the material, samples were prepared in the absence of light. The thermal curing properties of the material were not investigated. Using the oven as described in section 3.5, the enclosure was heated to the desired temperature.

[1]The MRI 6002.3 resist was manufactured by Micro Resist Technology and kindly provided by Prof. Helmut Schift of the Paul Scherrer Institut.

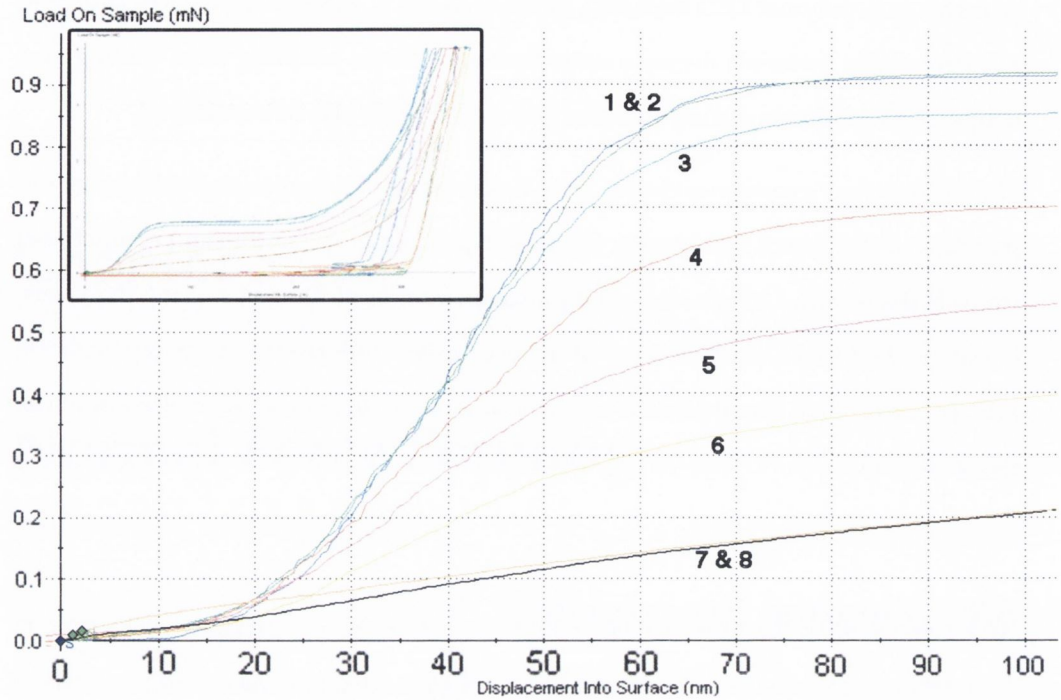

Figure 5.1: Load vs. Displacment curves showing the change in yield behaviour with temperature. Inset shows the entire loading curves to the peak load of 4mN. The gradual drop in the yield point can be seen in curves 1 to 6. For curves 7 and 8, the turnover has disappeared completely suggesting that the system is close to or at T_g

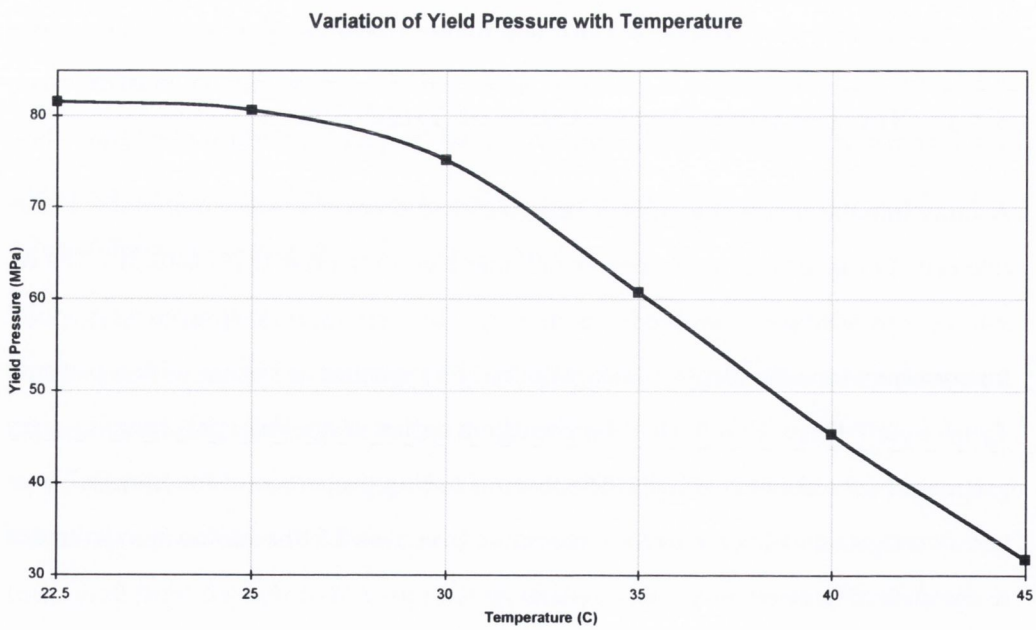

Figure 5.2: Variation of Yield Pressure with Increasing Temperature

A flat punch was used as it provided a clear yield turnover and the experiments were run from 25°C to 60°C. Figure 5.1 shows the curves generated by the indenter as the temperature is increased. The gradual drop in the yield point can be seen in curves 1 to 6. For curves 7 and 8, the turnover has disappeared completely suggesting that the system is close to or at T_g. The yield pressure was found by taking the force at which the plastic turnover occurred for each temperature. Figure 5.2 shows the results of the variation of yield pressure with temperature.

What is clear from the curves is that the force required to reach the yield point is falling as the temperature rises. More thermal energy is added to the system, leading to an increased mobility of chain segments due to an increase in the activation volume. Activation volume describes the size of a polymer chain segment which is available to move to a new position, thus facilitating flow as it increases. The concept of activation volume is discussed further in section 2.5.2.

To attempt to quantify this, the following relation was used.

$$V \propto \frac{\ln(\dot{\epsilon} k_B T) + E_a}{\sigma} \tag{5.1}$$

With the MRI 6002.3 being a proprietary polymer, the activation energy was unknown so a representative value of 15000J/mol was chosen [99]. The results can be seen in figure 5.3 which although not quantitatively correct, displays a rise in activation volume which is expected and demonstrated with the temperature of the material approaching the glass transition [77].

5.2 Investigation of Residual Stresses in Hot Embossed PS

It was proposed to investigate the mechanical state of a hot embossed sample locally and globally using different methods of mechanical testing. Using the ability to accurately locate individual tests, a large number of indents were performed with a

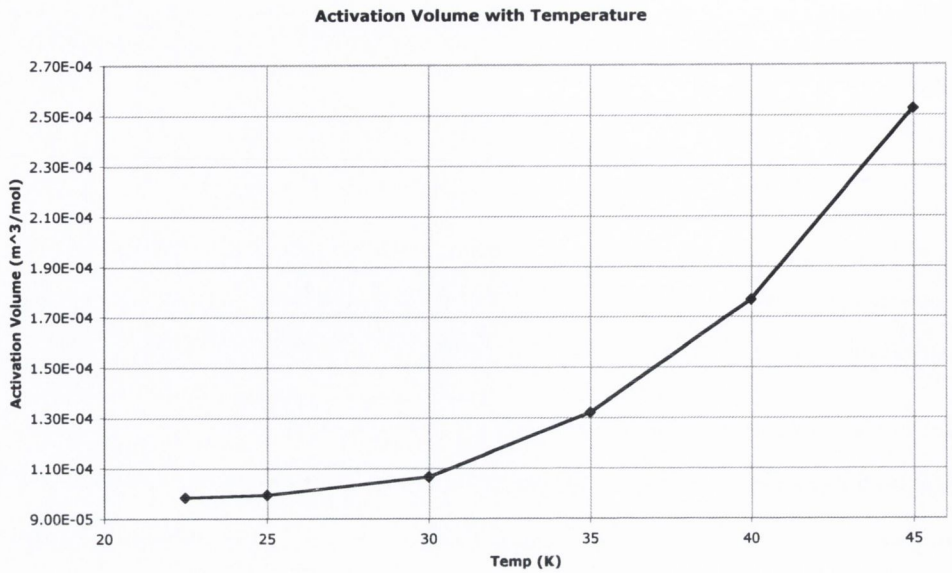

Figure 5.3: An estimate of the variation of the Activation Volume vs. Temperature for the MRI 6002.3 photoresist.

berkovich tip on a samples of differing molecular weights, both pristine and prepared with hot embossing. Also, a relatively large sphere was used to compress several embossed lines in order to try and obtain non localised data.

5.2.1 Localised Testing

A 40μm wide line was hot embossed into a 270 ± 10nm film of polystyrene with M_W = 58k by H.C. Scheer and H. Schulz of the University of Wuppertal [5]. Figure 5.4 shows an AFM image of part of this line. In this sample, three areas of interest are visible, the residual layer in the centre, extruded pileup on either side of the trench and unextruded material flanking the pileup. Elastic recovery of the residual material in the centre of the trench can be clearly seen. This is exhibited as a ridge between rows 9 and 10.

A 10x10 array of 100nm deep indents were performed on the sample, the indents were placed to examine the properties of the three areas of interest. The dynamic modulus and hardness data were obtained and are presented in figure 5.5 and 5.6 respectively. Indents into uncoated substrate of silicon (1 0 0) show a steady modulus of ~ 135GPa

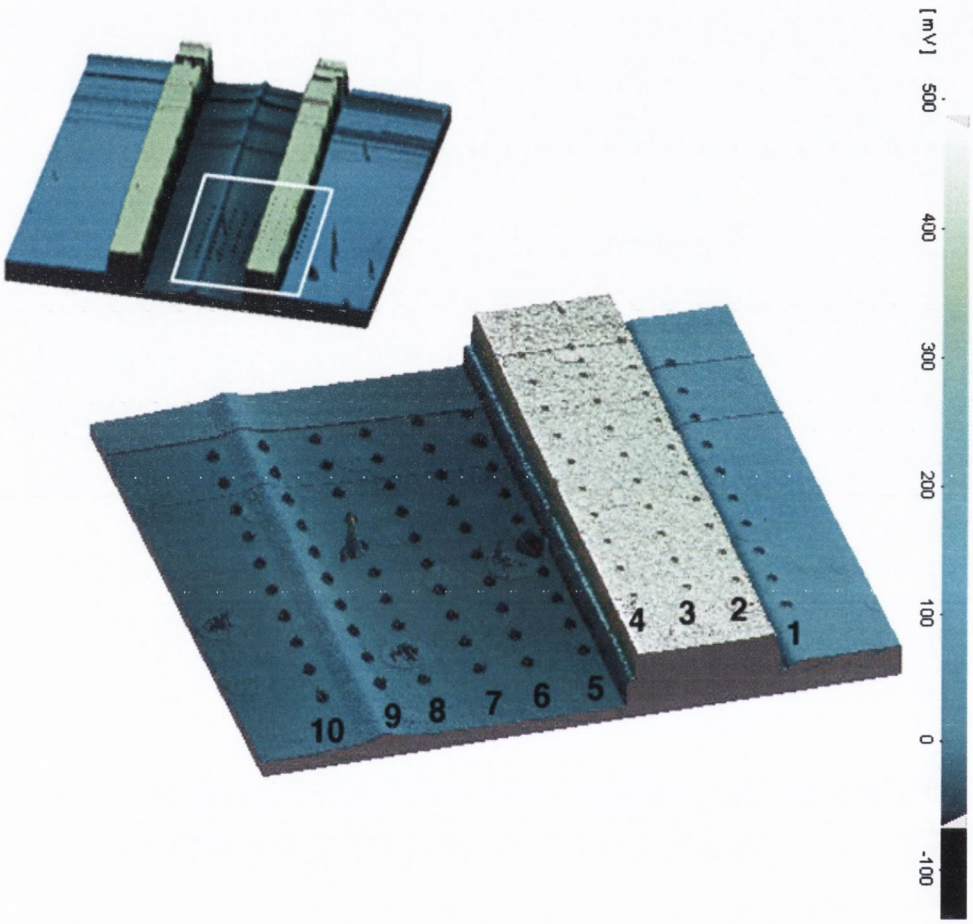

Figure 5.4: AFM scan of a 10x10 test array performed in the nanoindenter with a Berkovich tip on a sample of polystyrene that had been formed using Hot Embossing.

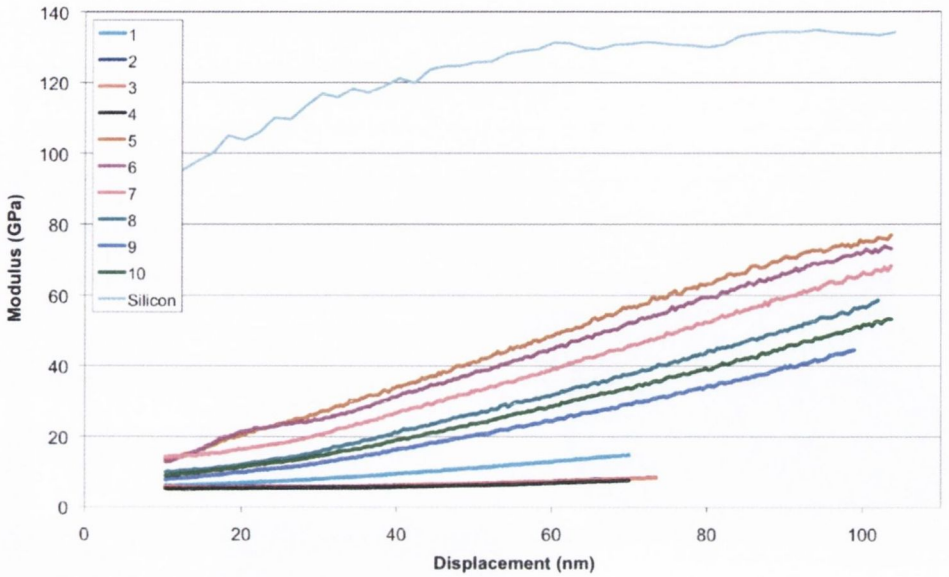

Figure 5.5: Modulus tests as a function of depth on embossed Polystyrene of M_W 58k.

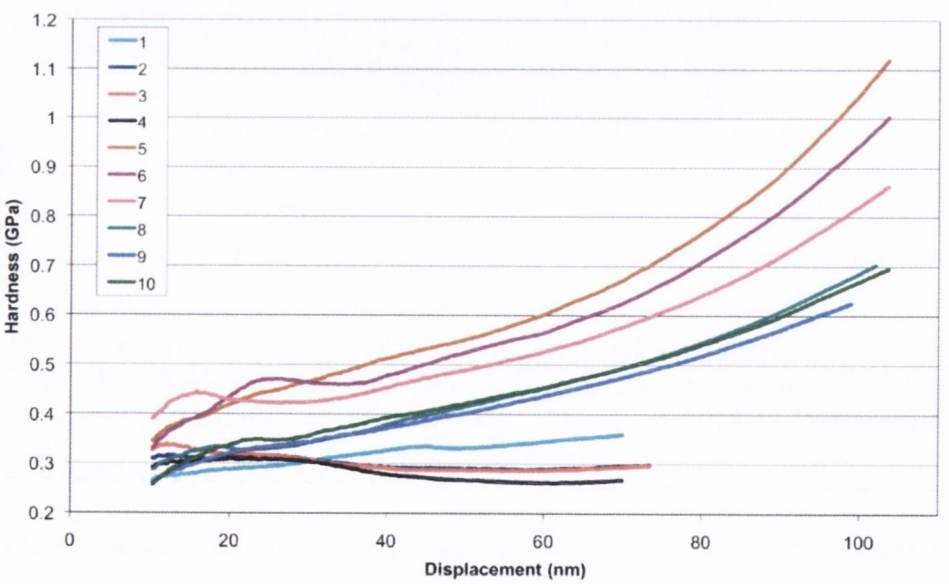

Figure 5.6: Hardness as a function of depth on embossed Polystyrene of M_W 58k.

occurring beyond a penetration depth of ~ 45nm. This indicates that the influence of tip effects diminishes after this point. Rows 5-10 show the influence of substrate with an increase in modulus, with indents 5,6 & 7 showing the largest effects due to being on a thinner part of the substrate. Indents on rows 2-4 do not display this behaviour, being incident on the thicker extruded portion of the sample. Hardness is less affected by the substrate, as can be seen in figure 5.6. It is demonstrated by rows 2-4 reaching a constant hardness value of ~ 0.26GPa that the material properties are generally homogenous in the extruded pileup. Row 4 shows a slight deviation due to it being close to the edge of the extruded area and thus having a lower constraint from surrounding material. Row 1 on the thinner unflowed region displays a slight increase, again due to substrate influence. Again, it can be seen that rows 5, 6 & 7 have a higher hardness than the remainder of the rows. This may be due to the variation in thickness of the residual layer which increases in thickness towards rows 8, 9 & 10, as can be seen in the AFM scan. The hardness value for the silicon reached a plateau of ~ 11.2GPa but is not shown in this test in order to display the data at maximum dynamic range.

The substrate effect is clear in the all these plots as the modulus increases with depth and is a well known problem when measuring thin films [68, 100, 101]. Unlike modulus, hardness measurements are not as sensitive to substrate effects, with indent data being useful at depths up-to 50% of the film thickness. The local testing shows no significant increase in hardness due to extrusion process in hot embossing. It is also demonstrated that the parasitic effect of the substrate hardness limited the usefulness of measurements. S.J. Bull has outlined a method by which such a system can be modeled [101].

Further tests were carried out on four samples, pristine unembossed samples and embossed samples using 2 molecular weights, 58k and 382k. For the embossed samples the indents were placed on the extruded material. The results of these tests are detailed in figure 5.7. The modulus curves, influenced by the substrate, are convergent on a value of 3GPa. The hardness plot shows no significant difference in any of the samples.

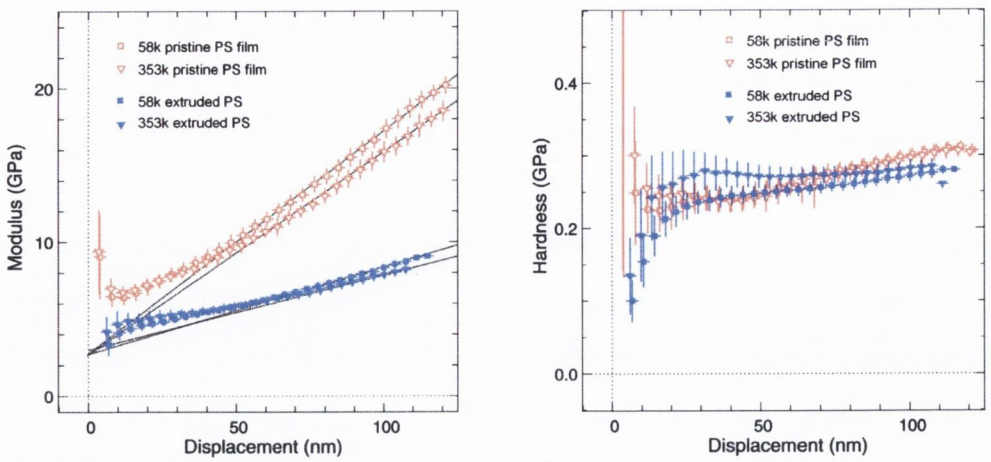

Figure 5.7: Modulus and hardness data comparing pristine and extruded films of polystyrene of differing molecular weights. The modulus curves, influenced by the substrate, are convergent on a value of 3GPa. The hardness plot shows no significant difference.

5.2.2 Non-Localised Testing

Tests on the non local scale involved using a polished 1mm diameter silicon sphere discussed in Section 3.4.1. The sphere was introduced to the substrate and loaded to induce plastic deformation. Work was carried out on 400nm lines which had been formed in a similar manner to the 40μm lines discussed in the previous section. Examination of figure 5.8 shows no appreciable difference in measurements due to strain hardening. At a depth of 270nm, the Load vs. Displacement slope displays a convergence of the the curves of the pristine film and the embossed film, also figure 5.8. This may be due to the trenches between the lines being filled and the behaviour approaching that of an undeformed film and this is supported by the AFM data of the indent. Note that once again the elastic straining of the substrate affects the data. Although defects exist in this sample, their number was small relative to the rest of the sample tested by the sphere and had a negligible effect.

In summary, strain hardening nor any other significant difference in mechanical state was observed in any of the tests performed. For imprinted or embossed patterns to be viable as etch masks, certain criteria must be met, see Section 1.1.2. See [5] for greater detail.

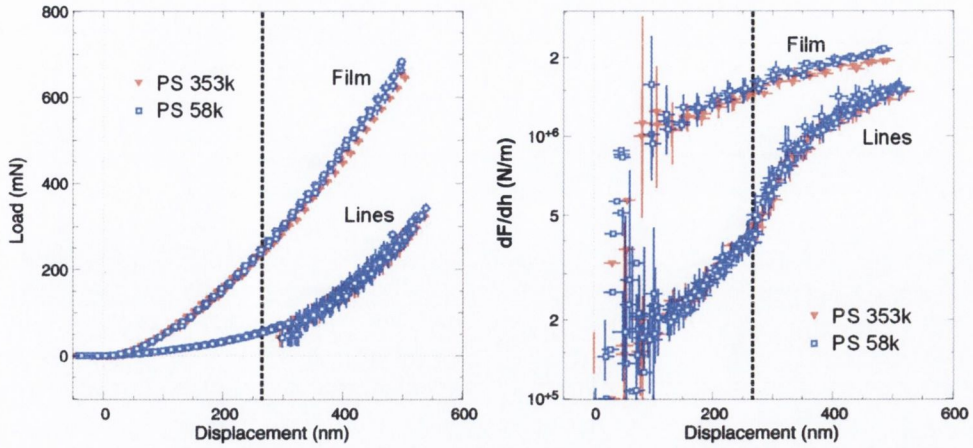

Figure 5.8: Non-localised testing of embossed 400nm lines in polystyrene using a silicon sphere of 1mm diameter. The load-slope versus displacement on the right (determined from the load versus displacement curve on the left) shows a convergence to the same values, indicating a lack of strain hardening or any other significant difference in mechanical state.

5.3 Forming using an Applied Normal Force

In order to determine the mechanisms for the forming operations it was decided to simplify the geometry thus simplifying the measurements and analysis. The geometry of squeeze flow was investigated, in incarnations of "coupon crushing" and the "flat punch" geometry. Squeeze flow was chosen because of it's relevance regarding forging operations as it is the dominant mode of generating flow to achieve a desired geometry in imprint. Whilst squeeze flow generates complex velocity gradients, it is known to generate high shear rates [42], thus resulting in high levels of plasticity (section 2.3.2). Assuming no-slip and incompressibility, the forming load required to maintain a constant stamp velocity scales with the size of the stamp and the residual height of the material under the stamp [12]. This is usually manifested as a slowdown and cessation in the thinning of the material under the stamp as discussed in section 2.2.4.

Figure 5.9 shows the differences between coupon crushing and the flat punch. The coupon is a simple 'slug' of material on the substrate, unconstrained at the sides and is free to move in the lateral direction. The flat punch geometry allows a similar study,

but provides constraining effects due to the surrounding film as well as a constant area over which the force is applied.

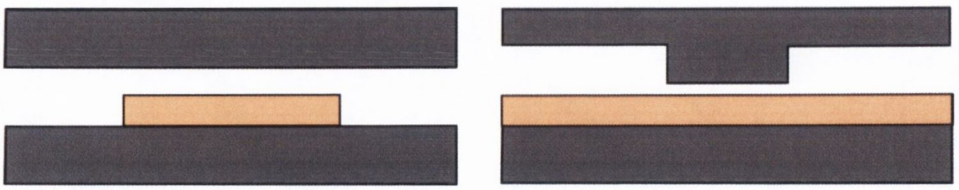

Figure 5.9: Geometries which exhibit squeeze flow. A deformable coupon between rigid substrate and stamp(left) and a rigid flat punch deforming a thin film supported by a rigid substrate (right).

The load-displacement curves for the coupon and flat punch have a some elements in common. Figure 5.10 shows simplified load-displacement curves for squeeze flow geometries with assumed large thicknesses of plastic material. Initially there exists an elastic loading segment, followed by a plastic yield plateau. Plastic yield is identified by the application of force above a threshold called the yield stress (section 2.3.2) which results in plastic flow.

In reality, the finite thicknesses of the plastic materials supported by rigid substrates shown lead to load-displacement curves more like those shown in figure 5.11 and described in equation 2.1 where after the plastic forming plateau, the forming load has to increase to maintain a constant stamp velocity as the film thins.

With a coupon (figure 5.10(a)), the lack of constraint provides a lower yield point (section 2.3.2), but the increasing area of contact as the coupon deforms results in an increase in the force required to provide yielding [64, 102]. Friction also plays a part, with full stick at the boundaries resulting in undeformed conical volumes due to the opposition of flow [64, 42]. As material is extruded from the edges, these conical volumes eventually overlap, and a rise in the stress is required to cause a strain with the eventual extinguishing of plasticity. Lubricating the boundaries reduces the stress required to produce a given strain. In general, the variation in applied force, L, applied to the coupon is related to the vertical height of the coupon, h, by $L \propto \frac{1}{h}$ [10]. The results for the coupon experiments are discussed in section 5.3.1.

The flat punch geometry (figure 5.10(b)) into a film behaves in a similar manner to

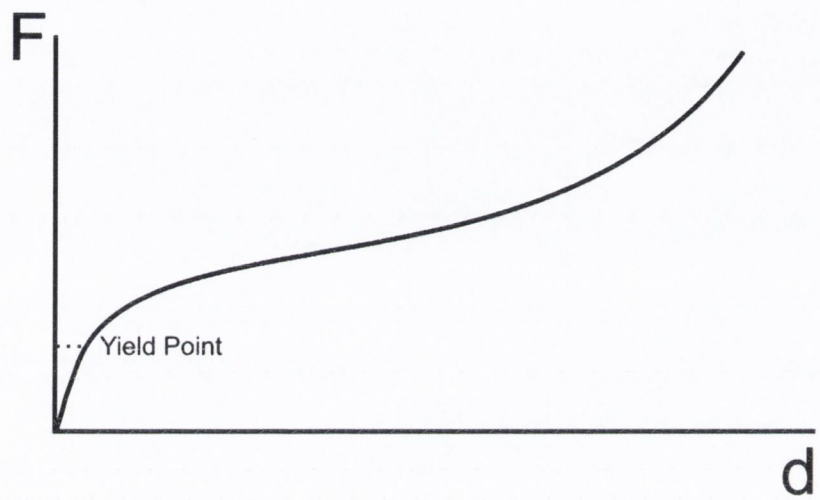

(a) Example of F vs. d curve for coupon crushing geometry.

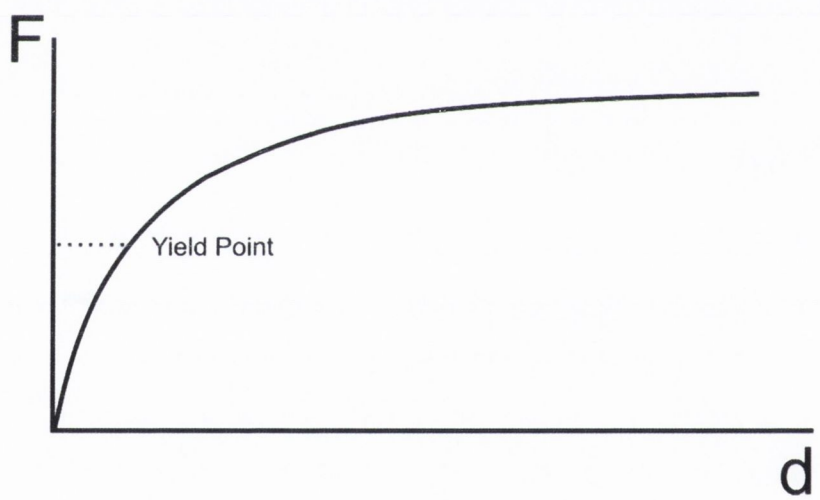

(b) Example of F vs. d curve for flat punch geometry.

Figure 5.10: Idealised load versus displacement curve for idealised squeeze flow using a flat punch on a bulk substrate.

the coupon, although there are differences. The constraining effects arising from the surrounding film require a higher stress to initiate plasticity. As with the coupon, the presence of friction at the boundaries also affects matters with an increase in stiffness being observed followed by the extinguishing of plasticity. The flat punch results are discussed in section 5.3.2.

Figure 5.11 illustrates typical experimental results whilst using a flat punch. Firstly, the stamp is not perfectly aligned and a depth of $5-15$nm must be achieved before the punch is in complete contact with the substrate. Directly following this is the initial elastic loading. Following this, the yield point is clear and so is the subsequent rise in stress required to continue deformation. The HCS does not vary greatly during plastic deformation but shows a sharp upturn when the effect of the substrate is "felt". For a squeeze flow geometry, an important point is that H & E plots are invalid as they are dependent on knowing the contact area correctly (section 2.6.2). However, comparisons or corrections to the H & E calculations may be made within the context of a single stamp.

5.3.1 Coupon Experiments

An investigation into mechanical flow processes was carried out by using the FIB to mill a film of isotactic PMMA into coupons and ring geometries. An SEM of one of these coupon is shown in figure 5.12. Once the coupon had been machined, it was subjected to squeeze flow using a silicon sphere. Because the diameter of the sphere is large (1mm) compared to the coupon it is effectively a parallel plate for effecting squeeze flow.

Figure 5.13 shows an AFM image of a FIB milled coupon before and after compression with a plain silicon sphere. The coupon was 2.2μm in height with a 5μm radius before compression and a peak height of ~ 1.4μm and a radius of ~ 6μm afterwards. The trough, visible at the base of the coupon before deformation, which was a FIB milling artifact has been covered over.

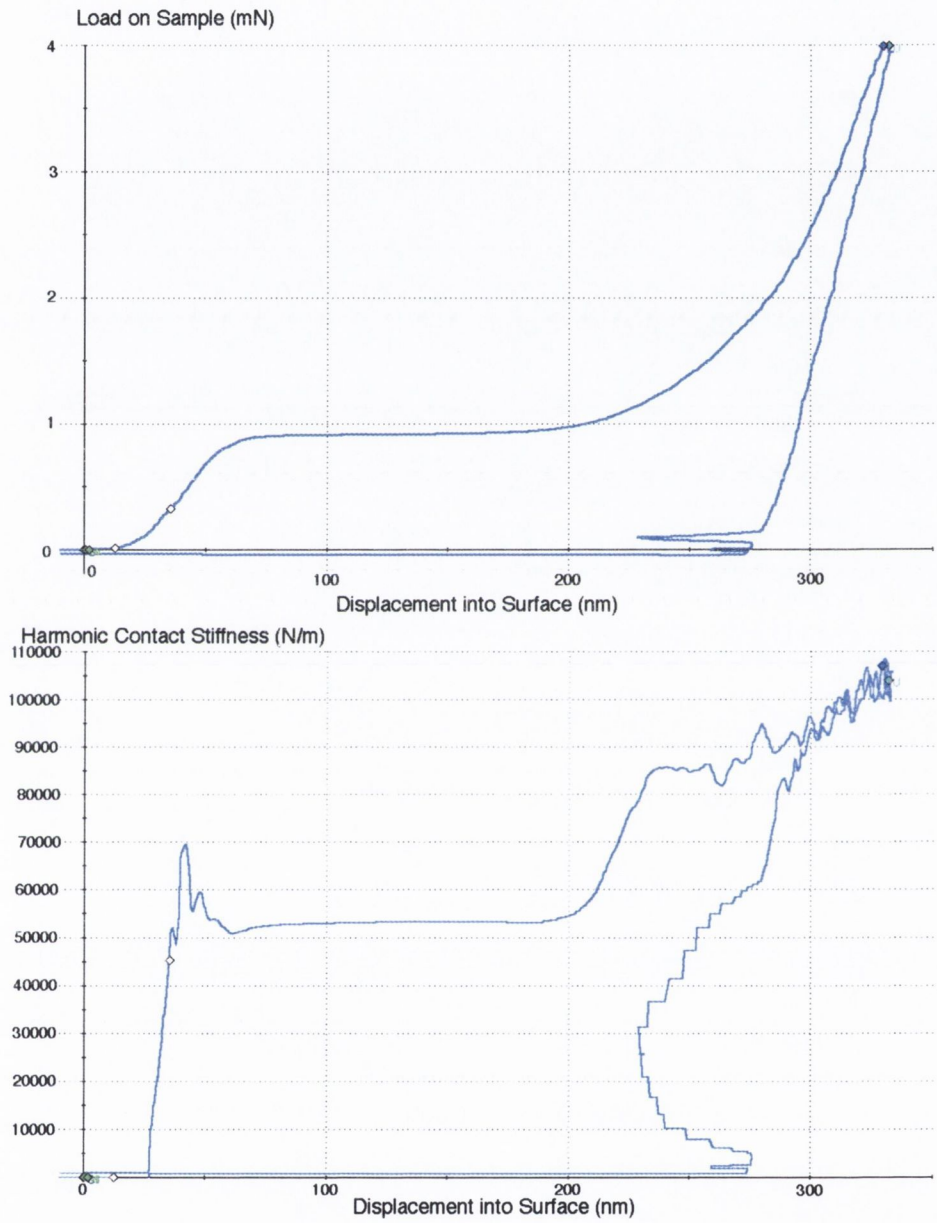

Figure 5.11: Examples of Load and Harmonic Contact Stiffness behaviour during a squeeze flow experiment, namely the indentation of a cylindrical flat punch into a deformable thin film.

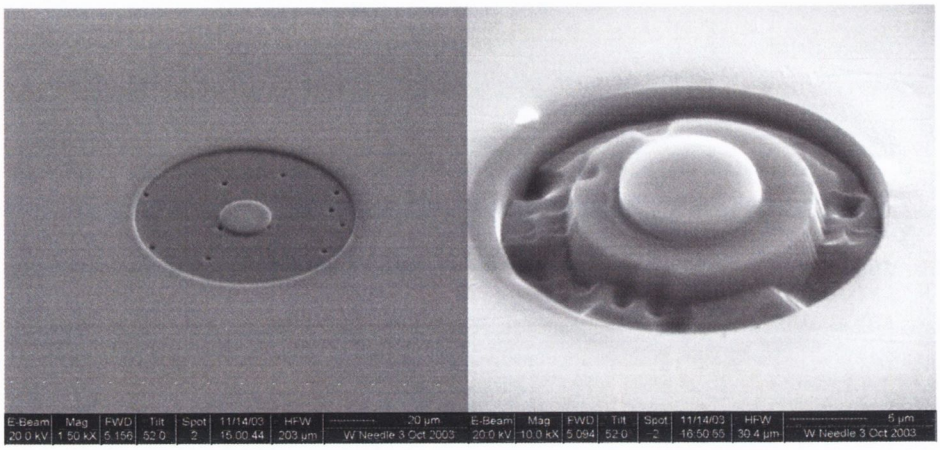

Figure 5.12: SEM images of coupons during FIB milling.

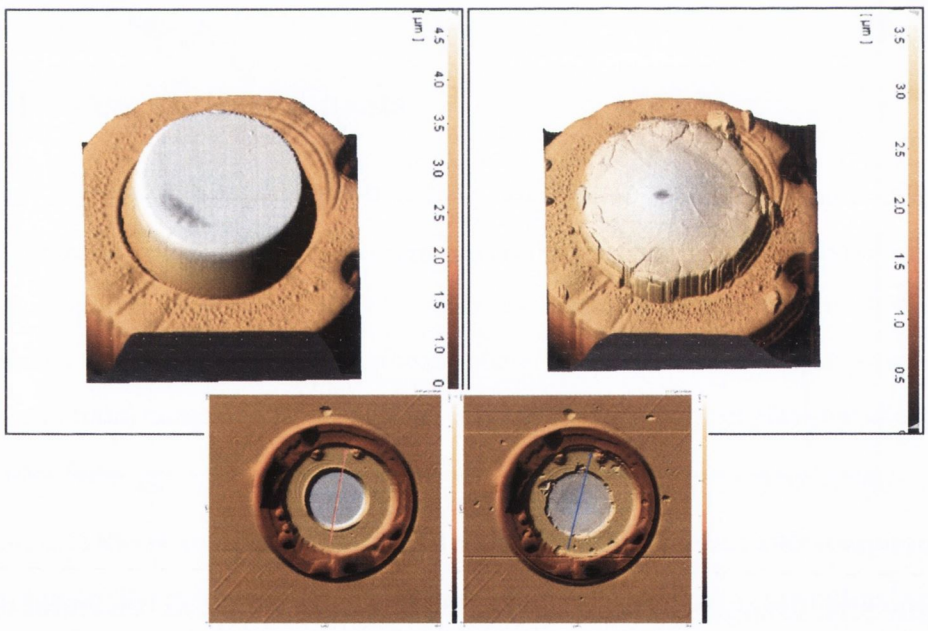

Figure 5.13: AFM images of a PMMA coupon of 2.2µm in height with a 5µm radius before (left) and after (right) compression with a plain silicon sphere.

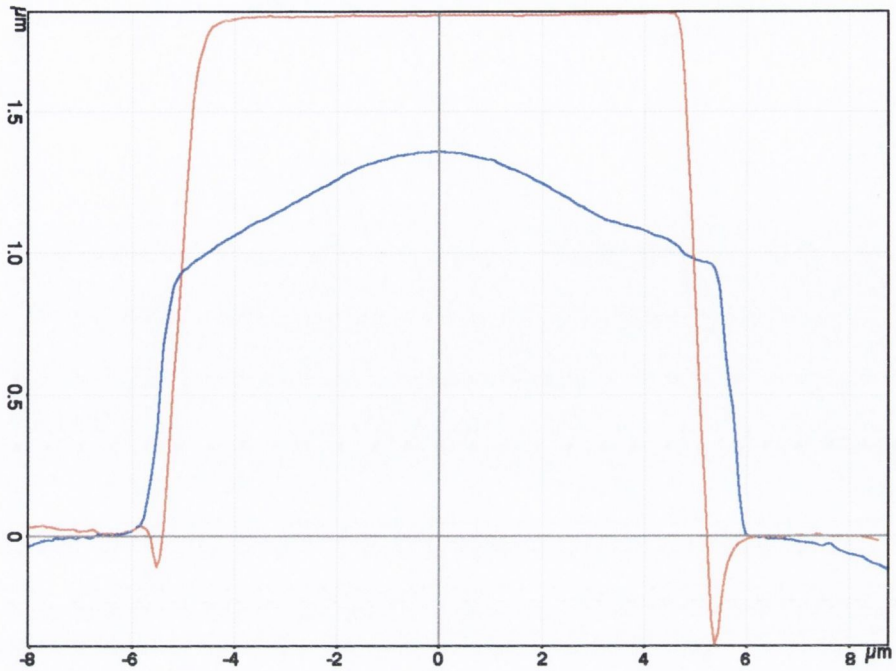

Figure 5.14: Coupon profiles taken from the AFM images in figure 5.13 before (Red) and after (Blue) deformation with

The coupon is seen to exhibit elastic recovery, which can be seen in the centre of the coupon, giving it a dome shape. This can also be seen in the AFM profile where the green trace is before deformation and the red trace after, figure 5.14. Cracks and chips of material can be seen, having separated from the sides of the main body, as well as the reproduction of scratches on the silicon sphere. This elastic recovery of the dome arises from the fact that volumes of material about the centre of the coupon are prohibited from yielding. Because material has not yielded, it is only compressed elastically and so recovers to it's original state when external forces are removed. Yielding is prevented, even if the yield stress has been exceeded by constraining forces from surrounding material. This is expressed as an area where velocities of material are zero in slip line theory [103] [10]. Other models describe this material as a constrained hydrostatic volume [9]. Simply put, plastic deformation exists only where it is allowed, if material which has exceeded the yield stress has somewhere to go, then it will flow, section 2.3.2.

Domed elastic recovery is also seen in the flat punch geometry experiments. Consider

the AFM profiles of a flat punch indent (figure 5.19 in section 5.3.2) at a peak pressure of 1300MPa. Unfortunately, reliable mechanical data for the coupon experiments is unavailable for this experiment due to issues with the x-y stage.

A volume change of the coupon after the deformation was observed. Many forging operations on many scales rely on the fact that the process of forging is volume conserving. If this phase change occurs at a particular strain threshold, the possibility of areas of varying density arising from the strain gradient exists. These density variations would be manifested as areas of differing properties, and could make the material unsuitable for some processes. To quantify the extent of the change, the volume of the coupon before and after was calculated using shell integration. Shell integration involves dividing the coupon into a series of concentric cylinders. The volume of each of these cylinders were calculated separately and then added together to obtain total volume of the solid. The equation used was

$$V = \sum_{i=1}^{n} 2\pi\, r_n\, h_n\, \Delta t \tag{5.2}$$

where for n sections, r_n is the average radius of the section, h_n is the height of the section and Δt is the thickness. For this measurement, a profile of the coupon similar to that in figure 5.14 was divided into 12 sections from the center to an edge. Considerations to the measurements are as follows, anomalies due to shed material were avoided in the cross section and due to AFM tip convolution (more details on AFM imaging artifacts can be found in section 4.6, the bases of the coupons appear wider than they actually are.

An initial volume of about $147\mu m^3$ appears to be reduced to $110\mu m^3$, or 25% of the original volume. The volume change may be due to a combination of phenomena. Reduction of free volume, the presence of residual hydrostatic stresses in the final shape, the loss of material through fractures, creating debris which separates from the main body.

Experimental and theoretical data suggests that plastic deformation through reduc-

tion of free volume due to hydrostatic pressure is not significant, as the free volume of an amorphous organic glass has been postulated to be on the order of between 2.5% [51, 63, 76] and 11.3% [58]. However, removal of this free volume would not result in the huge compressibility of over 70% postulated by Lee et al [48]. However, the film used for the coupon experiments was quenched (see section 4.2.1)and so the increased free volume associated with spin coating from a solution was frozen in. Fragments of material which have detached from the coupon can be seen in the AFM scan, however these fragments are not expected to account for such a large loss of material, as the integrity of the coupon appears mostly intact from the AFM scans. Another contributor to the volume change may be the tacticity of the polymer, for this particular experiement an isotactic polymer was used and such materials have been known to exhibit a phase change from glassy to crystalline, resulting in a change in packing efficiency and therefore density [58]. It is possible that a combination of all these phenomena contributed to the observed volume change.

5.3.2 Flat Punch Forming Using Normal Loading

The impression of a flat punch into a planar film, described in figure 5.9, was a closer approximation to the scenario of feature manufacture in imprint lithography, a planar film is an easier target to hit than a coupon. Starting with a planar film, the contact area of the punch is constant but the constraint of the surrounding film and how it varies depending on the amount of material under the punch.

Figure 5.15 shows SEM images of a typical flat punch milled from a silicon sphere (see section 4.1), in this case stamp "H", 6μm in diameter. On the left, the wide 60μm cut can be seen, which was used to remove surrounding material and thus prevent any other parts of the sphere from coming into contact with the film[2].

Figure 5.16 shows experimental force-displacement curves for a flat punch in films of different thicknesses. The bulk film exhibits behaviour similar to that of the idealised behaviour shown in figure 5.10. The substrate effects can be seen quite clearly where

[2]A list of stamps used in the project can be found in tables 3.1 and 3.2.

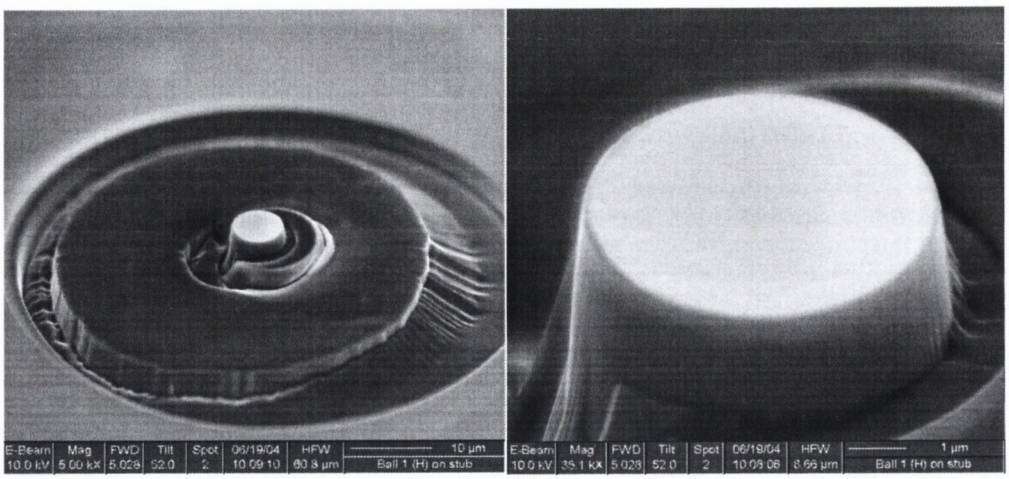

Figure 5.15: SEM images of flat silicon punch "H", 6µm in diameter.

films of X and Y were used.

Using a flat punch (entitled "Arwyn") of diameter 7400nm and 2200nm height, a series of experiments were carried out. Firstly the conformity of the film at different loads and extruded thicknesses was examined. Secondly, an examination of the variation of different film thicknesses on the residual layer was undertaken. The flat punch was milled from from a silicon sphere as detailed in section 4.1. A series of PVAc films were prepared, (section 3.4.2), of thickness 500, 900, 1310, 2200nm and also a bulk sample of the same polymer.

Film Conformity

It can be seen from figure 5.16 that there are common features to the plots. This is the typical signature of a flat punch indented into a glassy material. Firstly there is the initial (mostly) elastic loading (1). This is followed by the plastic turnover point at which the load is constant (2). Finally, the load begins to rise as the layer of polymer under the punch thins and the influence of the substrate is felt (3). Loading is halted and held at a certain point during which creep flow will become apparent (4). The load is then reversed withdrawing the punch from the surface (5).

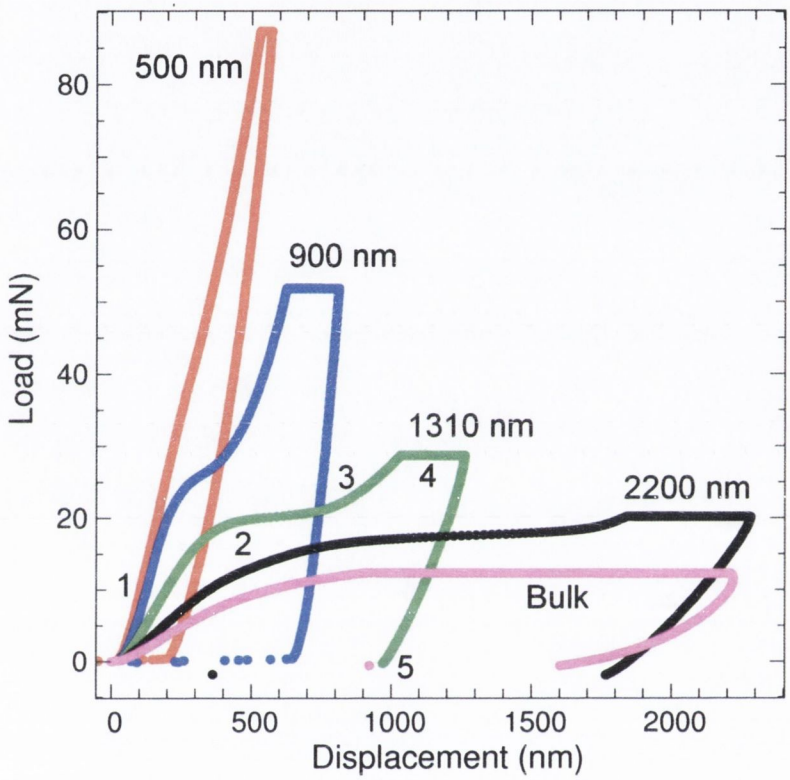

Figure 5.16: Load vs. Displacement curves for a flat punch into films of varying thicknesses displaying common traits of a flat punch indented into a glassy material. Firstly there is the initial (mostly) elastic loading (1). This is followed by the plastic turnover point at which the load is constant (2). Finally, the load begins to rise as the layer of polymer under the punch thins and the influence of the substrate is felt (3). Loading is halted and held at a certain point during which creep flow will become apparent (4). The load is then reversed withdrawing the punch from the surface (5).

Residual Layer

The residual film thickness (h_r) was obtained for the four different known film thicknesses (see section 4.2 for film measurement details), 2000nm, 1500nm, 1000nm, 500nm. The residual height could not be obtained for the bulk sample as it was of greater thickness than the stamp. Figure 5.17 utilises the data shown in figure 5.16, where the indenter displacement data is subtracted from the known film thickness, resulting in the residual thickness of the deformed film. The peak pressure is calculated from the applied load divided by the area of the stamp. Above 200MPa, the plastic yield threshold is reached and results in large excursions. Once h_r reaches ~ 350nm, further increases in applied pressure fail to reduce h_r. It appears that this limit occurs regardless of the initial film thickness and the applied pressure. This indicates that the h_r is dependent on the width of the punch. Similar effects have been noticed in squeeze flow geometries during rheology testing where the material between the parallel plates of the rheometer and the squeeze velocity asymptotically approaches zero over time periods > 5000s [42] [104].

For the 1310nm film, the effects of different pressures on the film were investigated. The load points chosen were,

- Before main plastic turnover at 120 MPa.
- During the plastic turnover at 260 MPa.
- After yield has extinguished at 1310 MPa.

AFM scans were taken of each of these tests. Figure 5.18 is an example of an AFM scan of a flat punch imprint. Figure 5.19 shows a series of superimposed profiles from AFM scans of indents as differing applied pressures. The 120 MPa point showed only some plastic deformation at the stamp edges as expected. A flat, uniform profile was exhibited at 260 MPa, whilst at 1310 MPa a convex residual layer was produced, due in part to deformation of the flat punch and in part to elastic behaviour of the residual layer and substrate.

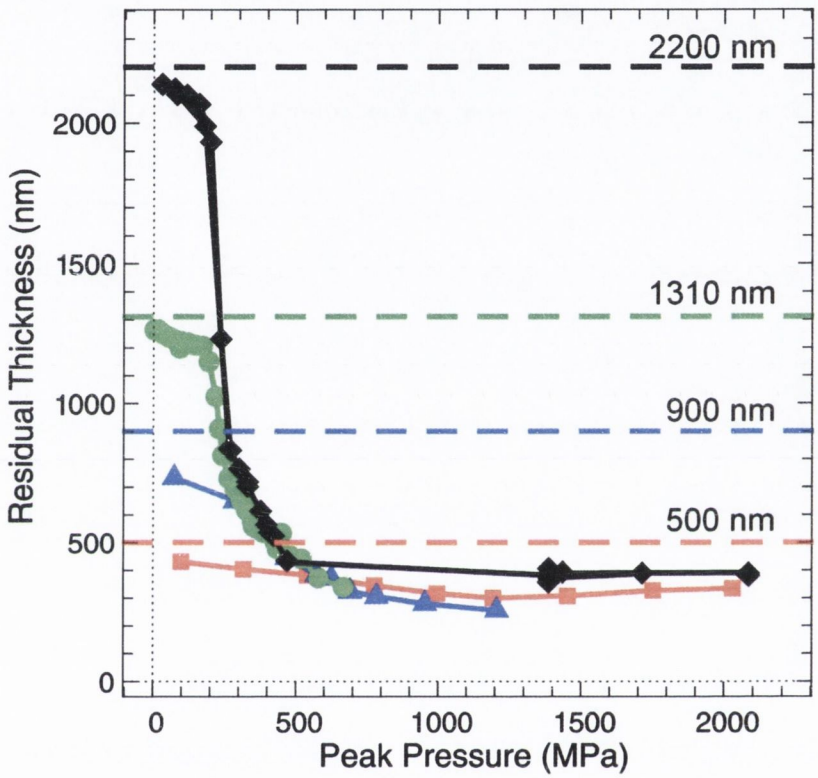

Figure 5.17: Variation of residual polymer thickness with peak applied pressure for 4 films of different thicknesses. Above 200MPa, the plastic yield threshold is reached and results in large excursions. Once h_r reaches ~ 350nm, further increases in applied pressure fail to reduce h_r. This limit occurs regardless of the initial film thickness and the applied pressure.

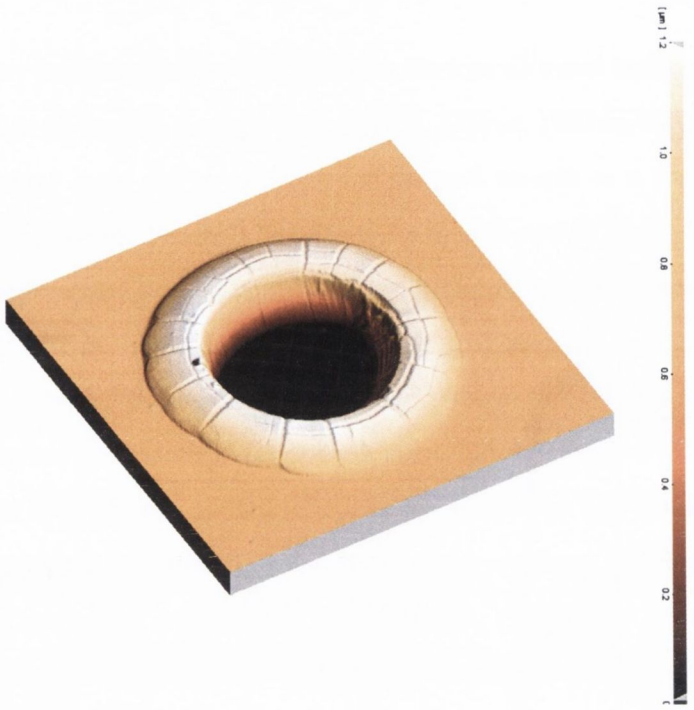

Figure 5.18: AFM scan of a flat punch imprint produced in this series of experiments.

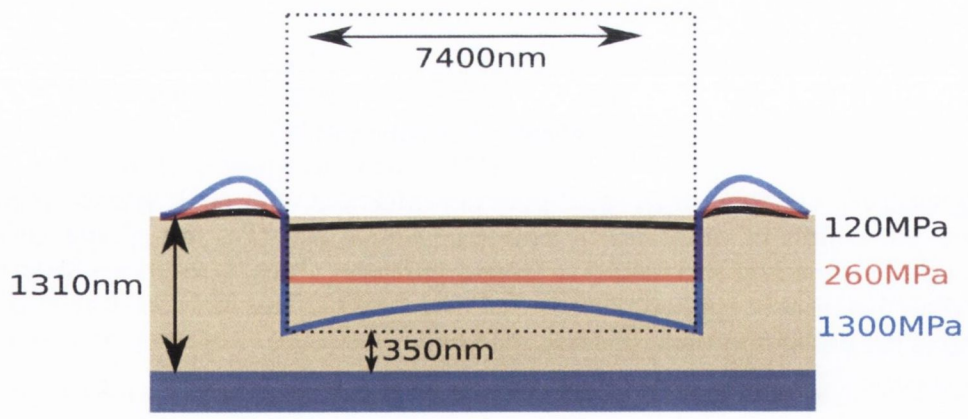

Figure 5.19: A series of superimposed profiles from AFM scans of indents as differing applied pressures. The 120 MPa point showed only some plastic deformation at the stamp edges as expected. A flat, uniform profile was exhibited at 260 MPa, whilst at 1310 MPa a convex residual layer was produced, due in part to deformation of the flat punch and in part to elastic behaviour of the residual layer and substrate.

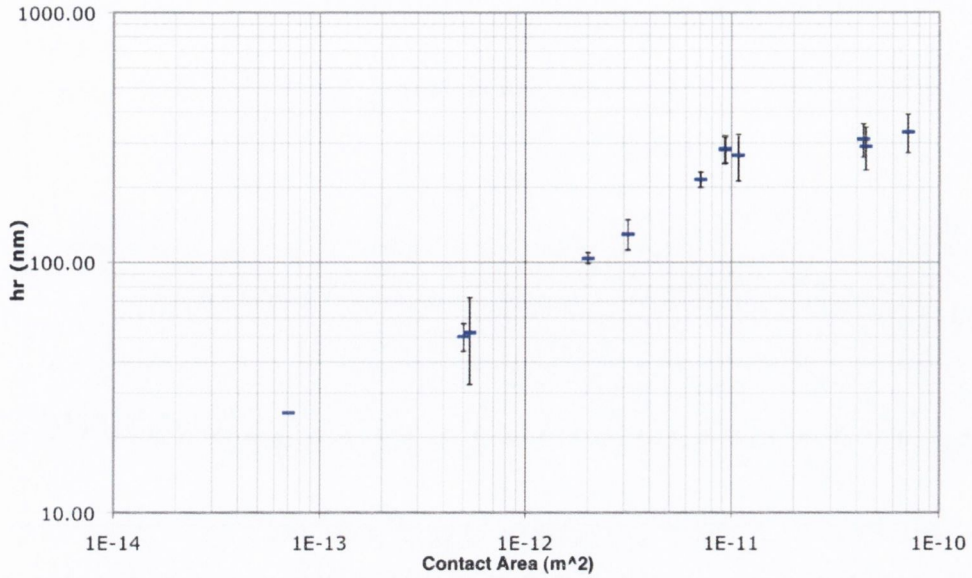

Figure 5.20: Effects of Punch size. Variation of residual height (h_r) with contact area for differing sizes of circular flat punches.

The non-uniformity of the residual layer may be due to a combination of relaxation of the elastic zone created in the substrate under the indenter and also to a deformation of the flat punch at high loads. These processes also produce effects seen in the coupon experiments (section 5.3.1) resulting in a similar domed shape after the deformation suggesting elastic recovery of the area beneath the center of the stamp. This suggests that this forming geometry is creating circumstances where shear strains are prevented from driving plasticity.

It was postulated from the data shown in figure 5.17, that the residual height of ~ 400nm, was dependent on the size of the punch. Figure 5.20 shows the a summary of h_r measurements for a number of circular flat punches used in this project. It can be seen that as the punch size scales to zero and begins to approximate a cutting edge, h_r also trends to zero. The shape of the curve also appears to show a size effect where the slope changes for punches of a diameter smaller than 3.5μm.

Apart from size, punch geometry appears to have significant effects. Figure 5.21 shows the differences between the rectangular plane strain stamps and the circular flat punches based on the contact area of the stamps. Although the contact areas of

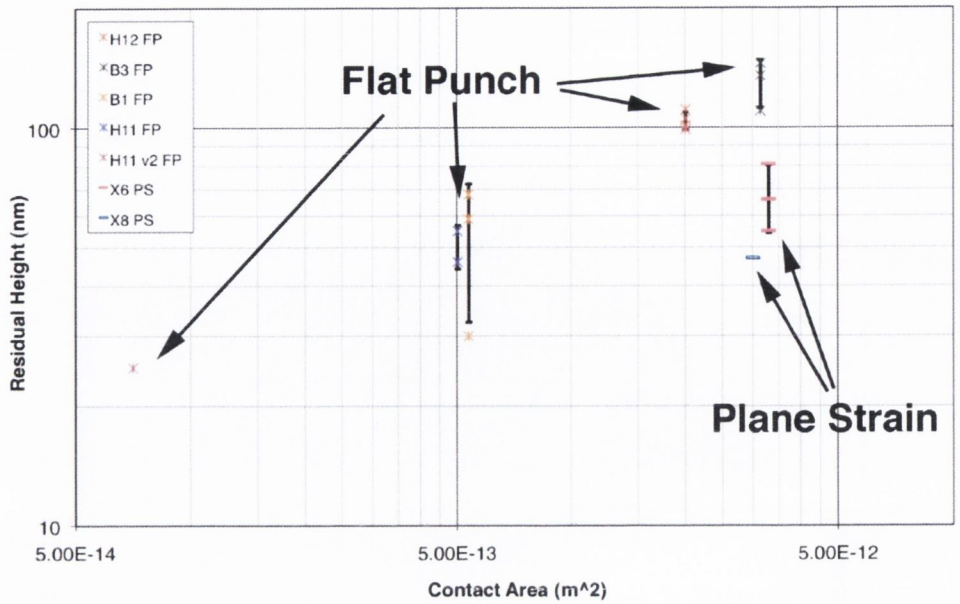

Figure 5.21: Effects of Punch geometry. Contact area versus residual height (h_r) for Flat Punch and Plane Strain Stamps. Even though contact areas of the plane strain stamps X6 and X8 are on the same order as stamp B3, the plane strain stamps show an improvement in the reduction of h_r.

the plane strain stamps X6 and X8 are on the same order as stamp B3, the plane strain stamps show a decrease in h_r over the flat punches. This may be explained by the fact that the smallest dimensions of the plane strain stamps are 610nm and 510nm for X8 and X6 respectively, smaller than the H11 stamp. Even so, while it appears that the smallest dimension dominates, it may still be offset somewhat by the length of the stamps (on the order of 6000nm). Continual reduction of a feature dimension towards zero means that the geometry begins to approximate a cutting edge which is effectively a stress concentrator. This would suggest that for single asperities with feature sizes of ~ 500nm and below, geometrical asymmetries have little bearing on residual height.

Elastic strains within the stamping setup.

It can be seen that the yield stress of the polymer under the punch rises as the film thins, resulting in an extinguishing of flow (see section 2.4). Assuming slip conditions

and the following values, $E_{Si} = 150GPa$, $E_{poly} = 1.2GPa$, $h_p = 2200nm$, $h_r = 350nm$ and $a = 3700nm$ the following were calculated,

Flat punch of silicon,

$$S_a = \frac{\pi a^2 E_{Si}}{h_p} = 2.9MN/m \tag{5.3}$$

Polymer plug underneath the flat punch,

$$S_b = \frac{\pi a^2 E_{poly}}{h_p} = 0.6MN/m \tag{5.4}$$

Silicon half spaces,

$$S_c = \frac{2aE_{Si}}{(1-\nu^2)} = 1.2MN/m \tag{5.5}$$

This series of springs results in a total stiffness of 0.27N/m.

Removal of simplifications such as providing a no-slip condition at interfaces and allowing for the constraining effects of surrounding material result in an significantly increased stiffness of the polymer rising from 0.6MN/m to 30MN/m. Figure 5.22 is a diagram showing the flat punch indenting the polymer and the associated pressures for each part. Pileup and stamp and substrate deformations are exaggerated for clarity.

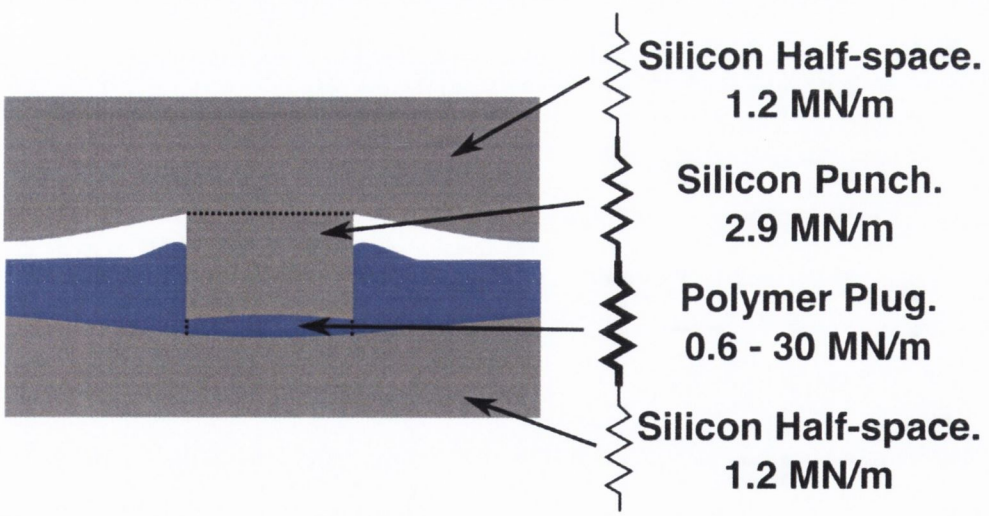

Figure 5.22: Schematic of an indented system at peak load and the components of a 4-spring system described above.

From this analysis, it can be concluded that when the polymer plasticity ends and it's spring constant rises, the majority of the strain in the system is in the silicon half spaces. This analysis concludes that increasing load will produce no further significant gains in the reduction of the residual layer using this method. Increasing load also produces elastic deformation, straying from the intended geometry and there is also the chance of damaging the stamp at high pressures. Avoidance of substrate deformation is essential when considering some of the main applications for NIL, thus leading to the experiments described in section 6.1 where material is removed without application of excessive pressures [6].

Delamination

Although all the samples were prepared in the same manner, the phenomenon of delamination was rare, although present in some samples, particularly that of a particular film prepared using a 6%wt. polystyrene solution. The reason for the delamination in this particular film was unknown and was not observed in other films. It was highly localised in the area of the imprint and easily identified through stress/strain data, visual inspection and AFM scanning.

Figure 5.23 is a plot of indentation curves produced by the nanoindenter. As per a typical test, the load on the sample is ramped up to a predetermined peak value and held at a constant. The punch continues to move into the sample due to creep processes which gradually extinguish, and for this reason the shear is typically applied 20s after the peak load is achieved. Several instances of spontaneous excursions of the punch into the sample are observed indicating delamination. Although these events occur at different times, the majority of delaminations appear to occur when the indenter is maintaining a constant load.

Electron micrographs of delaminated and non-delaminated indents are shown in 5.24. Immediately obvious is the conical shape of the delaminated areas and the difference in pile-up caused by the lack of constraint. The reason for the lack of constraint is apparent in Figs.5.24(b) & 5.24(c), as the film has come away from the substrate. The

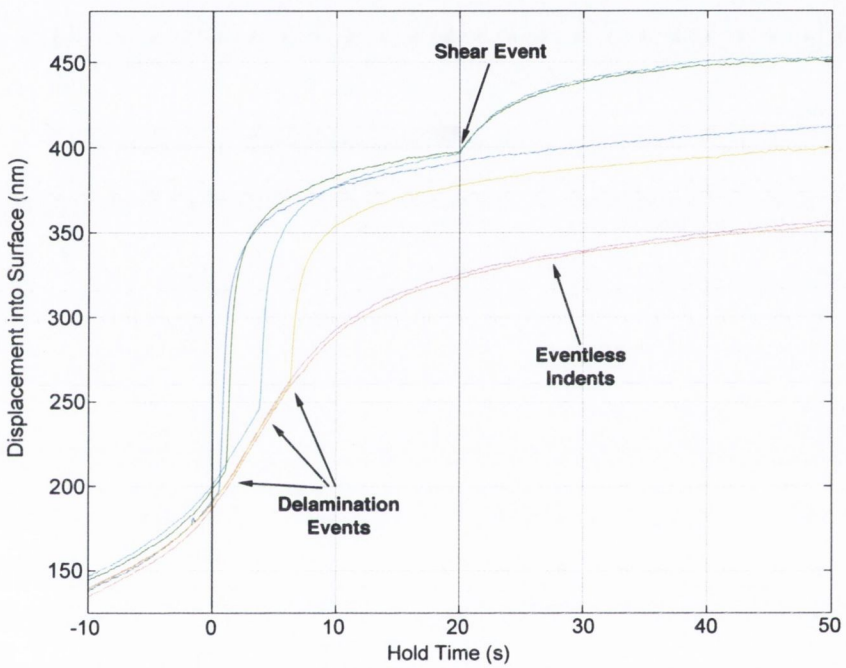

Figure 5.23: Indenter data showing different behaviours of a film under stress. Instances of spontaneous excursions of the punch into the sample are observed indicating delamination, ordinary eventless indents and shear driven plasticity.

material directly under the indent has not detached from the surface.

AFM reveals similar details with the profiles of 2 indents being compared in figure 5.25.

Several tests were performed, altering variables with the conclusion that delamination could not be deliberately induced (or prevented). Whilst one of the effects of delamination is to improve the residual height, it limits the proximity of neighboring features of the imprint process and therefore may be of limited use. Delamination did not appear to effect the shearing as evidenced by vibrometer data with no apparent difference between delaminated and ordinary indents. What may be of use is the unique signal provided by delamination, thus easing troubleshooting.

The elastic hydrostsatic core revealed itself in both geometries. This would suggest that the majority of constraint is due to the interfacial friction as the effect occurs regardless of the presence of surrounding material.

It has been shown that in increase in pressure leads to an increase in the activation energy [76] [105], however the limit to the performance can be explained via the phenomenon of the friction hill. The Friction hill (see section2.4.2) essentially traps material at the boundaries and restricts shearing strains despite the high pressures developed.

5.3.3 Conclusions

Normal forming is a ubiquitous process used within the nanoimprint community to selectively drive plasticity. Investigations were carried out to determine the limits of this technique.

An investigation into the effects of temperature on the variation of yield stress of a polymer were carried out. The system was found to behave as expected with a decrease in yield stress as the temperature increased. A mechanical testing study into the existence of residual stresses in a hot embossed sample resulted in no detectable difference between formed and unformed material.

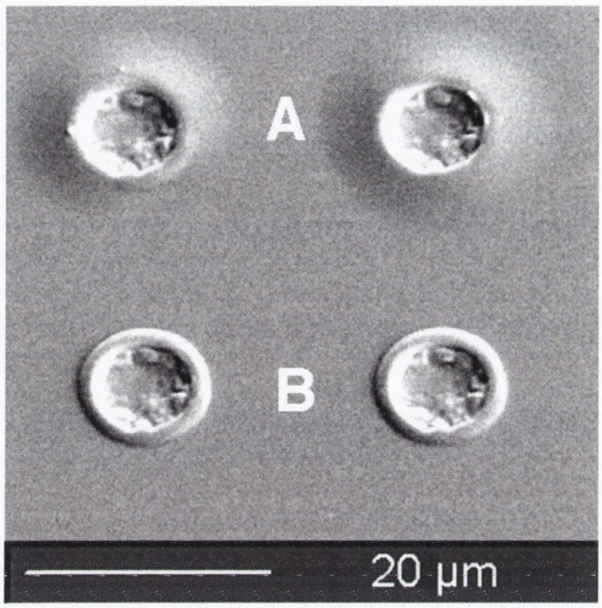

(a) Comparison of delaminated (A) and ordinary (B) indents formed with a flat punch.

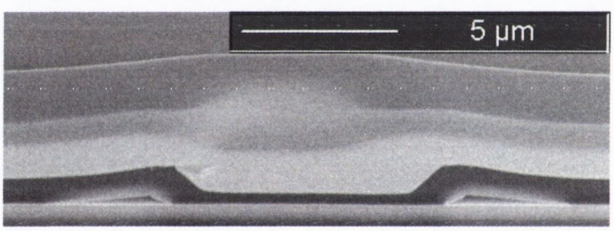

(b) Fib machines SEM image of a profile of a delaminated indent.

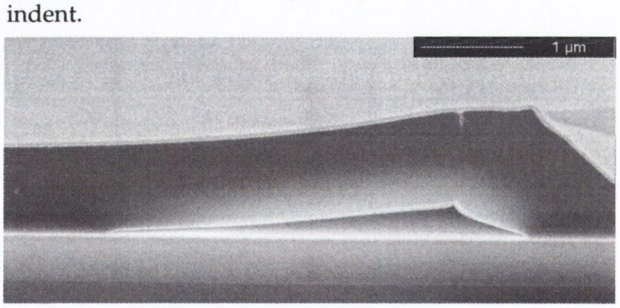

(c) A closer look at the delamination seen in figure 5.24(b) above.

Figure 5.24: Electron micrographs of delaminated and non-delaminated indents.

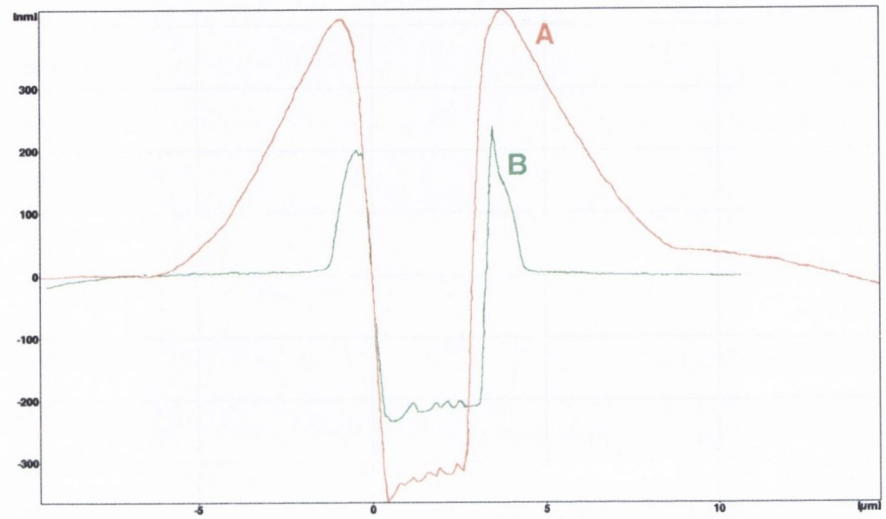

(a) Comparison of delaminated (A) and ordinary (B) indents.

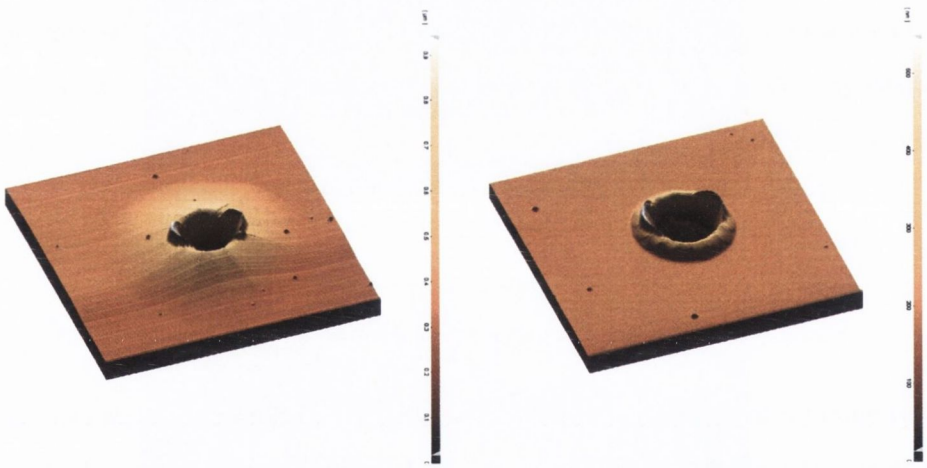

(b) Profile of delaminated indent.

(c) Profile of non-delaminated indent.

Figure 5.25: AFM measurements of delaminated indents.

The residual layer was shown to be dependent on stamp geometry and independent of the initial film thickness, maximum applied force and the time over which the force was applied. As well as proving futile in mass transport, high load application has been shown to result in non uniformities in the residual layer caused by elastic straining. Tests concerning variation of the punch size were performed resulting in a coinciding reduction of the residual layer with size. Tests on plane strain stamps suggest that the smallest local feature of a stamp also has a bearing on the residual height. Removal of lateral constraint through the initiation of delamination of the polymer film surrounding the stamp was shown to lower the yield stress of the system.

Chapter 6

Shear Injection Forming

Normal force generates both shearing and hydrostatic forces, of with shear driving plasticity [9, 64], as discussed in section 2.3.2. During normal loading, the production of shear strains results in plastic flow, however the extent of the flow is limited by friction [64] and the increase in shear strength of the material under the stamp. To compound the problem, attempting to increase shear stresses by increasing normal load in squeeze flow does not result in continued flow. Large forces are required to develop the required deviatoric stresses, these scale with the contact area of the stamp (as shown in figure 5.20) and can reach high levels when attempting to produce patterns over an entire wafer. There are a myriad of techniques to work around or avoid such problems, as summarised by Gates *et al.* [106] and Cross [12] and the efforts to exploit one of these techniques are discussed here. By maximising shearing stress, shear injection attempts to address the issues associated with NIL by driving plasticity in an efficient manner. This avoids the need for complex setups and exotic materials whilst reducing the need for high normal loads as discussed in Chapter 5.

An investigation into influencing the stresses in the system was carried out. Using the shear setup described in section 4.4, additional shear strains were induced using piezo elements in an attempt to drive plasticity whilst preventing the formation of hydrostatic volumes by avoiding high normal loads. This technique is referred to as SAOSF (Small Amplitude Oscillatory Shear Forming).

The shear injection process (summarised in figure 6.1) involved applying the stamp to the polymer film with a moderate normal load to maintain contact between the stamp and the film. The shear was applied in an oscillatory manner by the piezo transducers with a maximum amplitude of up to 200nm. The relative motion of the stamp and substrate was monitored by a laser vibrometer. Section 4.4 provides greater detail regarding the instrumentation and methods.

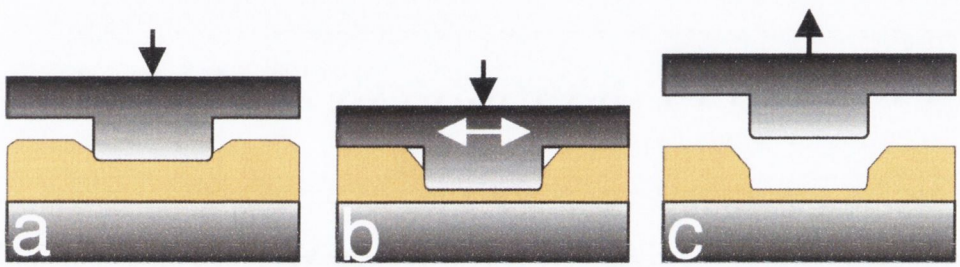

Figure 6.1: Summary of the shear injection process. A rigid punch is brought into contact with a ductile film under a normal load(a) and an oscillatory shearing motion is applied(b) before the separating the punch and thinned film(c).

6.1 Shear Strain Application During Squeeze Flow

Major considerations of the imprint process are the limits to improving the mask ratio (i.e. reducing the residual layer) and the elastic deformation of the stamp at high loads. As discussed in section 2.2.1, this is of importance when considering imprint for semiconductor and nanodevice fabrication processes.

A core requirement in nanoimprint lithography (also discussed in Section 1.1.2) is that sufficient material flows during the forming process to ensure high fidelity in the pattern transfer. A prominent problem with pattern transfer is that of the residual layer discussed in detail in (5.3). It has been shown (for cold forming processes) that high normal forces have a finite capability to reduce the amount of material under the stamp [6]. A principal problem with using large forces is elastic straining of the components involved [12, 7, 6, 107]. Not only does the straining have the potential to alter stamp and substrate geometry at peak load, but the phenomenon of "springback"

exists where elastic recovery on unloading adds to the distortion [108, 109]. The distortion reduces the pattern uniformity and fidelity where identical patterns imprinted by the stamp vary according to the location on the stamp. This can cause problems with post-imprint processes such as etching, deposition and polishing.

As mentioned previously in section 1.1.2, variations on NIL have been developed to avoid these problems [33, 34, 35, 36], but these in turn bring their own complications, as reviewed by Cross [12]. Section 2.5 describes mechanisms by which plasticity may occur in polymeric glasses. The Eyring model (section 2.5.2) supplies a mechanism by which mechanical forces may facilitate inelastic straining through the motion of polymer chain segments into free volume within the polymer matrix.

Higher temperatures can be used to increase material mobility, at the cost of increasing stamp-substrate adhesion and instrumentation complexity, limiting the scope of available materials. Active materials are temperature sensitive and may undergo degradation thus losing some of their desired properties. Forming at high temperatures means having to incorporate a warm-up/cool-down cycle [46], thus increasing cycle time and decreasing throughput. Lowering viscosity can be used as in the successful SFIL [38], but stamp-substrate adhesion and limits to the materials that can be crosslinked in such a manner are also restrictive.

The combination of hydrostatic pressure, mechanical constraint from surrounding material and elastic compliance of the silicon "hinterlands" of the stamp and substrate limit the production of shear stresses. Work from this project has shown that increasing the normal load only serves to deform the stamp and produces negligible gains as shown in section 5.3.2 [6].

6.1.1 Features and Characterisation of Applied Shear Strain

Initial experiments involved investigating system behaviour by applying a fixed normal load and waiting for a number of seconds for creep processes to settle down. Shear was then implemented by applying an AC voltage from a signal generator to an am-

plifier and to the piezo elements in turn, recording the subsequent excursions.

One of the first investigations undertaken was sweeping the shearing frequency by hand and watching the live indenter displacement trace. The output of the signal generator to a maximum of 10V was sufficient only to drive the PZT elements to 5nm strain, see figure 4.9 in section 4.4. It was noted that mechanical resonances of the nanoindenter were quite effective at boosting the limited piezo motion. One such resonance was 2717Hz, which was used for many tests. Another resonance was 613kHz, which provided a modicum of heating and proved very useful for inking the spheres before milling stamps, (section 4.1). However, due to phenomena such as ringing and chaotic behaviour these mechanical resonances were very difficult to interpret in light of trying to tie the shearing motion to extrusion. It was decided to utilise an amplifier to provide and exploit a low frequency away from any resonance, typically 500Hz for the majority of tests.

Figure 6.2 is a demonstration of the efficacy of shear application regarding extrusion of material under a stamp. The stamp was of a design to create plain-strain conditions being of 10μm in length and 1μm in width. The film into which the stamp was applied at a pressure of 50MPa was polystyrene of 950nm thickness. The shear amplitudes amounted to 1% and 2% of the stamp width. Without any increase of applied load, significant excursions into the film were observed with preservation of the stamp's shape.

Some key features of SAOSF are illustrated in figure 6.3. Preservation of high fidelity features is demonstrated in figure 6.3a-d. where inscribed lines of 60nm on a punch of diameter 2700nm (known as "B4") are replicated in the film despite the lateral motion of the stamp. The ability to drive complex flows is demonstrated using the stamp shown in figure6.3e. Enhanced filling of the serrations of the stamp are observed in figure 6.3g, compared to the example of normal load only in figure 6.3f. Figure 6.4 shows the effectiveness of SAOSF in reducing the residual layer from ~ 350nm to ~ 90nm, an aspect ratio increase from 7 to 30.

It should be noted that there is no correlation between the measurements made in

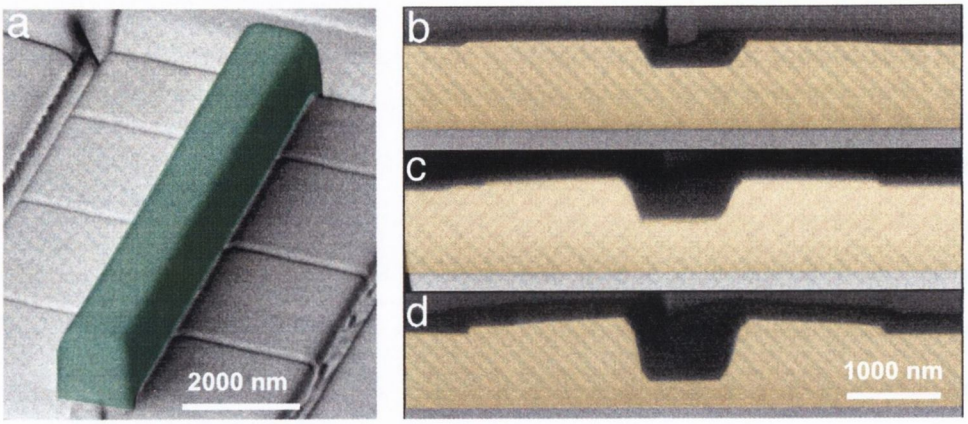

Figure 6.2: Demonstration of the affect of applied shear for a single plain-strain stamp (a). Electron micrographs of FIB cross sectioned indents show results for normal applied pressure of 50MPa with no shear (b), where only minor extrusion is observed. Applied oscillatory shear of amplitudes 10nm (c) and 20nm (d) orthogonal to the long axis of the stamp displays increased extrusion.

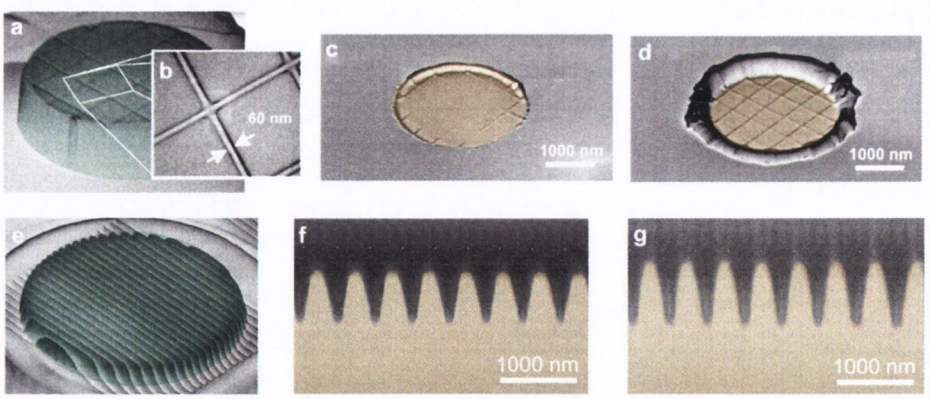

Figure 6.3: Resolution, parallelism, and high aspect ratio mass transport performance of SAOSF. The 60nm lines (b) decorating a cylindrical flat punch of 2700nm punch diameter (a), are barely visible under the 90 MPa normal load of (c) but are well reproduced after extensive shear forming into a glassy polystyrene film (d). In (g), filling into cavities between parallel, 500nm pitch line patterns on the die of (e) is enhanced over normal loading (f).

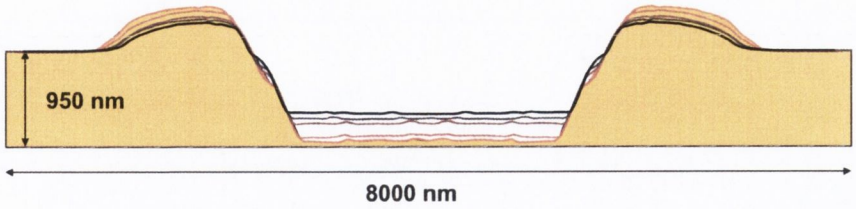

Figure 6.4: Significant long-range surface mass transport in solid polymer is shown in by the incremental residual layer thinning by SAOSF from an aspect ratio of 7 (black AFM scan profile, no shear) to 30 (red profile, 30nm shear amplitude)show no loss in thickness uniformity.

figure 6.4 and the tests represented by table 6.1 and subsequent figures. One major factor that may lead to such differences is drift of the indenter components which can be seen in many indenter measurements.

The series of graphs in figure 6.5, show typical shear behaviour for the cylindrical flat punch, in this case, "B4". The film was of 950nm thickness. Standard procedure was to increase the load to the desired level and maintain that load for the duration of the test. After waiting for creep processes to extinguish ($10 - 20$s) the shear would then be switched on for the remainder of the "hold time", typically a duration of $30 - 60$s. As can be seen, there is a correlation between the shear amplitude and maximum excursion. Table 6.1 summarises the results from figure 6.5. As can be seen, there is scope for improvement with the residual height in this set of tests as the maximum voltage of 400V (corresponding to a peak to peak displacement of 200nm) was not used.

Test No.	**Shear Amplitude** (nm_{pp})	**Residual Height** (nm)
1	0	466
7	0	459
2	50	442
6	75	438
3	100	324
4	125	291
5	150	275

Table 6.1: Details of shear excursions at 500Hz for stamp 2700nm diameter stamp "B4" at 2.5mN

It is clear from this data, figure 6.5(a), that there is a threshold that must be exceeded

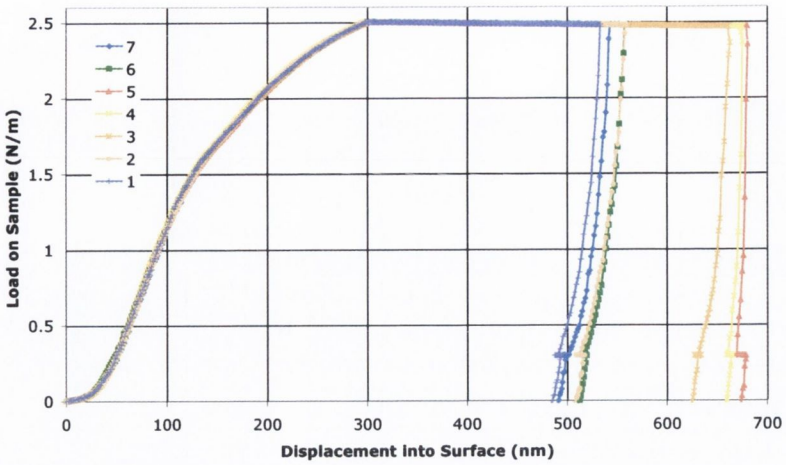

(a) Load on Sample vs. Displacement into Surface curve, showing shear excursion for events 3,5 &4.

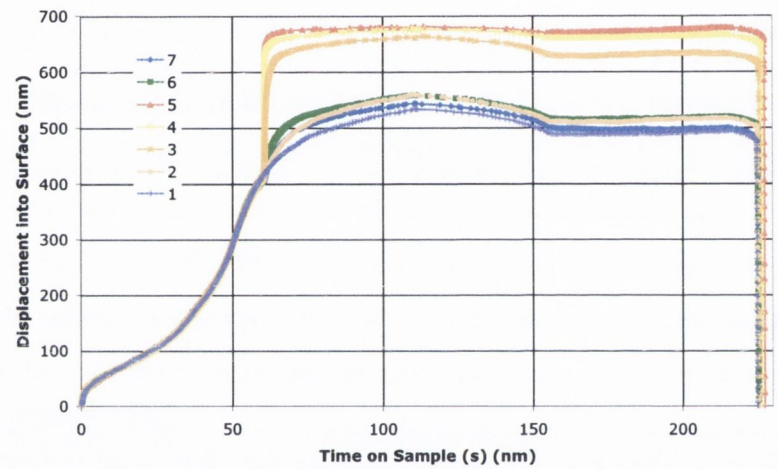

(b) Displacement into Surface vs.Time on Sample curve, showing rapid shear excursion at ~ 60s.

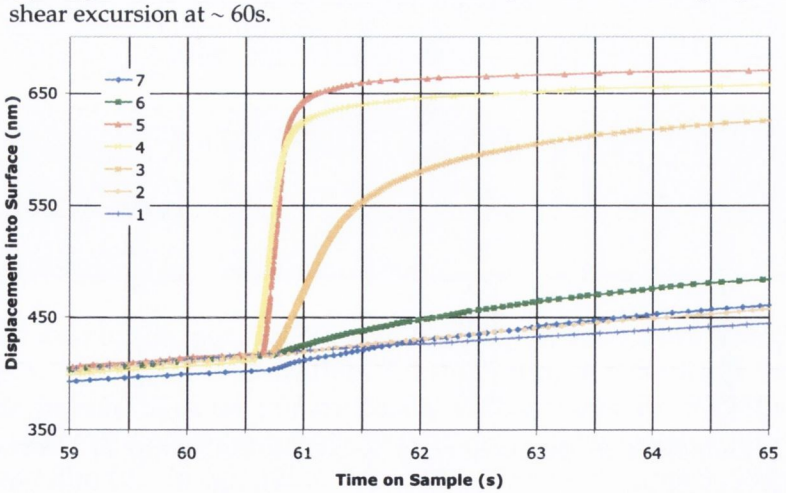

(c) Detail of figure 6.5(b) showing greater detail of the shearing event.

Figure 6.5: Displacement load and time data for a 2700nm diameter cylindrical flat punch for a series of voltages applied to the piezo transducers.

for the shearing action to work under these conditions, between 150V and 200V in this particular case, corresponding to a piezo motion of 50nm to 100nm (see figure 4.9). figure 6.5(b) shows the displacement into the sample over time. The moment at which the shear was switched on can be seen at 60s. Again the brevity of the shear excursion is evident. Although the shearing action continues for another 50s, it has no other apparent effects. The displacement due to shear typically lasts about 0.5s as shown in figure 6.5(c), meaning most of the work done happens in under 250 cycles. These tests did not utilise the full capabilities of the amplifier, where amplitudes upto 400V were possible. It would also appear that once the threshold is reached, the gains for further increases in amplitude are small, the reason for this is the compliance of the indenter shaft, as pointed out in the introduction to this chapter.

Measured velocities of the punch into the film exceeded 1μm/s indicating that the entire process is over quickly and happens within the first few shearing cycles. With only a 50nm residual height difference between tests 3 and 5 the velocity profiles differ, suggesting differing efficiencies of extrusion per cycle. This would suggest a fine level of control over the process is possible by variation of applied amplitude. By slowing down the shear oscillation frequency, direct observation of shearing cycles is possible (section 6.4.1).

6.2 Finite Element Analysis simulations of shear injection

To elucidate the detailed mechanism of SAOSF, finite element analysis (FEA) of a simple, ductile yield system under indentation plane strain was performed.

The plot of figure 6.6 shows contours of von Mises stress at a low normal indentation load of a one tooth die, where the Cauchy stress singularity points at the corners create small highly localized regions of material in a plastic state. The von Mises stress is the threshold deviatoric stress at which plastic yield occurs, (see section 2.3.2). In the simulation, the threshold is set at a value of 1, below which all strains are elas-

tic. Introducing a small shear displacement of 7% of the film thickness, we see that a plastic state (red contour) is introduced across the whole of the punch. By oscillating this shear in the simulation, the full SAOSF extrusion effect can be reproduced [1]. In conventional forming operations where high aspect ratio geometries present large, compressive contact areas, friction between die and billet leads to an exponentially rising "friction hill" and mean forming stress [64]. Lubricating interfacial layers provided by injecting liquid or by ultrasonic interfacial melting [71] attempt to mitigate this frictional effect.

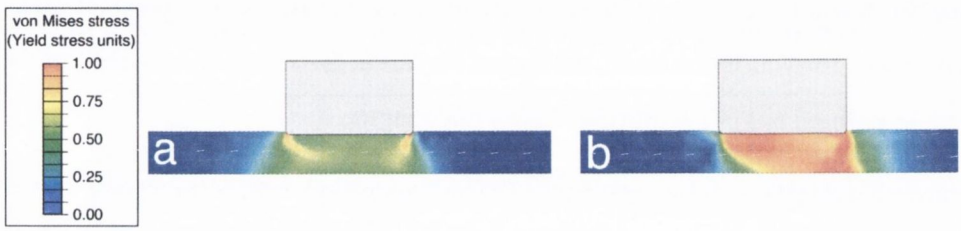

Figure 6.6: FEA of von Mises stress underneath a one tooth die. Under normal loading only (a), plasticity (red) is induced only at the corners of the punch. Application of shear (b) shows that the von Mises stress is introduced across the whole of the punch.

In figure 6.7 FEA suggests that extrusion due to SAOSF is not due to modification of boundary conditions or lubrication. A SAOSF simulation with full stick boundary conditions produces the strongest effect per cycle. Furthermore, simulation reveals the SAOSF action is thus more akin to pumping, relying on amplifying a small transport hysteresis by repetition. A circular flow pattern occurs about each Cauchy point (corner edge) of the stamp, synchronized to the shear oscillation.

The symmetry of this circulation is broken by the vertical punch side wall, causing a gradual migration of material to the pile-up region at the stamp sides. This is especially evident on the compressive side of the shear stroke shown in figure6.8c, where large vertical displacement vectors at the stamp edge reflect motion of material into a forming chip. SAOSF thus relies on structural ratcheting arising from contact induced, nonuniform stress distributions [30] and will operate regardless of any material ratch-

[1]More detail on the FEA can be obtained in the paper by Cross *et al.* [7] with supporting information and animations of simulations at http://pubs.acs.org.

eting that may accompany and enhance it.

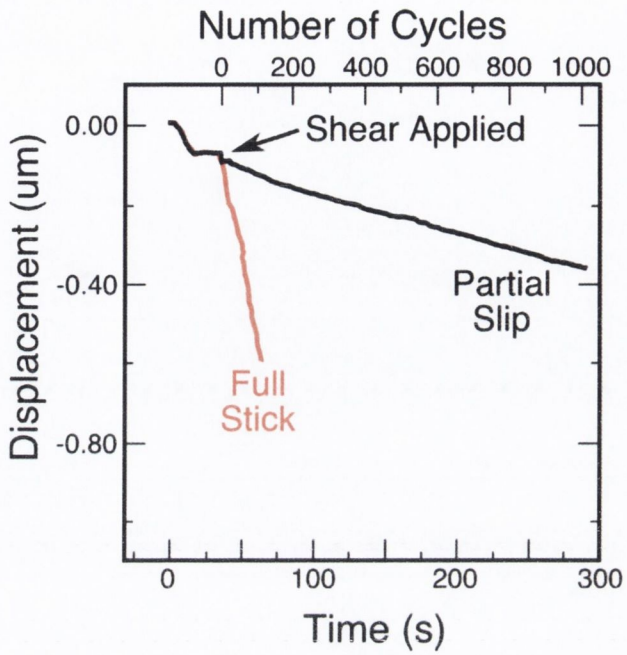

Figure 6.7: Results of variation of die-sample boundary conditions in FEA, where a change from full-stick to partial-slip friction conditions effect only the per-cycle rate of shear extrusion.

Figure 6.9 illustrates a key fidelity difference between simple normal loading and SAOSF. Plane strain experiments using a 600 nm by 6000 nm rectangular punch on a 150nm polystyrene film show excellent qualitative feature matching to the finite element simulations. Attempts to thin the film by applying a load of ~ 1.0GPa show that for both experiment (a) and simulation (b), a loss of residual layer uniformity occurs. This was shown to be due to elastic deformation of the die in chapter 5 [6]. In contrast, shear forming using a far lower normal load of 150MPa leads to an excellent uniformity with the same degree of thinning, (c) and (d). This uniformity is of crucial importance, for instance, to critical dimension (CD) yields produced during further lithographic processing steps [12, 69, 40] and to the thinning of insulating layers in field effect transistors.

Shear forming provides a way to overcome the limitations of die elastic deformation. These are more significant for large areas, since normal force scales with area, but die rigidity scales with diameter for features on a solid hinterland (chapter 5) [6].

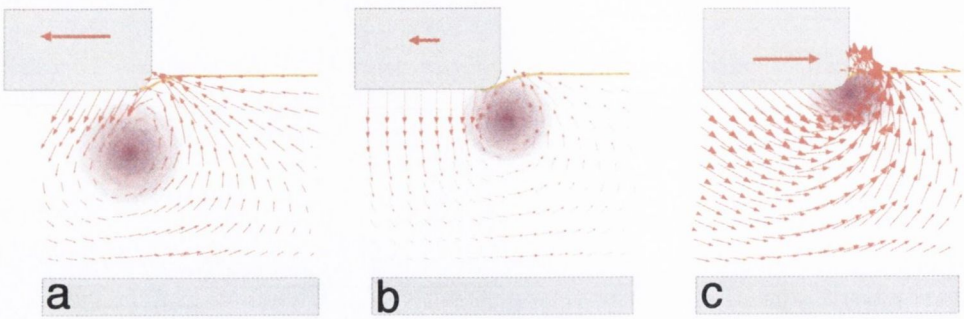

Figure 6.8: FEA of circulation at Cauchy points of a punch. The material displacement vector field at the right-hand corner of a stamp tooth is shown for left stroke (tensile) through right stroke (compressive) shear loading of the contact in parts (a - c). A region of material circulation (purple) moves up from slightly below the surface in part (a) to "break" against the stamp sidewall in part (c). For each cycle, the broken symmetry of this circulation results in a net pumping of material from beneath the tooth to the adjacent free-surface regions.

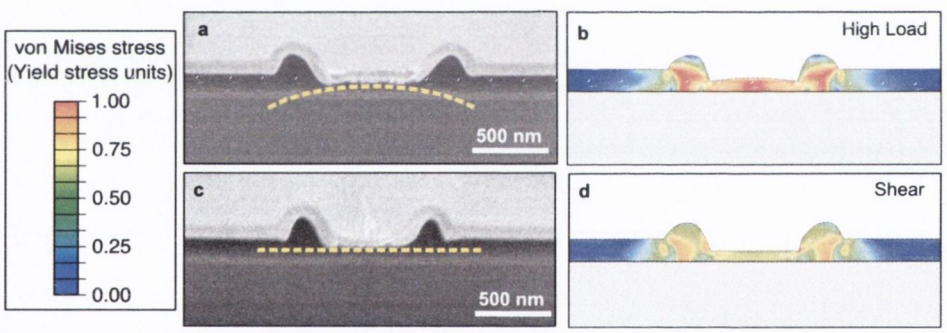

Figure 6.9: Avoidance of critical forming defects through shear forming, shown in experiment (a & d) and simulation (b & d). High loading pressure leads to a loss of residual layer uniformity, shown for 1 GPa in (a) and simulation in (b). Usage of the SAOSF technique under a low normal pressure (150 MPa) produces a flat residual layer in (c & d). This can be understood by the significantly lower degree of residual stress (partially shown here by von Mises stress contours derived from the simulations). Continued shear action thinning of the residual layer while retaining uniformity is easily achieved as shown in figure 6.3. The scanning electron micrographs of FIB-milled cross sections in (a, b) show the polymer as dark grey, with the deposited gold and platinum masking layers appearing as white/light grey. The supporting silicon substrate can be seen beneath the polymer with the boundary between the two appearing as a slightly lighter grey.

Nanoscale features of a dimension smaller or equivalent to the film thickness are by comparison relatively straightforward to form, it is multiscale flow arising from an initial distribution of features sizes and a cascade of progressively filled regions that provides the challenge.

6.3 Effects of state of stress on shearing

The state of stress of the material under the punch has effects on the results of shear injection. At different normal loads applied to the substrate, the material will naturally be in differing states of elastic and plastic strain. Figure 6.10 shows the loading curve of the cylindrical punch of with applied normal force only, with no shear application (see section 5.3). An attempt to measure the effects of shear under these differing stress states was made. A number of points along the curve were investigated as illustrated in figure 6.10, from majority elastic to plastic, through to the end of yield. The conditions for this experiment were similar to those described in Table 6.1.

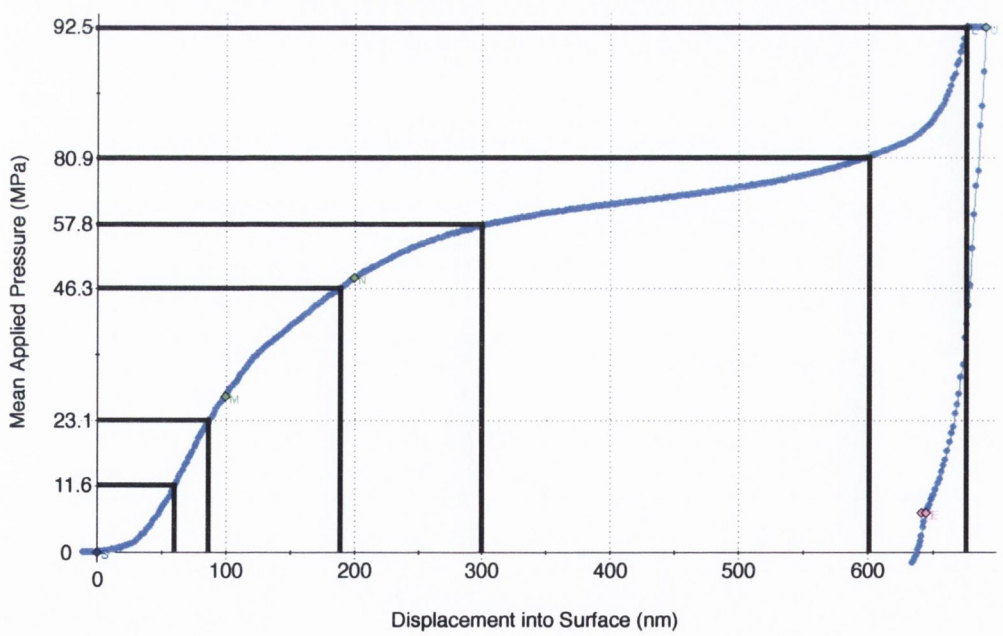

Figure 6.10: The flat punch signature for the a 2700nm diameter cylindrical flat punch, showing the applied normal pressure at which shear injection was made.

At 11.6MPa and 23.1MPa the polymer film about the stamp is mostly under elastic strain. This can be shown by the indenter's measurement of elastic recovery and AFM scans of the imprints which show minimal plasticity. At 46.3MPa and 57.8MPa, a significant component of plasticity is observed. The 80.9MPa point is where creating the required shear stresses to drive flow becomes increasingly difficult, as observed in section 5.3.2. At 92.5MPa, plastic strain has practically ceased and the system now loads elastically.

To investigate the effects of shear injection at each of these regimes described above, the punch was brought into contact with the film and loaded to the desired load for each test and held constant. After waiting for creep to extinguish , the shear was applied at a displacement of $175nm_{pp}$, corresponding to a voltage of $350V_{pp}$ with a frequency of 500Hz for ~ 50s, whereupon the punch was unloaded from the surface.

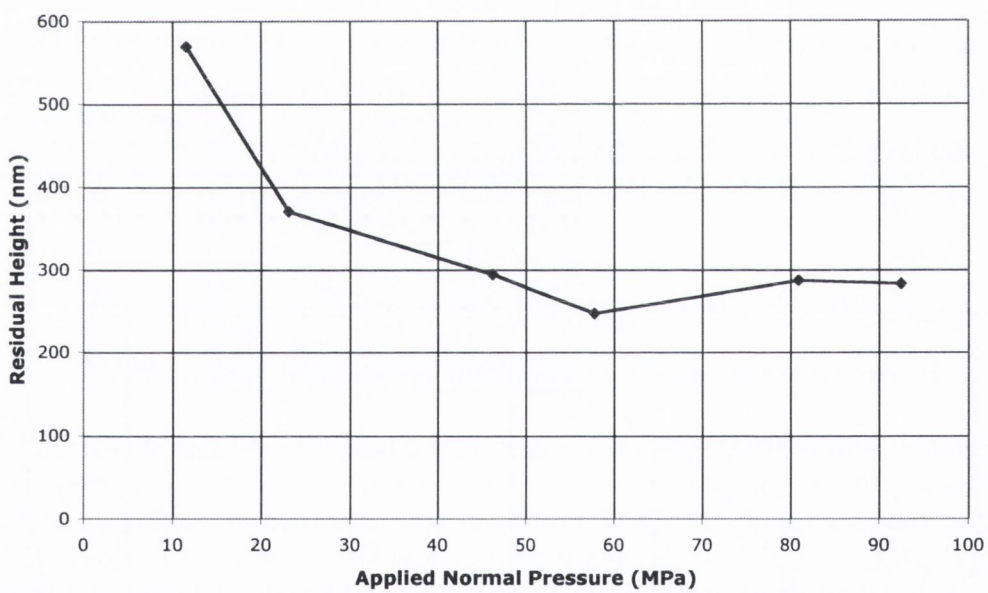

Figure 6.11: The residual film height for each value of peak loading pressure after shear injection.

Figure 6.11 presents the residual film height for each load after shearing and figure 6.12 presents the excursion due to shear application. The residual height h_r, described in section 5.3.2, is a way of measuring the performance of the process as an attempt to improve the mask ratio. The lower the residual height, the more material has been

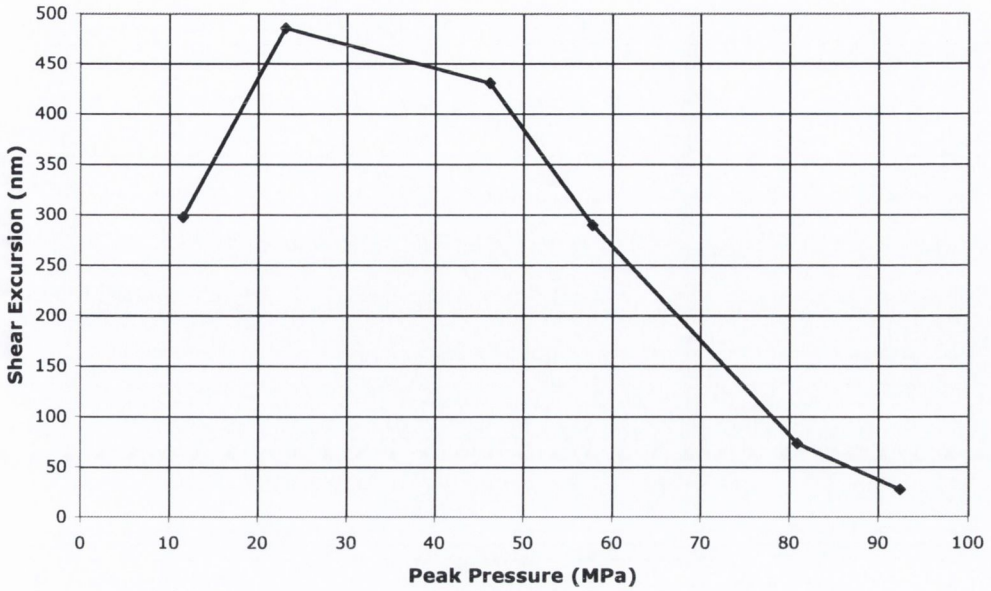

Figure 6.12: The excursion of the stamp into the surface for each value of peak loading pressure after shear injection.

extruded from underneath the punch. The shear excursion is a measurement of how far the stamp moved into the sample due to shear application only.

The best residual height achieved was for the 57.8MPa load, at this load the sample is in plastic yield zone for normal loading. It must be noted that in this setup, shear injection only manages an improvement of $<$ 50nm for h_r over high normal loading. It is notable that the the most work done by the shear application was at 23.1MPa with an excursion of $\sim$ 500nm, over half of the initial film thickness.

As already pointed out (5.3.2), use of high loads is can cause problems. Non-uniform elastic deformation of stamp and substrate and possibility of springback upon unloading are examples of undesirable outcomes. These experiments show that under this geometry, the largest gains are to be found by loading the stamp to a point close to the plastic turnover. Nonetheless, circumstances exist where such as multilayer geometries, where plastic flow in underlying structures is undesirable. Shear assisted forming means that large excursions can be made at reduced normal loads. This may be useful for stamps with large contact areas that require high loads to initiate forming.

6.4 Aspects of Applied Shear Strain

To attempt to determine the mechanism of mass transport by oscillatory shear application, a number of questions need to be addressed. The effects of frequency, amplitude and the number of cycles and the extent to which the effects can be controlled. The possible existence of heating and effects of shear direction with geometrical stamp asymmetries and how to continue to take advantage of all these phenomena.

6.4.1 Cycle Limitation, Shear Drive Modulation

It has been shown that there is a threshold amplitude at which mass transport due to shearing occurs. By modulating the voltage applied to the shear piezos it was hoped to resolve the behaviour.

Amplitude and frequency modulation functions were amplified and used to excite the shear piezos. As well as recording the vibrometer signal, the original excitation signal from the signal generator was recorded using the vibrometer data acquisition card. This ensured that the vibrometer signal could be tied to the excitation signal for analysis.

Low Frequency Shear

A study of frequency dependance, shearing at low frequencies ($<$ 50Hz) was performed. It was found that the shear driven mass transport still occurred.

A 3μm diameter circular flat punch was used with a 6%w/w polystyrene film of 524nm thickness. At 45 and 25Hz, the initial excursion was rapid, as seen at higher frequencies.

An example of a low frequency shearing event is shown in figure 6.13. The displacement into the sample is shown in green and the shear drive signal displayed in blue. At 0.1Hz and 200V, the individual cycles could clearly be seen in the displacement

data. The 30 cycle run (7 cycles of which of which are displayed in figure 6.13) resulted in a 472nm excursion and the 10 cycle resulted in a 272nm excursion. The motion of the stamp into the surface correlates with the maximum velocity of the shear motion, with the stamp displacement approximating the cosine function of the shear displacement.

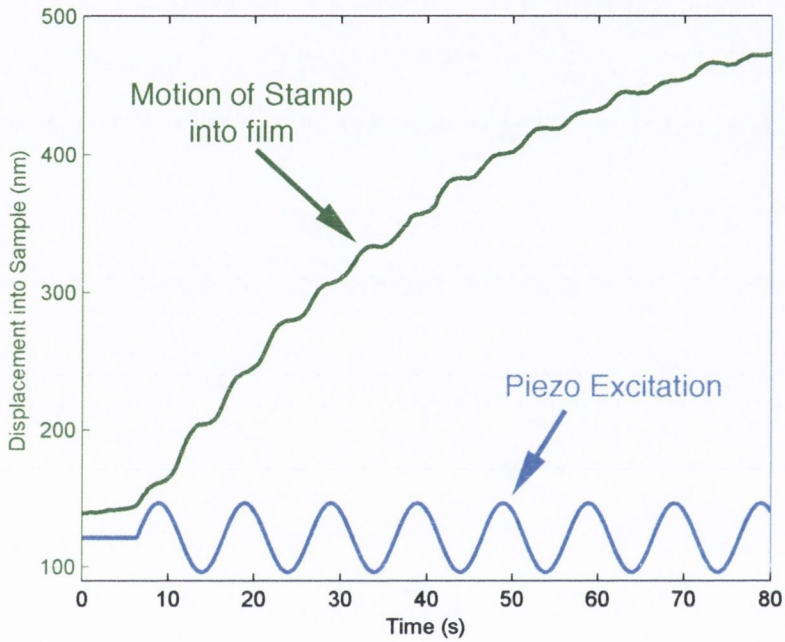

Figure 6.13: An example of a low frequency shearing at 0.1Hz showing the motion of the stamp into the film as measured by the nanoindenter and the piezo excitation voltage as measured by the vibrometer hardware.

These results support the observation of cycle limited mass transport (see section 6.5).

As mentioned above, the mechanical frequency response of the indenter and the electronic frequency response of the vibrometer prevented direct measurement of the stamp motion relative to the substrate. Regarding the indenter, a frequency below 5Hz is required to resolve the individual displacement due to each cycle. The filters of the vibrometer prevented measurement below $\approx$ 100Hz. Switching off the vibrometer high pass filter resulted in large drifts making low frequency data difficult to process. Attempts to perform offline signal processing on unfiltered vibrometer data

were unsuccessful due to time constraints preventing development of a suitable digital filter.

Modulation

The first experimental verification of shear forming used frequency sweeps to exploit mechanical resonances of the experimental setup (section 6.1.1). It was clear that although such resonances produced notable excursions into the films, the complexities introduced by the resonance made analysis difficult. Non-linearities were observed thus making correlation of shear motion.

One observed phenomenon was that of ringing. Ringing is observed when an impulse is introduced to a system. An example of ringing in our system is shown in figure 6.14 where the green plot represents the applied drive signal and the blue plot is the observed motion of stamp and substrate.

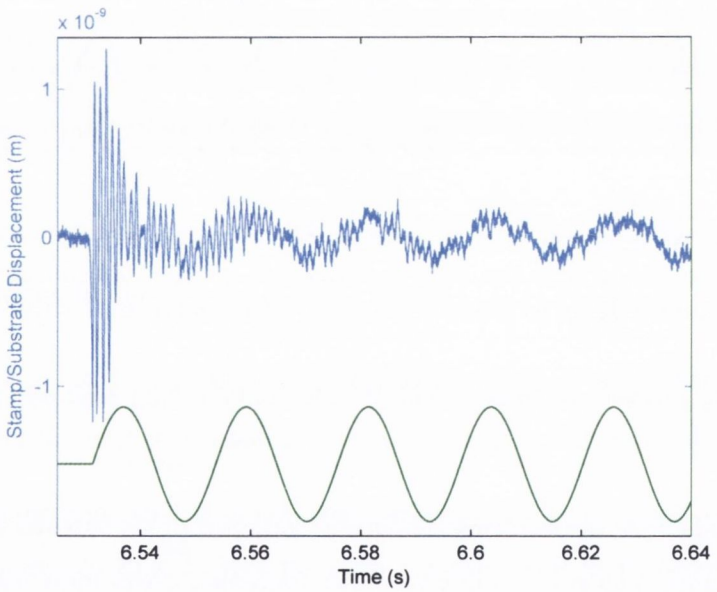

Figure 6.14: Observed mechanical ringing upon application of mechanical force. The applied drive signal is shown in green and the blue plot is the observed motion of stamp and substrate.

The drive signal is at 45Hz and the mechanical oscillation is at 931Hz. Although the 931Hz signal is extinguished within 4 cycles of the 45Hz signal and is of an insignifi-

cant amplitude by the end of the 1^{st} cycle, it is still an undesirable effect. It has been shown that the majority of shear driven forming occurs within the first few tens of cycles (one example is shown in figure 6.13) and here approximately 15 cycles are executed at 931Hz before dropping below the amplitude of the intended drive signal. Whilst ringing may in fact be an exploitable phenomenon in a manufacturing process, it complicates scientific analysis.

Modulation of the shear drive signal was investigated in order to see if ringing could be avoided. Ramping the amplitude of the drive signal was attempted, the results of which are shown in figure 6.15. Figure 6.15(a) shows the shear drive signal in blue and the measured relative motion between stamp and substrate. The amplitude is ramped from 0V to $2.5V_{pp}$ (resulting in an amplifier voltage of $250V_{pp}$ with a typical gain of 100) over a time of 45s, held at this voltage for 12.3s and ramped back down to 0V over 17s. These experiments were carried out with circular punches and rectangular plane strain stamps.

The measured stamp-substrate motion can be seen to increase with the drive signal until about 35s into the experiment when the slope of the stamp-substrate motion changes. At this point, an effect is seen in the displacement of the stamp into the sample (figure 6.15(b)). Up to this point, the stamp is experiencing a constant drift during the experiment, leading to a small, constant positive velocity, the change in this slope can be seen occurring about this 35s point where the stamp-substrate motion is $\sim 0.75nm_{pp}$. At the 39s point, a more obvious change is visible in the stamp-substrate motion and a definite increase in stamp velocity is observed. At 42s, a threshold is exceeded and a major excursion is observed.

Apart from the main conclusions that an amplitude threshold exists to activate the shear forming and ringing phenomena are avoided, other effects are also present. A couple of kinks are observed in the curve of the stamp displacement data during the main excursion. One reason for these kinks may be that a limited excursion may occur for a given amplitude and the continually increasing amplitude naturally continues to drive the excursion. The fact that the edges of the stamp result in high stress gradients,

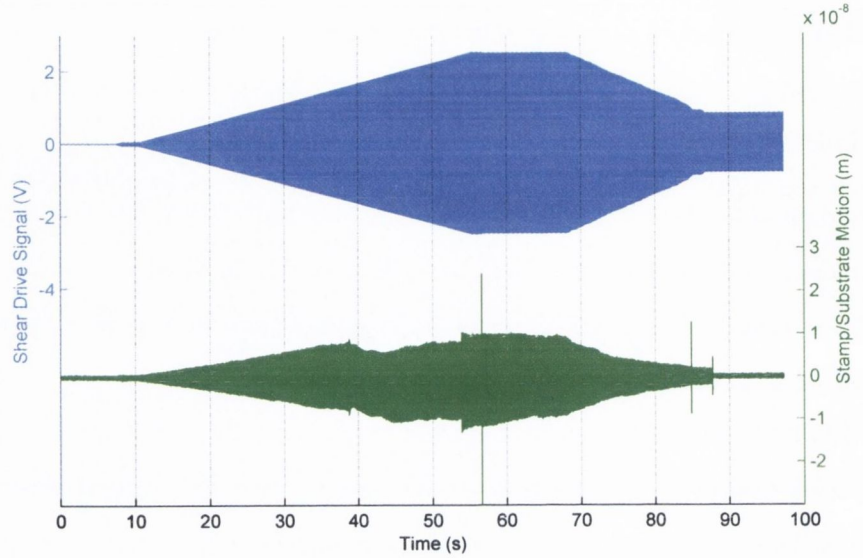

(a) Shear drive signal (blue) and measured stamp-substrate motion (green) during a ramping up of shear drive amplitude.

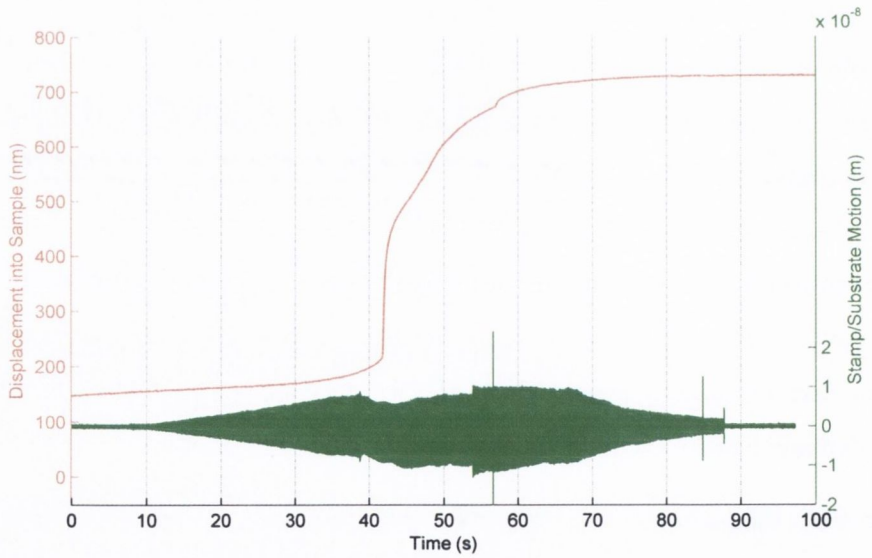

(b) Comparison of the displacement of the stamp into the sample (blue) and measured stamp-substrate motion (green) during a ramping up of the shear drive amplitude.

Figure 6.15: Effects of Amplitude Modulation of the drive signal.

may account for the initial small stamp excursion below the threshold point as plasticity is commonly observed at stamp edges prior to shearing. The small amount of additional stress provided by the shearing action below the threshold may be enough to drive further plasticity in these areas.

The envelope of the stamp-substrate motion appears to show a transition from elastic straining to driving plasticity. On closer examination of the data (figure 6.16), we can see differences between the two regimes. The blue plot being the shear drive signal and the green plot being the relative motion between stamp and substrate. In figure 6.16(a), a "kink" is introduced to the stamp-substrate motion after the 39s mark and is just about visible. At the 42s point, the main forming event occurs and the change in the stamp-substrate motion can be observed. It should be noted that the stamp-substrate behaviour does not "switch on" suddenly, but rather, is introduced and changes character slowly. The source and nature of this is unclear, although it may be due to mechanical resonance of the indenter or more subtle processes such as a per cycle transition between elastic loading and yielding. The increasing stiffness of the material under the stamp may be a factor in the changing behaviour [6](also, section 5.3.2). Closer analysis of these results in conjunction with modeling may reveal the details of the processes at work.

Investigations were carried out where the excitation frequency was modulated using a similar envelope to that used for the AM experiments. Using a rectangular plain strain stamp, figure 6.17 shows an example of the frequency modulation, a contiguous up-chirp and down-chirp was amplified and used to induce forming.

As seen in figure 6.17(a), the relative stamp-substrate motion drops to background noise levels at the highest drive frequencies. Figure 6.17(b) shows that this corresponds with a lull in the forming. The lack of stamp-substrate motion corresponds to frequencies of between 333Hz and 420Hz and occurred at all amplitudes large enough to induce forming. The reason for this behaviour is not clear and this apparently frequency dependent phenomenon is not observed in any other experiments (which were all single frequency).

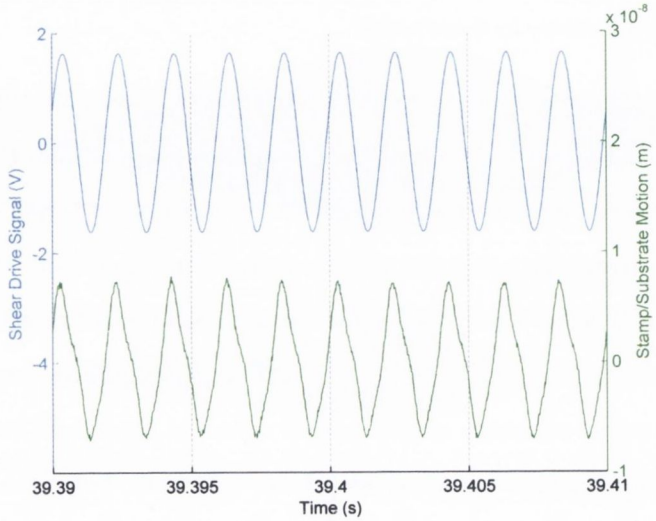

(a) Measurement of stamp-substrate motion and shear drive signal prior to exceeding forming threshold.

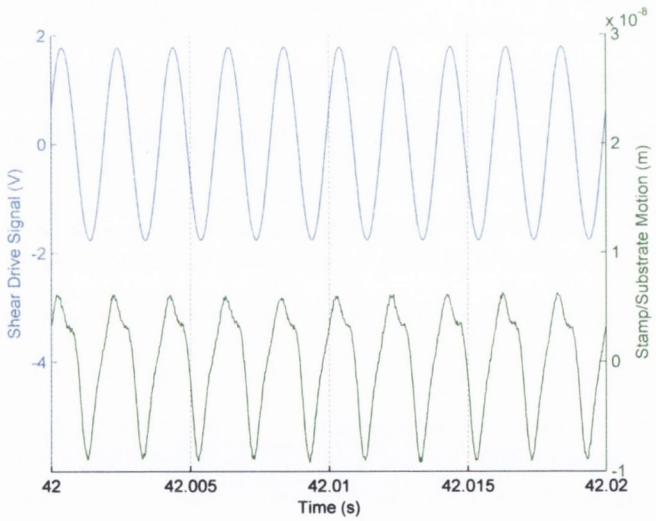

(b) Measurement of stamp-substrate motion and shear drive signal at forming threshold.

Figure 6.16: Comparison of stamp-substrate displacement before and after the forming threshold. Shear drive signal (blue) and measured stamp-substrate motion (green) during a ramping up of shear drive amplitude

One point to note is that the stamp-substrate motion shown in figure 6.17 was captured with the filters of the vibrometer turned off. This was one of the few incidences where the background drift was momentarily small enough to be discarded.

Isothermal operation

It was considered that localised heating may have led to a phase change of the polymer thus lowering the yield stress required. Although temperature measurement of the film locally was unachievable, heating effects were ruled out for a number of reasons. Friction as a heating source was ruled out as in the studies of frequency dependance and amplitude modulation 6.4.1, each individual cycle showed an excursion associated with mass transport. At low frequencies, any thermal energy generated through friction would quickly dissipate before a sufficient temperature was reached to cause a change in the polymer film. The fact that the excursions would start immediately on shear application would support this, as there is little time in which to accumulate energy. This frequency independence supports the reasoning that the mass transport is a purely mechanical phenomenon.

Typical ultrasonic welding processes operate in the regime of 20 to 40kHz [110, 111]. At frequencies above $>$ 100kHz, not only did the temperature of the piezo rise (figure 3.12), but the thermal expansion of the local system, (stamp-film-substrate) was noticed through the displacement measurement of the indenter as was expected . In these cases, behaviour was observed consistent with that of a material in and around T_g, such as high adhesion between polymer and stamp on unloading and material transfer onto the stamp. These features were absent in normal operation below 5kHz and typically 500Hz.

Shear Direction

The flat punch stamps were axisymmetric and so shear direction was not an issue. However, "real-world" applications rely on different geometries for success. The plane

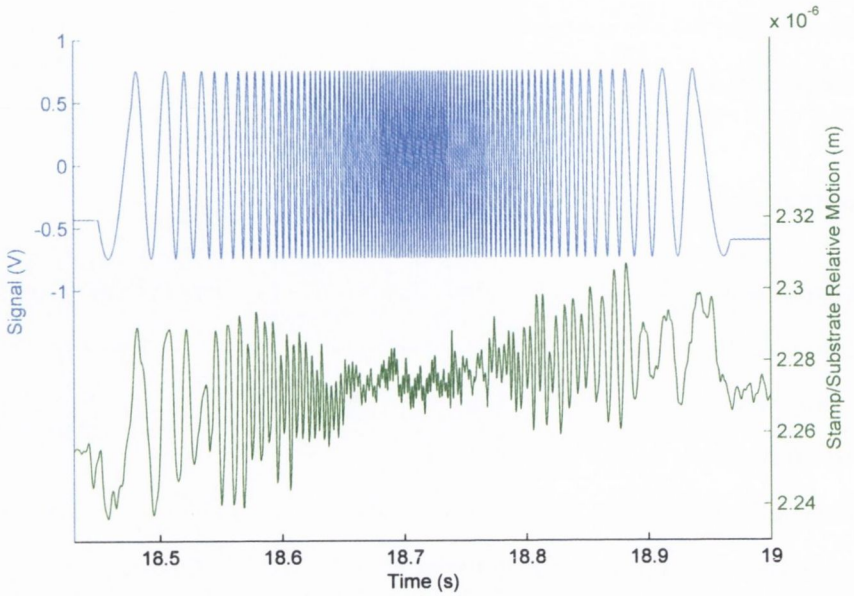

(a) Shear drive signal (blue) and measured stamp-substrate motion (green) displaying a decrease in the relative motion of stamp and substrate.

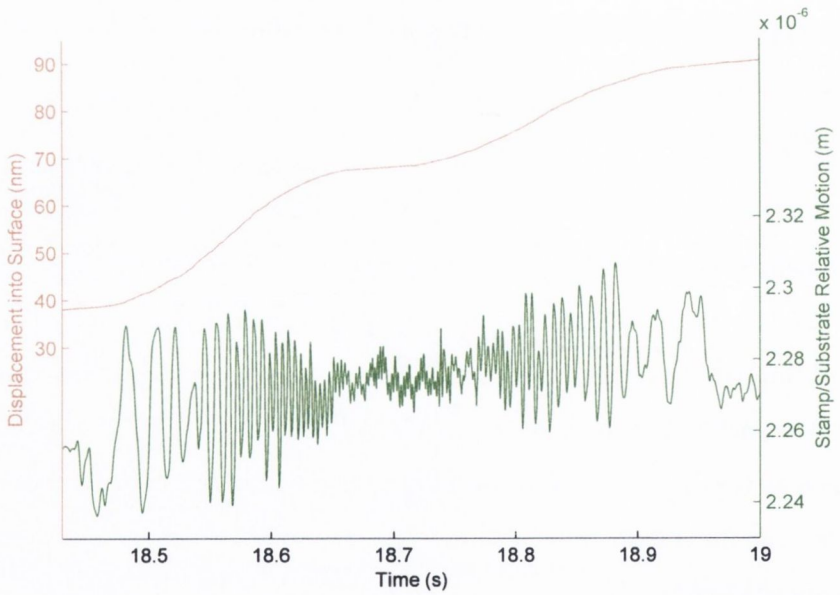

(b) The corresponding indenter data for displacement of the stamp into the surface (red) along with measured stamp-substrate motion (green) over time, again displaying a decrease in the relative motion of stamp and substrate.

Figure 6.17: Results of frequency modulation using a plane strain stamp where the reduction in stamp-substrate motion corresponds to frequencies of between 333Hz and 420Hz and occurred at all amplitudes large enough to induce forming.

strain stamps having one axis an order of magnitude greater than the other were used to investigate any differences in shear direction illustrated in figure 6.18. An iridium stamp with dimensions of 10μm × 1μm and a height of 1.15μm was used and the shearing directions were orthogonal and parallel to the longest axis. The film used was a 950nm thick polystyrene film.

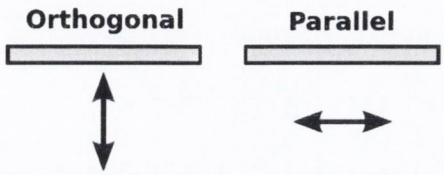

Figure 6.18: Illustration of the shearing motion with respect to the stamp.

Test	Shear (nm_{pp})	Δh (nm)	Orthogonal		Parallel	
			h_r(nm)	d_{vib} (nm)	h_r(nm)	d_{vib} (nm)
1	0	10	454	0	464	0
2	50	15	457	5	443	4
3	75	110	457	10	347	5
4	100	196	396	12	200	5

Table 6.2: Details of shear excursions at 500Hz for plane strain stamp Ir10 × 1 at 4mN with shear applied orthogonally and parallel to the longest axis.

Table 6.2 shows the results from this study. The load used was 4mN, a point just on the edge of the plastic turnover for this system, with an applied shear frequency of 500Hz. The Δh value is the difference in maximum depth between the different shearing directions, with h_r being the residual height. Representative values of stamp-substrate relative motion is given by d_{vib}, a sample of which can be seen in figure 6.19.

When dealing with complex geometries, the result of the isotropy (a maximum of 196nm) is significant and could certainly pose a problem when attempting to maximise performance. It is certainly possible to change the direction of shear, unfortunately this wasn't feasible to measure due to a single amplifier and measurement channel being available.

Vibrometer data is shown describing the difference between the parallel and orthogonal shearing directions. For the orthogonal motion experiment, the relative stamp-

substrate motion is ~ $12nm_{pp}$ whilst the the parallel motion results in ~ $5nm_{pp}$ relative motion for an applied voltage of 200V.

Notable points about the stamp-substrate motion are that of the phase difference between the excitation signal and the stamp motion, the amplitude and the shape of the motion waveform. The differences in the excursion is clear, the parallel shearing leads to the greatest effect. A possible reason for this behaviour is that the smaller profile presented in the parallel case provides a stress concentrator or a lower resistance to the motion necessary for mass transport through racheting.

The difference between the two with regards to the amplitude and the slip event could be explained by elastic straining of the stamp in the orthogonal case. The phenomena persist even after shearing has extinguished and any direct link of plasticity to the measured motion is not obvious. The observed event in figure 6.19(b) suggests elastic straining of the stamp combined with regular slip events. Indeed, the only orthogonal case that displayed a significant plastic excursion was test #4, (200V), and this was the only example where slip was observed.

It must be noted that there was a difference in background noise between the two samples, and that the noise is not a consequence of plasticity . The Parallel case had a background noise value of $1nm_{pp}$ which is visible in figure 6.19 and the orthogonal case had a value of $175pm_{pp}$.

6.5 Extinguishing of Shear induced Flow

The shearing process was cycle limited and frequency independent, with the majority of mass transport occurring in the first few tens of cycles. One of the problems encountered was the limitation of the extents of the mass transport. Although the shear application method offers improvements over the standard normal loading techniques, understanding the processes involved may lead to further improvements.

There are a number of effects that may contribute to the extinguishing of plastic flow

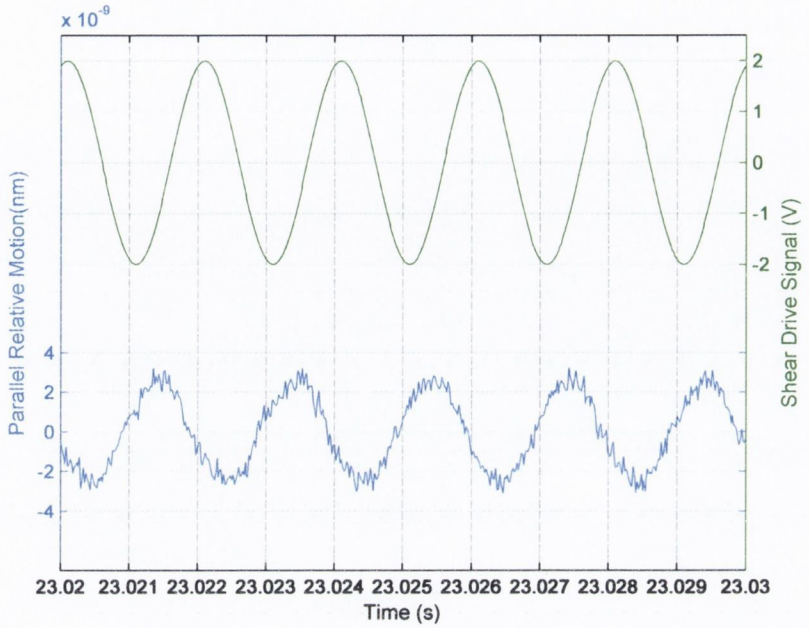

(a) Parallel Case, exhibiting ~ $5nm_{pp}$ relative motion

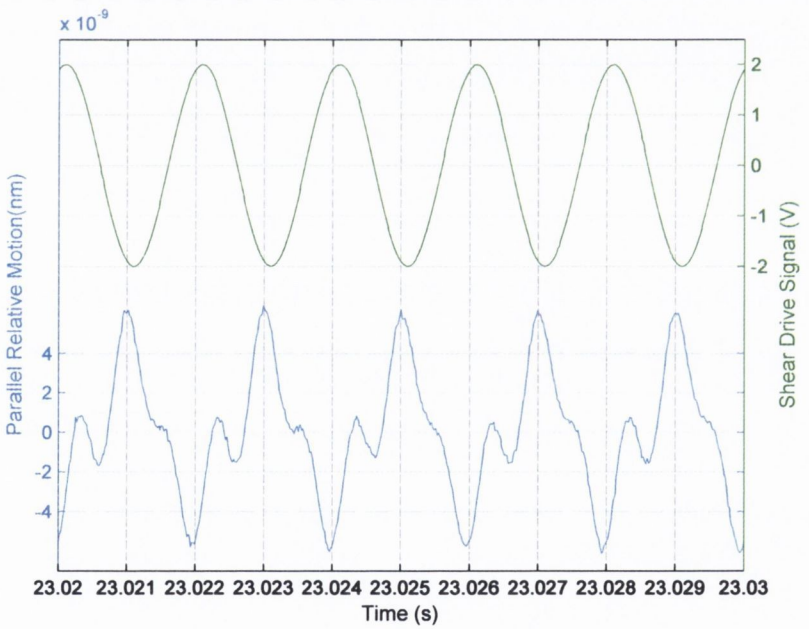

(b) Orthogonal case, ~ $12nm_{pp}$ relative motion

Figure 6.19: Differences in relative stamp-substrate motion for a rectangular plane-strain stamp driven with orthogonal shear directions.

in the geometries described here. Constraint from a surrounding film can have an effect (as discussed in section 2.4.1). Another factor preventing yield is friction which restricts the motion of material in contact with the stamp and substrate. In compressive strain, friction causes the yield stress to climb to a maximum at the centre of the stamp, this effect is known as a friction hill. This effect is sensitive to the ratio between a/h (where a is the contact radius and h is the film thickness) and the pressure required to drive plasticity climbs with the a/h ratio [64]. The effects of the friction hill can be seen in the elastic recovery of the coupon crushing experiments (section 5.3.1) [112, 113].

Friction can be a double edged sword, although it is capable of limiting extrusion under the stamp it may assist in the transfer of shear strain from the stamp to the film. Finite element modeling has produced results that suggest that a full stick condition results in more work being done per cycle than partial slip [7].

The limit to the plasticity is due to the mechanical properties of the equipment used for the experiment. The stiffness of the contact,after shear has extinguished, is greater than that of the indenter shaft and so the shaft absorbs the strain. Many tests were driven to the maximum amplifier voltage of $400V_{pp}$ resulting in a piezo displacement of $200nm_{pp}$ (section 4.4), yet the stamp-substrate displacement was typically measured to be on the order of $< 10nm$. As discussed in the above section on shear direction, the elastic straining of other components is also worthy of consideration.

Certain results have lead us to believe that shear driven plasticity may be capable of further reductions in the residual height. Certain considerations must be made regarding the design of the stamp and instrumentation so they are stiff enough to provide the required strains.

6.5.1 Conclusions

Combined with shearing, it was shown that high normal loads were counter-productive in reducing the residual layer. The best results were found by applying a load merely

high enough to initiate plastic yield. The mass transport mechanism was shown to be a non thermal process with evidence and modeling suggesting a ratcheting action being responsible. The process was shown to be frequency independent with a "switch-on" amplitude. Using a plane strain stamp with one axis an order of magnitude greater than the other, it was shown that the direction of shearing, relative to the stamp geometry is critical to the forming process.

SAOSF (Small Amplitude Oscillatory Shear Forming), a new solid processing technique, has been demonstrated under constant room temperature conditions for simple die shapes in thin, glassy polymer films. This displays an improvement over standard normal loading

Finite element simulation agrees well with experiment suggesting that the process is due to a combination of two effects. Uniformly plasticizing the entire area beneath where the die contacts the film and a novel pumping action involving die-geometry-induced broken circulation of elastoplastic flow. SAOSF is an isothermal process, free of temperature ramping times, thermal stresses, and adhesion problems during die removal, with material deformation localized to regions very close to the die. Nanometer dimension feature fidelity is preserved, and the process appears readily scalable from nanoscopic to 10's of micrometer dimensions. Crucially, the process is scale independent for thin film planar forming, since a critical shear strain is required. Reduced normal forging load largely eliminates elastic distortions, and the process appears relatively insensitive to die-film friction. The potential of SAOSF to activate transport in a wide choice of solid imprint materials may eventually extend to self-assembled nanomaterials which can accommodate plastic flow, furnishing a connection between "top-down" and "bottom-up" patterning techniques.

Chapter 7

Conclusion

Nanotechnology refers to devices comprising of features whose dimensions are measured in nanometers[1]. The most obvious (and ubiquitous) example of nanotechnology is the modern integrated circuit. At the time of writing, a modern computer processor contains features as small as 65nm. There are many methods of producing features and devices on the nanoscale, one of the newer methods is known as nanoimprint lithography (NIL).

Nanoimprint is a technique that involves mechanical patterning using a rigid patterned stamp on a deformable thin film to produce nanostructures. It is also a technique that is the focus of much research because of the benefits it brings over other nanofabrication methods. It is a planar process potentially capable of producing high resolution features at a high throughput and low cost and has been shown to reliably produce features smaller than 25nm since it's inception in 1995 [1] and features below 10nm since 1997 [2].

NIL has shown great flexibility with diverse production of of devices featuring passive and active features. Examples such as optical filters, photonic crystals, microfluidics, active electronics, SAW filters and electrodes for single molecule transistors to name a selection. However, because it is a mechanical processes, several unique issues with

[1] *i.e.* smaller than a micrometer, *i.e.* not over 1000nm

NIL exist, for example, adhesion between stamp and mold, pattern uniformity and residual material. These issues must be addressed if NIL is to assume the place of more traditional fabrication methods.

This project attempted to address some of these issues and obtain solutions using the approach of instrumented indentation on single feature stamps. With this approach it was possible to precisely isolate, control and measure the stresses and strains of the material during and after the imprint event [3] [4] [5].

7.1 Conclusions

Localised characterisation of polymer properties after imprint

Using the high sensitivity of the nanoindenter, measurements were carried out to determine the mechanical state of features created by wide area hot embossing of polystyrene [5] (section5.2). Highly localised testing of individual features using a Berkovich tip were performed. It was found that there were differences in hardness and elastic modulus between the pristine and extruded polymer. This however was not because of any change in the polymer itself, but rather due to the lack of constraint from surrounding polymer in extruded sections. It was also noted that the influence of the silicon substrate supporting the film was significant and affected the measurements on thiner parts of the film preventing true measurements being obtained. Global testing using a silicon sphere of 1mm was carried out, crushing the embossed lines. As the lines were crushed, the properties were found to be convergent on those of the pristine film. This reinforced the conclusion that the polystyrene had not been altered by strain hardening during embossing.

Influences of elastic strains in glassy polymer imprint

An investigation into the phenomenon of residual layers of unextruded material was carried out [6](section5.3.2). A cylindrical flat punch made of silicon was created in the

FIB and imprinted into a series of PVAc films of different thicknesses. All the films displayed characteristics common to the flat punch geometry. Although yield occurred at an applied pressure of 260GPa, the pressure was increased beyond that by at least a factor of 5. The thickness of the unextruded layer was found to be dependent only on the stamp geometry and independent of applied load, stamping time and initial film thickness. As the film thins, the yield stress for the film rises beyond the shear stress provided by the stamp. The increasing load would develop large hydrostatic stresses. Analysis of the the stiffnesses of the system (stamp, polymer and substrate) reveals that the thinned polymer film is likely to be significantly high than the rest of the system. With the conclusion that continuing to increase the applied load was seen to have little effect on the film and served to only deform the stamp and substrate.

Mechanical thinning of solid films through shear injection

With the futility of applying enormous loads to drive plasticity being made clear, an attempt to introduce plasticity by maximising shear and minimising hydrostatic pressure was attempted [7](section 6). It was possible to develop a novel processing technique for thin solid polymer films. This technique, known as Small Amplitude Oscillation Shear Forming (SAOSF) activates material transport in a more efficient manner than normal loading alone. Finite element analysis provides possible mechanisms for this effect. By introducing a small oscillatory shear strain, friction between the stamp and substrate transmits the strain to the area under the stamp driving plasticity. This shear strain also causes ratcheting of material out from under the stamp at the corners

.

SAOSF is an isothermal process with many benefits. It is free of temperature ramping times, thermal stresses, and adhesion problems during die removal. It can drive complex flows, with material deformation localized to regions very close to the die. Elastic distortions are largely eliminated and although the technique appear insensitive to stamp-film friction, although full stick conditions results in more a greater quantity of plasticity per cycle. Finally, as the process is dependent on strain to drive

the process, scaling to large contact areas is feasible.

7.2 Future Work

In the voyage of discovery that was this project, many ideas had to be left by the wayside for various reasons, whether they be time constraints or instrumentation inadequacies or simply not recognising a good result when you see it. This section attempts to touch on some of the work that could be done in the future.

A great many stamps were destroyed by myriad reasons, the move from silicon stamps to diamond may have prevented some work from being lost. One of the ways in which a few stamps met their end was via high voltage discharge from the piezo transducers. Not long before I finished experimental work, this was simply fixed by changing the wiring layout of the piezo stack so the piezo in contact with the substrate was grounded.

Custom instrumentation may have to be constructed in order to continue investigations. Due to the low lateral stiffness of the indenter shaft this tended to absorb the strains imposed by the shear piezos. Another point regarding the instrumentation was the frequency responses of the vibrometer and nanoindenter. The indenter was adept at low frequency work whilst the vibrometer was adept at high frequency work. The two did not overlap and so it was difficult to obtain data about individual shear cycles. The simplest solution would be to exploit the enormous dynamic range of the vibrometer and implement an offline digital "brick wall" filter to remove the background drift thus providing single cycle resolution for the shearing process. This was attempted, but ultimately proved futile due to time constraints.

FEA suggests that boundary conditions, namely friction, have little effect on the ultimate results for shear forming. However, the full stick condition tends to improve the efficiency, requiring fewer cycles to achieve a goal. Where this may come in interesting is in multilayer forming, where preservation of features in lower layers is critical. As multilayer geometries are commonplace in semiconductor manufacturing, optics

and microfluidics, it would be interesting to see if the results of this project had any application in the area.

Bibliography

[1] S. Y. Chou, P. R. Krauss, and P. J. Renstrom. Imprint of sub-25 nm vias and trenches in polymers. *APPLIED PHYSICS LETTERS*, 67(21):3114–3116, Nov 1995.

[2] S. Y. Chou and P. R. Krauss. Imprint lithography with sub-10 nm feature size and high throughput. *MICROELECTRONIC ENGINEERING*, 35(1-4):237–240, Feb 1997.

[3] G. L. W. Cross, R. A. Langford, B. S. O'Connell, and J. B. Pethica. The mechanics of nanoimprint forming. *FUNDAMENTALS OF NANOINDENTATION AND NANOTRIBOLOGY III*, 841:15–26, 2005.

[4] G. L. W. Cross, B. S. O'Connell, J. B. Pethica, and W. C. Oliver. Some issues in the mechanical forming of nanoimprint structures. *JOURNAL OF PHOTOPOLYMER SCIENCE AND TECHNOLOGY*, 18(5):559–562, 2005.

[5] G. L. W. Cross, B. S. O'Connell, J. B. Pethica, H. Schulz, and H. C. Scheer. Instrumented indentation testing for local characterisation of polymer properties after nanoimprint. *MICROELECTRONIC ENGINEERING*, 78-79:618–624, Mar 2005.

[6] G. L. W. Cross, B. S. O'Connell, and J. B. Pethica. Influence of elastic strains on the mask ratio in glassy polymer nanoimprint. *APPLIED PHYSICS LETTERS*, 86(8):081902, Feb 2005.

[7] G. L. W. Cross, B. S. O'Connell, H. O. Ozer, and J. B. Pethica. Room temperature mechanical thinning and imprinting of solid films. *NANO LETTERS*, 7(2):357–362, Feb 2007.

[8] G. L. W. Cross, B. S. O. Connell, J. B. Pethica, H. Rowland, and W. P. King. Variable temperature thin film indentation with a flat punch. *REVIEW OF SCIENTIFIC INSTRUMENTS*, 79, 2008.

[9] K. L. Johnson. *Contact Mechanics*. Cambridge University Press, 2003.

[10] R. HIll. *The mathematical theory of plasticity*. Oxford, 1950.

[11] D. Tabor. *The Hardness of Metals*. Oxford University Press, 1951.

[12] G. L. W. Cross. The production of nanostructures by mechanical forming. *JOURNAL OF PHYSICS D-APPLIED PHYSICS*, 39(20):R363–R386, Oct 2006.

[13] IBM. "ibm power6 microprocessor specification". Technical report, IBM, 2007.

[14] L. J. Guo. Nanoimprint lithography: Methods and material requirements, 2007.

[15] Intel. Intel museum webpage, 2007.

[16] Itrs website. http://www.itrs.net/, 2007.

[17] S. Y. Chou, P. R. Krauss, and P. J. Renstrom. Nanoimprint lithography. *JOURNAL OF VACUUM SCIENCE & TECHNOLOGY B*, 14(6):4129–4133, Nov-Dec 1996.

[18] G. M. Whitesides, B. Gates, Q. Xu, R. Boulatov, C. Love, and D. B. Wolfe. New approaches to nanofabrication. *ABSTRACTS OF PAPERS OF THE AMERICAN CHEMICAL SOCIETY*, 227:U514–U514, Mar 2004.

[19] M. Otto, M. Bender, J. Zhang, A. Fuchs, T. Wahlbrink, J. Bolten, B. Spangenberg, and H. Kurz. Dimensional stability in step & repeat uv-nanoimprint lithography. *MICROELECTRONIC ENGINEERING*, 84(5-8):980–983, May-Aug 2007.

[20] ITRS. International technology roadmap for semiconductors: Lithography report - 2006 update. Technical report, ITRS, 2006.

[21] L. J. Guo. Recent progress in nanoimprint technology and its applications, 2004.

[22] C. Burda, X. B. Chen, R. Narayanan, and M. A. El-Sayed. Chemistry and properties of nanocrystals of different shapes. *CHEMICAL REVIEWS*, 105:1025–1102, 2005.

[23] B. A. Grzybowski and G. M. Whitesides. Dynamic aggregation of chiral spinners. *SCIENCE*, 296(5568):718–721, 2002.

[24] C. R. K. Marrian and D. M. Tennant. Nanofabrication. *JOURNAL OF VACUUM SCIENCE & TECHNOLOGY A*, 21(5):S207–S215, Sep-Oct 2003.

[25] S. A. Stauth and B. A. Parviz. Self-assembled single-crystal silicon circuits on plastic. *PROCEEDINGS OF THE NATIONAL ACADEMY OF SCIENCES OF THE UNITED STATES OF AMERICA*, 103(38):13922–13927, 2006.

[26] A. J. Heinrich, C. P. Lutz, J. A. Gupta, and D. M. Eigler. Molecule cascades. *SCIENCE*, 298(5597):1381–1387, Nov 2002.

[27] L. Ressier, J. Grisolia, C. Martin, J. P. Peyrade, B. Viallet, and C. Vieu. Fabrication of planar cobalt electrodes separated by a sub-10 nm gap using high resolution electron beam lithography with negative pmma. *ULTRAMICROSCOPY*, 107(10-11):985–988, Oct 2007.

[28] F. Hua, Y. G. Sun, A. Gaur, M. A. Meitl, L. Bilhaut, L. Rotkina, J. F. Wang, P. Geil, M. Shim, J. A. Rogers, and A. Shim. Polymer imprint lithography with molecular-scale resolution. *NANO LETTERS*, 4(12):2467–2471, 2004.

[29] J. Taniguchi, Y. Tokano, I. Miyamoto, M. Komuro, and H. Hiroshima. Diamond nanoimprint lithography. *NANOTECHNOLOGY*, 13(5):592–596, 2002.

[30] M. Colburn, S. Johnson, M. Stewart, S. Damle, T. Bailey, B. Choi, M. Wedlake, T. Michaelson, S. V. Sreenivasan, J. Ekerdt, and C. G. Willson. Step and flash imprint lithography: A new approach to high-resolution patterning. *EMERGING LITHOGRAPHIC TECHNOLOGIES III, PTS 1 AND 2*, 3676:379–389, 1999.

[31] L. J. Heyderman, H. Schift, C. David, B. Ketterer, M. Auf der Maur, and J. Gobrecht. Nanofabrication using hot embossing lithography and electroforming. *MICROELECTRONIC ENGINEERING*, 57-8:375–380, 2001.

[32] G. M. Schmid, M. D. Stewart, J. Wetzel, F. Palmieri, J. J. Hao, Y. Nishimura, K. Jen, E. K. Kim, D. J. Resnick, J. A. Liddle, and C. G. Willson. Implementation

of an imprint damascene process for interconnect fabrication. *JOURNAL OF VACUUM SCIENCE & TECHNOLOGY B*, 24(3):1283–1291, May-Jun 2006.

[33] H. Schulz, D. Lyebyedyev, H. C. Scheer, K. Pfeiffer, G. Bleidiessel, G. Grutzner, and J. Ahopelto. Master replication into thermosetting polymers for nanoimprinting. *JOURNAL OF VACUUM SCIENCE & TECHNOLOGY B*, 18(6):3582–3585, 2000.

[34] A. KUMAR and G. M. WHITESIDES. Features of gold having micrometer to centimeter dimensions can be formed through a combination of stamping with an elastomeric stamp and an alkanethiol ink followed by chemical etching. *APPLIED PHYSICS LETTERS*, 63(14):2002–2004, 1993.

[35] S. Y. Chou, C. Keimel, and J. Gu. Ultrafast and direct imprint of nanostructures in silicon, 2002.

[36] P. Ruchhoeft, M. Colburn, B. Choi, H. Nounu, S. Johnson, T. Bailey, S. Damle, M. Stewart, J. Ekerdt, S. V. Sreenivasan, J. C. Wolfe, and C. G. Willson. Patterning curved surfaces: Template generation by ion beam proximity lithography and relief transfer by step and flash imprint lithography, 1999.

[37] M. D. Stewart, S. C. Johnson, S. V. Sreenivasan, D. J. Resnick, and C. G. Willson. Nanofabrication with step and flash imprint lithography. *JOURNAL OF MICROLITHOGRAPHY MICROFABRICATION AND MICROSYSTEMS*, 4(1):011002, Jan-Mar 2005.

[38] D. J. Resnick, G. Schmid, M. Miller, G. Doyle, C. Jones, and D. LaBrake. High-volume full-wafer step-and-flash imprint lithography. *SOLID STATE TECHNOLOGY*, 50(2):39–+, Feb 2007.

[39] Micro resist technology website. http://www.microresist.de/.

[40] H. Schulz, M. Wissen, N. Bogdanski, H. C. Scheer, K. Mattes, and C. Friedrich. Impact of molecular weight of polymers and shear rate effects for nanoimprint lithography. *MICROELECTRONIC ENGINEERING*, 83(2):259–280, Feb 2006.

[41] N. H. Li, W. Wu, and S. Y. Chou. Sub-20-nm alignment in nanoimprint lithography using moire fringe. *NANO LETTERS*, 6(11):2626–2629, 2006.

[42] Christopher W. Macosko. *Rheology: principles, measurements, and applications.* Wiley-VCH, 1993.

[43] H. D. Rowland and W. P. King. Polymer deformation and filling modes during microembossing. *JOURNAL OF MICROMECHANICS AND MICROENGINEERING*, 14(12):1625–1632, 2004.

[44] H. D. Rowland, A. C. Sun, P. R. Schunk, and W. P. King. Impact of polymer film thickness and cavity size on polymer flow during embossing: toward process design rules for nanoimprint lithography. *JOURNAL OF MICROMECHANICS AND MICROENGINEERING*, 15(12):2414–2425, Dec 2005.

[45] H. J. MAMIN and D. RUGAR. Thermomechanical writing with an atomic force microscope tip. *APPLIED PHYSICS LETTERS*, 61(8):1003–1005, 1992.

[46] L. J. Heyderman, H. Schift, C. David, J. Gobrecht, and T. Schweizer. Flow behaviour of thin polymer films used for hot embossing lithography. *MICROELECTRONIC ENGINEERING*, 54(3-4):229–245, Dec 2000.

[47] H. C. Scheer and H. Schulz. A contribution to the flow behaviour of thin polymer films during hot embossing lithography. *MICROELECTRONIC ENGINEERING*, 56(3-4):311–332, 2001.

[48] D. Y. Khang, H. Yoon, and H. H. Lee. Room-temperature imprint lithography. *ADVANCED MATERIALS*, 13(10):749–752, May 2001.

[49] E. Mele, A. Camposeo, R. Stabile, P. Del Carro, F. Di Benedetto, L. Persano, R. Cingolani, and D. Pisignano. Polymeric distributed feedback lasers by room-temperature nanoimprint lithography. *APPLIED PHYSICS LETTERS*, 89(13), 2006.

[50] P. Sharma, N. Kaushik, H. Kimura, Y. Saotome, and A. Inoue. Nano-fabrication with metallic glass - an exotic material for nano-electromechanical systems. *NANOTECHNOLOGY*, 18(3), 2007.

[51] R.N. Haward, editor. *The Physics of Glassy Polymers*. Applied Science, 1973.

[52] H. Sofuoglu and J. Rasty. On the measurement of friction coefficient utilizing the ring compression test. *TRIBOLOGY INTERNATIONAL*, 32(6):327–335, 1999.

[53] J. Engmann, C. Servais, and A. S. Burbidge. Squeeze flow theory and applications to rheometry: A review. *JOURNAL OF NON-NEWTONIAN FLUID MECHANICS*, 132(1-3):1–27, 2005.

[54] H. J. Lee, H. W. Ro, C. L. Soles, R. L. Jones, E. K. Lin, W. L. Wu, and D. R. Hines. Effect of initial resist thickness on residual layer thickness of nanoimprinted structures. *JOURNAL OF VACUUM SCIENCE & TECHNOLOGY B*, 23(6):3023–3027, 2005.

[55] Y. Hirai, S. Yoshida, and N. Takagi. Defect analysis in thermal nanoimprint lithography. *JOURNAL OF VACUUM SCIENCE & TECHNOLOGY B*, 21(6):2765–2770, 2003.

[56] G. Y. Jung, Z. Y. Li, W. Wu, Y. Chen, D. L. Olynick, S. Y. Wang, W. M. Tong, and R. S. Williams. Vapor-phase self-assembled monolayer for improved mold release in nanoimprint lithography. *LANGMUIR*, 21(4):1158–1161, 2005.

[57] H. W. Sun, J. Q. Liu, P. Gu, and D. Chen. Anti-sticking treatment for a nanoimprint stamp. *APPLIED SURFACE SCIENCE*, 254(10):2955–2959, 2008.

[58] L. H. Sperling. *Introduction to Physical Polymer Science*. Wiley-Interscience, 3rd edition, 2001.

[59] F. Q. Nie, M. Macka, L. Barron, D. Connolly, N. Kent, and B. Paull. Robust monolithic silica-based on-chip electro-osmotic micro-pump. *ANALYST*, 132(5):417–424, 2007.

[60] A. Gupta, D. Akin, and R. Bashir. Single virus particle mass detection using microresonators with nanoscale thickness. *APPLIED PHYSICS LETTERS*, 84(11):1976–1978, 2004.

[61] Y. C. Wang and R. Lakes. Analytical parametric analysis of the contact problem of human buttocks and negative poisson's ratio foam cushions. *INTERNATIONAL JOURNAL OF SOLIDS AND STRUCTURES*, 39(18):4825–4838, 2002.

[62] Anthony C. Fischer-Cripps. *Introduction to Contact Mechanics*. Springer, 2000.

[63] R.G. Larson. *The structure and rheology of complex fluids*. Oxford, 1999.

[64] George E. Dieter. *Mechanical Metallurgy*. McGraw-Hill, si metric edition edition, 1988.

[65] J. Rottler and M. O. Robbins. Yield conditions for deformation of amorphous polymer glasses. *PHYSICAL REVIEW E*, 64(5), 2001.

[66] J. Rottler and M. O. Robbins. Shear yielding of amorphous glassy solids: Effect of temperature and strain rate. *PHYSICAL REVIEW E*, 68(1), 2003.

[67] R. Quinson, J. Perez, M. Rink, and A. Pavan. Yield criteria for amorphous glassy polymers. *JOURNAL OF MATERIALS SCIENCE*, 32(5):1371–1379, 1997.

[68] Anthony C. Fischer-Cripps. *Nanoindentation*. Springer, 2002.

[69] P.S. Hong and H. H. Lee. Pattern uniformity control in room-temperature imprint lithography. *APPLIED PHYSICS LETTERS*, 83(12):2441, September 2003.

[70] R. J. Kent. Indentation processes in poly(methylmethacrylate) .2. cone indentation and deep punching. *JOURNAL OF PHYSICS D-APPLIED PHYSICS*, 16(2):135–149, 1983.

[71] C. H. Lin and R. S. Chen. Effects of mold geometries and imprinted polymer resist thickness on ultrasonic nanoimprint lithography. *JOURNAL OF MICROMECHANICS AND MICROENGINEERING*, 17:1220–1231, 2007.

[72] David Cebon Michael Ashby, Hugh Shercliff. *Materials: Engineering, Science, Processing and Design*. Butterworth-Heinemann, 2007.

[73] S. L. Semiatin George Ellwood Dieter, Howard A. Kuhn. *Handbook of Workability and Process Design*. ASM International, 2003.

[74] S. A. A. A. Mousavi, H. Feizi, and R. Madoliat. Investigations on the effects of ultrasonic vibrations in the extrusion process. *JOURNAL OF MATERIALS PROCESSING TECHNOLOGY*, 187:657–661, 2007.

[75] J. C. Hung, Y. C. Tsai, and C. H. Hung. Frictional effect of ultrasonic-vibration on upsetting. *ULTRASONICS*, 46(3):277–284, 2007.

[76] I.M. Ward. *An introduction to the mechanical properties of solid polymers*. Wiley, 1995.

[77] V. Lorenzo, R. Benavente, E. Perez, A. Bello, and J. M. Perena. Microhardness as a thermally activated process - indentation time-dependence for an amorphous copolyester. *JOURNAL OF APPLIED POLYMER SCIENCE*, 48(7):1177–1181, May 1993.

[78] R. D. Priestley, C. J. Ellison, L. J. Broadbelt, and J. M. Torkelson. Structural relaxation of polymer glasses at surfaces, interfaces and in between. *SCIENCE*, 309(5733):456–459, Jul 2005.

[79] W. C. Oliver and G. M. Pharr. Measurement of hardness and elastic modulus by instrumented indentation: Advances in understanding and refinements to methodology. *JOURNAL OF MATERIALS RESEARCH*, 19(1):3–20, Jan 2004.

[80] G. Binnig, C. F. Quate, and C. Gerber. Atomic force microscope. *PHYSICAL REVIEW LETTERS*, 56(9):930–933, Mar 1986.

[81] V. Bykov, A. Gologanov, and V. Shevyakov. Test structure for spm tip shape deconvolution. *APPLIED PHYSICS A-MATERIALS SCIENCE & PROCESSING*, 66(5):499–502, May 1998.

[82] H. Y. Nie and N. S. McIntyre. A simple and effective method of evaluating atomic force microscopy tip performance. *LANGMUIR*, 17(2):432–436, Jan 2001.

[83] C. V. Nguyen, Q. Ye, and M. Meyyappan. Carbon nanotube tips for scanning probe microscopy: fabrication and high aspect ratio nanometrology. *MEASUREMENT SCIENCE & TECHNOLOGY*, 16(11):2138–2146, Nov 2005.

[84] Q. Ye, A. M. Cassell, H. B. Liu, K. J. Chao, J. Han, and M. Meyyappan. Large-scale fabrication of carbon nanotube probe tips for atomic force microscopy critical dimension imaging applications. *NANO LETTERS*, 4(7):1301–1308, Jul 2004.

[85] Micromasch website. http://www.spmtips.com/.

[86] A. F. Prebus. Events at the university of alberta and the university of toronto, leading to the first north american electron microscope. *MICRON*, 29(4):289–292, Aug 1998.

[87] Polytec website. http://www.polytec.com/.

[88] C. S. Veldman. A novel implementation of an iso standard method for primary vibration calibration by laser interferometry. *METROLOGIA*, 40(2):1–8, 2003.

[89] John Burke. *The Book and Paper Group Annual*, volume 3, chapter "Solubility Parameters: Theory and Application". The American Institute for Conservation, 1984.

[90] D. F. S. Petri. Characterization of spin-coated polymer films. *JOURNAL OF THE BRAZILIAN CHEMICAL SOCIETY*, 13(5):695–699, Sep-Oct 2002.

[91] D. W. Schubert and T. Dunkel. Spin coating from a molecular point of view: its concentration regimes, influence of molar mass and distribution. *MATERIALS RESEARCH INNOVATIONS*, 7(5):314–321, Oct 2003.

[92] M. Alcoutlabi and G. B. McKenna. Effects of confinement on material behaviour at the nanometre size scale. *JOURNAL OF PHYSICS-CONDENSED MATTER*, 17(15):R461–R524, Apr 2005.

[93] C. J. Ellison and J. M. Torkelson. The distribution of glass-transition temperatures in nanoscopically confined glass formers. *NATURE MATERIALS*, 2(10):695–700, Oct 2003.

[94] P. Scheidler, W. Kob, and K. Binder. The relaxation dynamics of a confined glassy simple liquid. *EUROPEAN PHYSICAL JOURNAL E*, 12(1):5–9, Sep 2003.

[95] G. B. McKenna. Size and confinement effects in glass forming liquids: Perspectives on bulk and nano-scale behaviours. *JOURNAL DE PHYSIQUE IV*, 10(P7):53–57, May 2000.

[96] M. D. Stewart, J. T. Wetzel, G. M. Schmid, F. Palmieri, E. Thompson, E. K. Kim, D. Wang, K. Sotodeh, K. Jen, S. C. Johnson, J. Hao, M. D. Dickey, Y. Nishimura, R. M. Laine, D. J. Resnick, and C. G. Willson. Direct imprinting of dielectric materials for dual damascene processing. In R. S. Mackay, editor, *Emerging Lithographic Technologies IX. Edited by Mackay, R. Scott. Proceedings of the SPIE, Volume 5751, pp. 210-218 (2005).*, pages 210–218, May 2005.

[97] M. F. Paige. A comparison of atomic force microscope friction and phase imaging for the characterization of an immiscible polystyrene/poly(methyl methacrylate) blend film. *POLYMER*, 44(20):6345–6352, Sep 2003.

[98] S. P. Jarvis, T. Uchihashi, T. Ishida, H. Tokumoto, and Y. Nakayama. Local solvation shell measurement in water using a carbon nanotube probe. *JOURNAL OF PHYSICAL CHEMISTRY B*, 104(26):6091–6094, Jul 2000.

[99] D. S. Sanditov and A. B. Bainova. Viscous flow and plastic deformation of glasses in the model of excited atoms. *GLASS PHYSICS AND CHEMISTRY*, 30(2):113–131, Mar-Apr 2004.

[100] V. Gonda, J. den Toonder, J. Beijer, G. Q. Zhang, and L. J. Ernst. Finite thickness influence on spherical and conical indentation on viscoelastic thin polymer film. *JOURNAL OF ELECTRONIC PACKAGING*, 127(1):33–37, Mar 2005.

[101] S. J. Bull. Nano-indentation of coatings. *JOURNAL OF PHYSICS D-APPLIED PHYSICS*, 38(24):R393–R413, Dec 2005.

[102] J. D. Sherwood and D. Durban. Squeeze-flow of a herschel-bulkley fluid. *JOURNAL OF NON-NEWTONIAN FLUID MECHANICS*, 77(1-2):115–121, 1998.

[103] R. D. Venter W. Johnson, R. Sowerby. *Plane strain slip line fields for metal deformation processes.* Pergamon, 1982.

[104] H. M. Laun, R. Bung, S. Hess, W. Loose, O. Hess, K. Hahn, E. Hadicke, R. Hingmann, F. Schmidt, and P. Lindner. Rheological and small-angle neutron-scattering investigation of shear-induced particle structures of concentrated polymer dispersions submitted to plane poiseuille and couette-flow. *JOURNAL OF RHEOLOGY*, 36(4):743–&, May 1992.

[105] S. D. Yeo and E. Kiran. High-pressure density and viscosity of polystyrene solutions in methylcyclohexane. *JOURNAL OF SUPERCRITICAL FLUIDS*, 15(3):261–272, Jul 1999.

[106] B. D. Gates, Q. B. Xu, M. Stewart, D. Ryan, C. G. Willson, and G. M. Whitesides. New approaches to nanofabrication: Molding, printing, and other techniques. *CHEMICAL REVIEWS*, 105(4):1171–1196, Apr 2005.

[107] C. Perret, C. Gourgon, F. Lazzarino, J. Tallal, S. Landis, and R. Pelzer. Characterization of 8-in wafers printed by nanoimprint lithography. *MICROELECTRONIC ENGINEERING*, 73-74:172–177, Jun 2004.

[108] A. Rosochowski. Die compensation procedure to negate die deflection and component springback. *JOURNAL OF MATERIALS PROCESSING TECHNOLOGY*, 115(2):187–191, Sep 2001.

[109] A. Rosochowski and R. Balendra. Effect of secondary yielding on nett-shape forming. *JOURNAL OF MATERIALS PROCESSING TECHNOLOGY*, 58(2-3):145–152, Mar 1996.

[110] C. J. Nonhof and G. A. Luiten. Estimates for process conditions during the ultrasonic welding of thermoplastics. *POLYMER ENGINEERING AND SCIENCE*, 36(9):1177–1183, May 1996.

[111] H. VanWijk, G. A. Luiten, P. G. VanEngen, and C. J. Nonhof. Process optimization of ultrasonic welding. *POLYMER ENGINEERING AND SCIENCE*, 36(9):1165–1176, May 1996.

[112] D. N. Smyrnaios and J. A. Tsamopoulos. Squeeze flow of bingham plastics. *JOURNAL OF NON-NEWTONIAN FLUID MECHANICS*, 100(1-3):165–190, Sep 2001.

[113] A. Matsoukas and E. Mitsoulis. Geometry effects in squeeze flow of bingham plastics. *JOURNAL OF NON-NEWTONIAN FLUID MECHANICS*, 109(2-3):231–240, Feb 2003.